

# SPIN TRANSPORT IN LOW-DIMENSIONAL MATERIALS: A STUDY FROM FIRST PRINCIPLE ELECTRONIC STRUCTURE CALCULATIONS

Thesis

submitted in partial fulfilment of the requirements for the degree of

DOCTOR OF PHILOSOPHY

IN

PHYSICS

by

**Nayana Devaraj**

(Reg. No. 165110PH16F05)



DEPARTMENT OF PHYSICS

NATIONAL INSTITUTE OF TECHNOLOGY KARNATAKA (NITK)

SURATHKAL, MANGALORE - 575 025

April, 2022

## DECLARATION

by the Ph.D. Research Scholar

I hereby declare that the Research Thesis titled '**Spin transport in low-dimensional materials: A study from first principle electronic structure calculations**', which is being submitted to the **National Institute of Technology Karnataka, Surathkal** in partial fulfilment of the requirements for the award of the **Degree of Doctor of Philosophy** in Physics is a bonafide report of the research work carried out by me under the guidance of **Dr. Kartick Tarafder**. The material contained in this Research Thesis has not been submitted to any university or institution for the award of any degree.



**Nayana Devaraj**

Register No: 165110 PH16F06

Department of Physics


NITK Surathkal

Place: NITK, Surathkal

Date: 21-09-2021

## CERTIFICATE

This is to certify that the Research Thesis titled '**Spin transport in low-dimensional materials: A study from first principle electronic structure calculations**' submitted by **Nayana Devaraj**, (Register Number:165110 PH16F05) as the record of the research work carried out by her, is accepted as the Research Thesis submission in partial fulfilment of the requirements for the award of degree of **Doctor of Philosophy**.

  
21/9/2021

**Dr. Kartick Tarafder**  
Research guide  
Assistant Professor  
Department of Physics  
NITK Surathkal - 575025



**Chairman - DRPC**  
(Signature with Date and Seal)

ASSOCIATE PROFESSOR & HEAD  
Physics Department  
NITK Surathkal, Mangalore-575025  
KARNATAKA

## Acknowledgement

First of all, I would like to thank my supervisor, Dr. Kartick Tarafder. He has been one of the most influential people in life for the last 5 years as a great guide, as an excellent researcher, and more than all as a great human being. I consider myself lucky to have been able to conduct my research under someone like him, who always motivates others, who always rejoices in the growth of others, who always treats others with care and compassion. I am incredibly thankful for the amount of time and energy he spent helping me solve the research problems, improve my writing and presentations, and even confidence.

During the research period, I spent most of my time with colleagues in the research lab. They were always there in dispelling doubts, giving suggestions, and motivating. The contributions made by each of them to my research are invaluable. I would like to thank Ms. Sruthi T., Ms. Vijaya A.R., Ms. Sulakshana Shenoy, Mr. Ramesh Reddy, Mr. Anantharam K.S., Ms. Subhasmita Ray, and Ms. Suneetha N. for always been supportive and helpful colleagues.

The interactions with project students in the research lab have helped a lot to improve my understanding. I owe my gratitude to each one of them.

I owe my gratitude to my Research Progress Assessment Committee members Dr. Shashikala H.D. and Dr. Jagannathan T.K. Their valuable feedback, suggestions, and encouragement helped me a lot to improve my research.

The computational facility provided by the high-performing computing (HPC) machine of NITK was crucial in completing my research. I owe my immense gratitude to the institute for providing computational facilities.

The workshops, conferences, and seminars I have attended during these periods have helped me to improve my basic understanding and interest. I am grateful to all who provided opportunities to attend all those and to all with whom I have interacted during those times.

I am grateful to all the faculty members of the Physics Department of NITK Surathkal, Prof. Kasturi. V. Bangera, Prof. N. K. Udayashankar, Dr. M. N. Satyanarayan, Dr. H. S. Nagaraja, Dr. Ajith K.M., Dr. Partha P. Das, Dr. Shajahan T.K., Dr. Deepak Vaid, Dr. Kishore Sridharan, and Dr. Sreenath V. for the constant support, motivation, and help they provided during my research life. I am also thankful to the non-teaching staff of the Department, Mrs. Veena, Mrs. Ashalatha, Mr. Pradeep, Mr. Harshith, Mr. Dhanaraj, Mr. Karthik, Mr. Santhosh, and Mrs. Suma, for their kind support for my day-to-day activities in the department.

Many research scholars from the other research labs were also always there to give guidance, clarify doubts. I want to acknowledge the sincere help and kindness from each and everyone over these years.

I would also like to express my gratitude to U.G. and P.G. students, research scholars from other departments, staff at the hostel, and the office at NITK. I have always received their love, help, and cooperation. I would like to extend my gratitude to them.

Finally, I would like to thank my family and friends for their constant support and encouragement during my Ph.D. I will always be grateful for the encouragement, love, support, care, and patience they have shown me.

Thank you,  
Nayana Devaraj

## Abstract

Conventional storage and processing devices based on the electrons' charge transport mechanisms are insufficient to meet the needs of the future. Spintronics, in which the electron's spin degree of freedom has also been exploited along with its charge, can be considered an alternative to charge-based technology. Storage and processing devices based on spin transport can overcome the limitations of charge-based transport devices and can provide many additional device functionalities. Two-dimensional (2D) materials are considered a suitable medium for spin transport. This thesis mainly focused on spin transport in 2D materials. Herein, the electronic structure and magnetic properties of various 2D materials have been thoroughly investigated using first-principle calculations. Magnetic metal-2D material interfaces are constructed and the possibility of spin injection/scattering has been carefully studied at the interface. Two probe magnetic junctions are modeled by combining different 2D materials and metals, where 2D materials are sandwiched between two magnetic electrodes. Spin-transport properties are investigated through magnetic junctions by performing a combined study of density functional theory (DFT) and nonequilibrium Green's function (NEGF) methods. The transmission spectrum, current-voltage characteristics, spin injection efficiency, and magnetoresistance are calculated for different modeled devices at various bias voltages in the parallel and anti-parallel electrodes magnetic configurations. Overall, this work provides a better understanding of spin injection at the metal-2D material interface. The reported results in this thesis could be suitable guidelines for the development of future spintronic devices based on TMDC materials.

Keywords: electronic structure, density functional theory, non-equilibrium Green's function method, spin-transport, magnetoresistance, two-dimensional materials, transition metal dichalcogenides, chromium trihalides

# Contents

<b>List of Figures</b>	<b>viii</b>
<b>List of Tables</b>	<b>xi</b>
<b>Nomenclature</b>	<b>xii</b>
<b>1 Introduction</b>	<b>1</b>
1.1 Spintronics . . . . .	2
1.2 Spin and Ferromagnetism . . . . .	3
1.3 Spin Valve . . . . .	4
1.4 Materials for Spin Transport . . . . .	5
1.5 Scope and Objectives of the Proposed Work . . . . .	9
1.6 Organization of the Thesis . . . . .	10
<b>2 Methodology</b>	<b>11</b>
2.1 Electronic Structure Theory . . . . .	11
2.1.1 Many-body Schrödinger Equation . . . . .	11
2.1.2 Born-Oppenheimer Approximation . . . . .	13
2.1.3 Hartree-Fock approximation . . . . .	13
2.1.4 Density Functional Theory (DFT) . . . . .	14
2.1.5 Kohn-Sham DFT . . . . .	15
2.2 Quantum Transport . . . . .	19
2.2.1 Ballistic transport . . . . .	20
2.2.2 Landauer’s formula . . . . .	23
2.2.3 Scattering Matrix . . . . .	24
2.2.4 Non-Equilibrium Green’s Function (NEGF) Theory . . . . .	26
2.2.5 NEGF-DFT Formalism . . . . .	33
2.3 Transport Calculation Using TranSIESTA . . . . .	37
2.4 Spin Transport . . . . .	38
<b>3 Electronic Structure of Low Dimensional Materials</b>	<b>41</b>
3.1 Introduction . . . . .	41
3.2 Methodology . . . . .	41

3.3	Results and Discussions . . . . .	42
3.3.1	Graphene . . . . .	42
3.3.2	Transition Metal Dichalcogenides . . . . .	43
3.3.3	Co/monolayer TMDC Interfaces . . . . .	46
3.4	Conclusion . . . . .	53
<b>4</b>	<b>Spin Transport Through Magnetic Junctions Composed of Transition Metal Dichalcogenides</b>	<b>54</b>
4.1	Introduction . . . . .	54
4.2	Methodology . . . . .	55
4.3	Results and Discussions . . . . .	56
4.3.1	MoS <sub>2</sub> Based Magnetic Junctions . . . . .	56
4.3.2	MoSe <sub>2</sub> Based Magnetic Junctions . . . . .	68
4.3.3	WS <sub>2</sub> Based Magnetic Junctions . . . . .	72
4.4	Conclusion . . . . .	74
<b>5</b>	<b>Electronic Structure of Two-Dimensional Ferromagnetic Materials</b>	<b>75</b>
5.1	Introduction . . . . .	75
5.2	Methodology . . . . .	76
5.3	Results and Discussions . . . . .	77
5.3.1	Monolayer CrX <sub>3</sub> Materials . . . . .	77
5.3.2	CrX <sub>3</sub> /TMDC Heterostructure . . . . .	79
5.4	Conclusion . . . . .	84
<b>6</b>	<b>Spin Transport in Magnetic Junctions with 2D Ferromagnetic Materials</b>	<b>86</b>
6.1	Introduction . . . . .	86
6.2	Methodology . . . . .	87
6.3	Results and Discussions . . . . .	88
6.3.1	Spin Transport through Co/trilayer CrI <sub>3</sub> /Co Magnetic Junctions . . . . .	88
6.3.2	Spin Transport through Co/CrI <sub>3</sub> /TMDC/CrI <sub>3</sub> /Co Magnetic Junctions . . . . .	91
6.4	Conclusion . . . . .	95
<b>7</b>	<b>Summary and Future Work</b>	<b>96</b>
7.1	Summary . . . . .	96
7.2	Scope of Future Work . . . . .	98
	<b>References</b>	<b>100</b>



# List of Figures

1.1	Typical spin valve structure . . . . .	5
2.1	Flow chart of the Kohn-Sham iteration scheme . . . . .	18
2.2	Schematic representation of motion of electrons through the channel	20
2.3	Schematic representation of a mesoscopic channel connected to source and drain . . . . .	20
2.4	E-k diagram for source, channel and drain . . . . .	21
2.5	Quantized conductance . . . . .	22
2.6	Conductor connected to source and drain . . . . .	23
2.7	Schematic representation of scattering at a coherent conductor . . .	25
2.8	Schematic representation of a conductor connected to reservoirs through a set of semi-infinite ballistic leads . . . . .	26
2.9	Retarded Green's function for an infinite 1-D wire . . . . .	28
2.10	Flowchart illustrating the self-consistent cycle in a standard DFT calculation, and a NEGF-DFT calculation. . . . .	34
2.11	Schematic diagram of a two-probe device model. . . . .	35
3.1	Structure of graphene. . . . .	42
3.2	Electronic structure of graphene. . . . .	42
3.3	Unit cells of monolayer, bilayer, trilayer, and bulk MoS <sub>2</sub> . . . . .	44
3.4	The crystal structure of monolayer MoS <sub>2</sub> . . . . .	44
3.5	Electronic structure of MoS <sub>2</sub> . . . . .	45
3.6	Partial density of states of monolayer MoS <sub>2</sub> . . . . .	45
3.7	DOS of monolayer TMDC materials. . . . .	46
3.8	Geometrical structure of Co/MoS <sub>2</sub> . . . . .	47
3.9	DOS of Co/MoS <sub>2</sub> interface . . . . .	47
3.10	DOS of monolayer MoS <sub>2</sub> in the isolated structure and Co/MoS <sub>2</sub> heterostructure . . . . .	48
3.11	Spin polarization in the MoS <sub>2</sub> layer . . . . .	49
3.12	Band structure of Co/MoSe <sub>2</sub> . . . . .	49
3.13	Magnetization density plot for Co/MoS <sub>2</sub> . . . . .	50
3.14	Spin charge transfer of Co/MoS <sub>2</sub> . . . . .	51

3.15	Geometrical structure of Co/MoSe <sub>2</sub> . . . . .	52
3.16	DOS of monolayer MoSe <sub>2</sub> in the isolated structure and Co/MoSe <sub>2</sub> heterostructure . . . . .	52
4.1	Device model of Co/monolayer MoS <sub>2</sub> /Co . . . . .	57
4.2	Transmission spectrum of Co/monolayer MoS <sub>2</sub> /Co at the equilib- rium condition. . . . .	57
4.3	Transport properties of Co/monolayer MoS <sub>2</sub> /Co . . . . .	59
4.4	Device model of Co/trilayer MoS <sub>2</sub> /Co . . . . .	60
4.5	Transmission spectrum of Co/trilayer MoS <sub>2</sub> /Co at the equilibrium condition. . . . .	60
4.6	DOS of MoS <sub>2</sub> layers . . . . .	61
4.7	Transport properties of Co/trilayer MoS <sub>2</sub> /Co . . . . .	61
4.8	Device model of Co/MoS <sub>2</sub> /MoSe <sub>2</sub> /MoS <sub>2</sub> /Co . . . . .	62
4.9	Transport properties of Co/MoS <sub>2</sub> /MoSe <sub>2</sub> /MoS <sub>2</sub> /Co . . . . .	63
4.10	Device model of Co/MoS <sub>2</sub> /graphene/MoS <sub>2</sub> /Co . . . . .	65
4.11	Transmission spectrum of Co/MoS <sub>2</sub> /graphene/MoS <sub>2</sub> /Co. . . . .	65
4.12	V-I characteristics of Co/MoS <sub>2</sub> /graphene/MoS <sub>2</sub> /Co. . . . .	66
4.13	MR and SIE of Co/MoS <sub>2</sub> /graphene/MoS <sub>2</sub> /Co. . . . .	67
4.14	K-resolved and spin-resolved transmission spectrum of Co /MoS <sub>2</sub> /graphene /MoS <sub>2</sub> /Co . . . . .	67
4.15	Device models of Co-MoSe <sub>2</sub> magnetic junctions . . . . .	69
4.16	Transport properties of Co/monolayer MoSe <sub>2</sub> /Co . . . . .	70
4.17	Transport properties of Co/trilayer MoSe <sub>2</sub> /Co . . . . .	70
4.18	Transport properties of Co/MoSe <sub>2</sub> /MoS <sub>2</sub> /MoSe <sub>2</sub> /Co . . . . .	71
4.19	Device models of Co-WS <sub>2</sub> magnetic junctions . . . . .	72
4.20	Transport properties of Co/monolayer WS <sub>2</sub> /Co . . . . .	73
4.21	Transport properties of Co/trilayer WS <sub>2</sub> /Co . . . . .	73
5.1	Geometric structure of CrX <sub>3</sub> monolayer . . . . .	76
5.2	DOS of CrX <sub>3</sub> monolayers . . . . .	77
5.3	Spin polarised band structures of CrX <sub>3</sub> monolayers . . . . .	78
5.4	Geometric structure of CrX <sub>3</sub> /TMDC heterostructure . . . . .	80
5.5	DOS of CrBr <sub>3</sub> monolayer in CrBr <sub>3</sub> /TMDC heterostructures. . . . .	82
5.6	Spin polarised band structure of CrBr <sub>3</sub> /TMDC heterostructures. . . . .	83
5.7	Effective potential profile of the MoS <sub>2</sub> /CrBr <sub>3</sub> interface. . . . .	84
6.1	Schematic representation of Co/trilayer CrI <sub>3</sub> /Co magnetic junction . . . . .	88
6.2	Transmission spectrum of Co/trilayer CrI <sub>3</sub> /Co at the equilibrium condition. . . . .	89
6.3	Transport properties of Co/trilayer CrI <sub>3</sub> /Co magnetic junction. . . . .	90

6.4	Schematic representation of Co/CrI <sub>3</sub> /TMDC/CrI <sub>3</sub> /Co magnetic junction . . . . .	91
6.5	Transport properties of Co/CrI <sub>3</sub> /MoS <sub>2</sub> /CrI <sub>3</sub> /Co magnetic junction.	92
6.6	Transport properties of Co/CrI <sub>3</sub> /MoSe <sub>2</sub> /CrI <sub>3</sub> /Co magnetic junction.	92
6.7	Transport properties of Co/CrI <sub>3</sub> /WS <sub>2</sub> /CrI <sub>3</sub> /Co magnetic junction. .	93
6.8	Transport properties of Co/CrI <sub>3</sub> /WSe <sub>2</sub> /CrI <sub>3</sub> /Co magnetic junction.	93

# List of Tables

5.1	Bandgap of CrX <sub>3</sub> monolayers . . . . .	77
5.2	The calculated parameters in CrX <sub>3</sub> /TMDC . . . . .	81

# Nomenclature

## Abbreviations

<i>GGA</i>	Generalised Gradient Approximation
<i>LDA</i>	Local Density Approximation
$P_S$	Spin Polarization
<i>vdW</i>	van der Waals
CBO	Conduction Band Offset
DFT	Density Functional Theory
DOS	Density of States
GMR	Giant Magnetoresistance
MR	Magnetoresistance
MTJ	Magnetic Tunnel Junction
NEGF	Non Equilibrium Green's Function
PDOS	Projected Density of States
SBH	Schottky Barrier Height
SIE	Spin Injection Efficiency
SIESTA	Spanish Initiative for Electronic Simulations with Thousands of Atoms
SOC	Spin Orbit Coupling
TMDC	Transition Metal Dichalcogenides
TMR	Tunnel Magnetoresistance
VASP	Vienaa Ab-initio Simulation Package
VBO	Valence Band Offset

## Chemical formulae

Br	Bromine
Cl	Chlorine
Co	Cobalt
CrBr <sub>3</sub>	Chromium tri-bromide
CrCl <sub>3</sub>	Chromium tri-chloride
CrI <sub>3</sub>	Chromium tri-iodide
Cr	Chromium
hBN	Hexagonal Boron Nitride
I	Iodine
MoS <sub>2</sub>	Molybdenum disulfide
MoSe <sub>2</sub>	Molybdenum disulfide
Mo	Molybdenum
S	Sulfur
WS <sub>2</sub>	Tungsten disulfide
WSe <sub>2</sub>	Tungsten diselenide
W	Tungsten

## Fundamental constants

$\hbar$	Reduced Planck's constant	$1.054571 \times 10^{-34} \text{ J s}$
$\mu_B$	Bohr magneton	$9.274009 \times 10^{-24} \text{ J T}^{-1}$
$c$	Speed of light in a vacuum	$2.997\,924\,58 \times 10^8 \text{ m s}^{-1}$
$e$	Electron charge	$1.602176 \times 10^{-19} \text{ C}$
$h$	Planck's constant	$6.626070 \times 10^{-34} \text{ J s}$
$k_B$	Boltzmann constant	$1.380648 \times 10^{-23} \text{ m}^2\text{kg/s}^2\text{K}$

# Chapter 1

## Introduction

One important trait of human beings is the systematic documentation and processing of information about their history, philosophy, art, etc. This is an interesting trend that human beings carried forward from their primitive selves in the prehistoric era. Starting from cave paintings to stone tablets to parchments to papyrus, humans have chosen many mediums for storing information. In the 15<sup>th</sup> century, after the invention of printing technology, this became the standard way of storing historical information due to its ease of use. It also became the go-to medium for sharing information as well - giving rise to printed textbooks, newspapers, magazines, and much more. With the discovery of computational devices, we quickly learned that we could do much more with machines than simply storing information. We started using it for difficult calculations and other computations.

The discovery of electronic transistors in 1947 and an incredible boom in electronics further followed has unimaginably changed society. This digital revolution, which brought fast and efficient electronic devices, is marked as the third industrial revolution. This technological boom has evolved into improving the overall standard of living for the human population. In 1965, Gordon E. Moore, the then co-founder of Fairchild semiconductors and soon to be the co-founder of Intel Corporation, observed that the number of components (transistors, resistors, diodes, or capacitors) in a dense integrated circuit had doubled approximately every year. He speculated that it would continue to do so for at least the next ten years. This prediction held good. In 1975, he revisited the hypothesis and stated that the number of components in an integrated circuit would double every year. Moore's this prediction, which was later known as Moore's law, held good for another four decades. But there is an endless need for devices that can be used to store, access, and process information efficiently and inexpensively. This need drove significant changes in the storage and computing industry in the 20<sup>th</sup>

century. In the current scenario, the number of transistors in an integrated circuit has already gone beyond the order of  $10^9$ . On the other hand, device size has also been reduced to the nanometer range. As the transistor size reduces to the nanoscale, which includes only a few atoms, the power dissipation increases, and quantum fluctuations emerge. Many cases where the simple laws of physics were previously applicable became invalid, posting the need for a new paradigm.

Spintronics is the field that can overcome the limitations of electronics and deliver the devices needed for the 21<sup>st</sup> century. The electronics technology is based on the utilization of an electron's charge, whereas spin-based electronics, or spintronics, exploits the spin degrees of freedom of the electrons along with its charge. One of the advantages of utilizing spin is the improvement of the device functionalities in smaller devices. Spin-based devices also consume significantly less power than charge-based devices. In addition to that, compared to conventional charge-based devices, spin-based devices can perform operations extremely fast. Also, the storage of the spin state is more reliable. Therefore, spintronics applications would be the best possible way to obtain smaller, faster, efficient, and reliable devices (Wolf et al., 2006). Such devices can bring a revolution in the standard of human life and society. It has become essential today to have better spintronics devices. To realize that, intense research is underway on spin transport devices.

## 1.1 Spintronics

Spintronics or spin-electronics is the branch of condensed matter physics that studies the properties of electron spin to improve the efficiency of electronic devices and to enrich them with new functionalities (Pulizzi, 2012). Spintronics has paved the way for designing new advanced devices, also provides a deeper understanding of fundamental physics. Knowledge of how the quantum mechanical entity, the spin - interacts with electrons other degrees of freedom and how it behaves in the atomic environment, provides a deeper understanding of matter and its quantum nature.

Spintronics has grown significantly in a short period of time. The advances in this field are based on the extent to which the spin of moving electrons can be controlled and detected. All spintronic devices work based on a simple scheme having 3 stages (Chopra, 2019):

- information is stored into spins as a specific spin orientation (up or down)
- the spins, being attached to mobile electrons, carry the information along a



channel

- the information is read at the output terminal

So, the advancement in spintronics is based on the extent of effective spin injection, manipulation, and detection. Intense research is going on to understand more on spin transport phenomena in spintronic devices, to find out an effective method to inject spin into non-magnetic materials, and finding more suitable materials for spin transport (Iqbal et al., 2018; Mishra et al., 2021).

## 1.2 Spin and Ferromagnetism

Since spintronics exploits the intrinsic spin of an electron, it is important to understand more about what the electron spin is and how it becomes significant. Spin is one of the intrinsic properties of an electron which is related to the inherent angular momentum (spin angular momentum). This quantum property can have an up or down configuration depending on the direction of spin angular momentum and can be represented by spin quantum numbers  $+1/2$  or  $-1/2$ . Due to the magnetic moment associated with the spin of an electron, it acts as a tiny magnet. This magnetic moment is much larger than that associated with the nucleus. Therefore, the magnetic behaviour of an atom is determined by the electron. According to Pauli's exclusion principle, electrons in an orbital must have different spin values. As a result, an orbital can hold at most two electrons, and when it is full, the net spin of the orbital is zero. Therefore, only unpaired electrons contribute to the magnetic properties of the atom. But for a high magnetic moment, it is not enough to have atoms with a partially filled electron shell, there must be a strong interaction between the atomic magnets. Such materials are called ferromagnets. It can be visualized that electrons in a ferromagnetic material are mostly moving through either spin-up channel or spin-down channel, which produces a spin-polarized current. So, these materials, which are capable of injecting spin-polarized current into non-magnetic materials, are very important in spintronics.

In spintronic devices, it is also important to generate spin-polarized current in non-magnetic materials. The most common method used to disturb the equality in the number of spin-up and spin-down electrons in non-magnetic materials is the injection of spin-polarized current from a ferromagnetic material. Magnetic fields, electric fields, electromagnetic wave introduction, Zeeman splitting, spin motive forces, thermal gradients, and mechanical rotations are also used to generate spin-

polarized current in non-magnetic materials (Hirohata et al., 2020).

### 1.3 Spin Valve

The elementary spintronic device which controls electron spin current is the spin valve (Julliere, 1975; Slonczewski, 1989). It consists of a thin insulator layer sandwiched between two ferromagnetic layers (Fig. 1.1). The exchange coupling between magnetic layers is suppressed by the interlayer. The flow of electrical current from ferromagnetic material to the non-magnetic interlayer inject spin-polarized electrons. The spin injection efficiency is determined by the spin polarization of ferromagnetic material and scattering of spin-polarized electrons at the interface between a ferromagnetic material and non-magnetic interlayer (Hirohata et al., 2020). The spin injection efficiency is crucial in determining the merit of a spintronic device.

In the spin-valve device, one of the two ferromagnetic layers is pinned or fixed by an anti-ferromagnet which raises its magnetic coercivity. This magnetically hard layer is insensitive to the external magnetic field. But, the other magnetic layer is sensitive to even a tiny external magnetic field. This magnetically soft material that changes its magnetization direction due to the applied field is known as the free layer or unpinned layer. Since the magnetic moment of the free layer changes easily with the external magnetic field, it is possible to obtain a spin valve with different relative magnetic orientations. If magnetic orientations are in the same direction, it is called parallel configuration and if both ferromagnetic layers are in opposite magnetic orientation, then that is anti-parallel configuration. The relative magnetic orientation of the ferromagnetic layer influences scattering of spin-up electrons and spin-down electrons differently. Thus a spin-polarized current occurs.

The effect in the electrical resistance of a material or device sensitive to magnetic orientation is called magnetoresistance. The electrical resistance is relatively high for anti-parallel configuration and relatively low for parallel configuration. Magnetoresistance is considered an important measure of device merit. It is defined as the resistance difference between anti-parallel ( $R_{APC}$ ) and parallel ( $R_{PC}$ ) configurations of electrodes normalized by the resistance in the parallel configuration (Tsymbal et al., 2003),

$$MR = \frac{R_{APC} - R_{PC}}{R_{PC}} \quad (1.1)$$

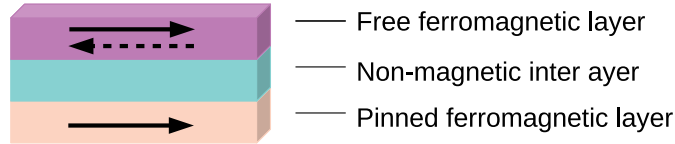


Fig. 1.1: Typical spin valve structure.

Higher MR values provide a more sensitive spintronic device, which is desirable. The widespread use of spin valves as the transducer in computer hard disk drive heads is due to its sensitivity to very weak magnetic fields (Chopra, 2019).

The interlayer barrier plays a crucial role in determining the properties of a spin valve. Oxide layers like  $\text{Al}_2\text{O}_3$ ,  $\text{MgO}$ ,  $\text{HfO}_2$ , and  $\text{Y}_2\text{O}_3$  were commonly used as the interlayer barrier in the beginning (Miyazaki et al., 1991; Moodera et al., 1995; Bowen et al., 2001; Chakraverty et al., 2013). But the defects and trapped charges in the metal oxide barrier demand for new materials (Cobas et al., 2012; Dankert et al., 2015). Therefore, it is imperative to find new interlayer barriers to overcome these problems.

## 1.4 Materials for Spin Transport

### 2D Materials

Two-dimensional materials could be an ideal choice to use as the interlayer barrier in advanced spin-valve devices. These materials are very suitable for spin transport, which is transverse in nature. Also, 2D semiconductors having a few atoms' thicknesses, would be the most suitable for an electron transport channel. This is not just due to their minimal thickness but their uniformity over a large area. The uniform bandgap over a large area, pristine interfaces without out-of-plane dangling bonds, the potential to allow efficient electrostatics, reduction of short channel effects, fewer traps on a semi conductor-dielectric interface, and a high degree of vertical scaling are the other factors that make 2D materials suitable for low dimensional transistors (Kang et al., 2014). 2D materials are also helpful in achieving atomically sharp interfaces (Dieny et al., 2020).

### Graphene

Graphene is the first man-made 2D material. As the name indicates, graphene is related to graphite which is an allotrope of carbon. The unexpected behaviour

in extremely thin layers of graphite caught the attention of scientists back in the mid-20<sup>th</sup> century. Therefore, attempts had been going on to make thinner layers of graphite since then. It continued till 2004 when Andrei Geim and Kostya Novoselov performed a simple experiment using a lump of graphite and a normal sticky scotch tape (Novoselov et al., 2005a). The graphite fragments were separated again and again with scotch tape, and they were able to separate them into flakes with the thickness of only an atom. This one-atom-thick layer packed in a dense honeycomb crystal structure is called graphene. Andrei Geim and Kostya Novoselov were awarded the 2010 Physics Nobel Prize for the discovery of this important material.

What makes graphene an important material is not only the fact that it is the 2D material that was first separated, but graphene stands out due to its fascinating mechanical, thermal, electrical, and optical properties as well (Zhen and Zhu, 2018). This one C atom-thick (around 0.34 nm) material is recognized as the toughest 2D material. Graphene is much harder than both steel and diamond of the same dimensions. It is a very light material, which weighs just 0.77 mg/m<sup>2</sup> (Kamaruddin, 2016). It also has an extremely high surface area (theoretical specific surface is 2630 m<sup>2</sup>/g) (Stoller et al., 2008). Other remarkable properties are its high tensile strength and flexibility (Lee et al., 2008; Gómez-Navarro et al., 2008). Graphene's electrical current density is about one million times that of copper. It has very low resistivity and high intrinsic mobility (Rao et al., 2010). These characteristics make graphene the fastest and most efficient conductor. But, since graphene is a zero bandgap material, it cannot be readily used as a transistor material. However, attempts are being made to use graphene in transistors by opening the bandgap in a variety of ways and making appropriate changes.

Graphene also has a promising role in the spintronic industry. The 2D nature of graphene provides a confined spin diffusion in lateral dimensions. Additionally, the long spin-flip length due to its very weak spin-orbit interaction makes graphene very suitable for spintronic application (Huertas-Hernando et al., 2007). However, the weak spin-orbit interaction of graphene makes it difficult to manipulate spin in graphene electrically. The proximity of ferromagnetic material helps to overcome this (Zhang et al., 2011). The metallic character of graphene averts the formation of the Schottky barrier at the interface when it comes in contact with ferromagnetic materials. Thus the additional contact resistance can be avoided at the interface. So, the combination of graphene and ferromagnetic materials can effectively be used in spintronic devices.

It did not take long for the discovery that spin transport through the graphene layer would occur in the presence of ferromagnetic electrodes. Within a few years

of the discovery of graphene, in 2007, Tombros *et al.* demonstrated the spin transport through graphene using Co/Al<sub>2</sub>O<sub>3</sub> tunnel electrode (Tombros *et al.*, 2007). They also obtained spin relaxation length as 1.5 to 2  $\mu\text{m}$  and corresponding spin relaxation time as 100 ps. These values are much greater than other materials. The long spin transport possibility makes graphene an attractive material for spin transport. Further extensive experiments and studies were done in this direction to confirm the possibility of injecting spin current into graphene (Zhang *et al.*, 2011; Semenov *et al.*, 2008; Pi *et al.*, 2010). Subsequent attempts were made mainly to explore how graphene could be utilized for spintronic device applications. For this purpose, studies focusing on the magnetoresistance of graphene were conducted. It is found that even if intrinsic graphene does not exhibit magnetoresistance, using different methods and modifications, graphene films exhibit magnetoresistance (Kim and Kim, 2008; Friedman *et al.*, 2010; Bai *et al.*, 2010; Liao *et al.*, 2012).

### **Transition Metal Dichalcogenides (TMDC)**

After the celebrated discovery of the first 2D material - graphene - great attention has been paid to atomically thin 2D materials. One such 2D material group which received great attention is transition metal dichalcogenides. These materials are available in nature in the bulk form and can be shaped into monolayers easily since bulk crystals are formed of monolayers bound to each other by weak Van der Waals attraction (Novoselov *et al.*, 2005b). Transition metal dichalcogenides have the chemical formula MX<sub>2</sub>, where M is a transition metal atom (such as Mo or W) and X is a chalcogen atom (such as S, Se, or Te). These materials exhibit semiconducting properties and the bandgap of these materials varies with the number of layers. If multilayer materials have an indirect bandgap, their bandgap becomes direct when converted to a monolayer structure (Mak *et al.*, 2010). TMDCs exhibit a unique combination of atomic-scale thickness, direct bandgap, strong spin-orbit coupling (SOC), and favorable electronic and mechanical properties, which make them interesting for fundamental studies and applications in high-end electronics, spintronics, optoelectronics, energy harvesting, flexible electronics, DNA sequencing and personalized medicine (Manzeli *et al.*, 2017). MoS<sub>2</sub> is the most studied material in this family.

Even though graphene has many fascinating properties, its lack of bandgap is a major disadvantage. MoS<sub>2</sub>, a material that shares many similar properties of graphene and has a specific bandgap, provides a promising alternative to graphene. Bulk MoS<sub>2</sub> is an indirect gap semiconductor, with a gap of  $\sim 1.3$  eV (Mak *et al.*, 2010). As the material transitions to a monolayer, the gap becomes direct with a size of  $\sim 1.8$  eV (Lee *et al.*, 2012). The direct bandgap is in the visible frequency

range, most favorable for optoelectronic applications. Another important distinction from graphene is, MoS<sub>2</sub> has an explicitly broken inversion symmetry. It can give rise to the valley Hall effect, where carriers in different valleys flow to opposite transverse edges when an in-plane electric field is applied (Xiao et al., 2007). Inversion symmetry breaking can also lead to valley-dependent optical selection rules for inter-band transitions at K points (Yao et al., 2008). The presence of a direct bandgap in monolayer MoS<sub>2</sub> allows room-temperature field-effect transistors with an on/off ratio exceeding 10<sup>8</sup>. The room-temperature mobility of MoS<sub>2</sub> is over 200 cm<sup>2</sup>/Vs, which is another advantage that makes the material suitable for transistor applications (Radisavljevic et al., 2011).

MoS<sub>2</sub> has a strong spin-orbit coupling (SOC) originated from the d-orbitals of the heavy metal atoms. It provides the possibility to manipulate the spin by an electric field. It can be an interesting platform to explore spin physics and spintronics applications, where graphene can not find any application due to its tiny SOC (Min et al., 2006). MoS<sub>2</sub> has broken inversion symmetry which gives rise to spin splitting at the surface and spin momentum locking. Therefore it has potentially large spin-orbit torques once coupled to a ferromagnet (Zhang et al., 2015). These features point towards the possibility of spintronic properties in MoS<sub>2</sub>. Intense research is going on to utilize MoS<sub>2</sub> and other TMDC materials effectively in spintronic applications including spin transistors (Dolui et al., 2014; Dankert et al., 2015; Wang et al., 2015; Tarawneh et al., 2016).

## 2D Ferromagnetic Materials

The search of different 2D functional materials was continued and many other 2D materials were found such as hexagonal boron nitride (hBN) (Zhang et al., 2017), borophene (Mannix et al., 2015), silicene (Vogt et al., 2012), and germanane (Acun et al., 2015). Although different in many properties, these were generally nonmagnetic materials. Two-dimensional materials with ferromagnetic properties could be an ideal choice for the spin-transport layer in the spin-valve devices and there is high interest in the research community to realize such materials. However, for a long time, 2D ferromagnetism was limited to theoretical explorations (Li et al., 2014; Sun et al., 2017; Kumar et al., 2017; Miao et al., 2017; Kuklin et al., 2017, 2018). The ferromagnetism in 2D materials was observed experimentally for the first time in 2017. Gong *et al.* and Huang *et al.* have reported the intrinsic ferromagnetic behaviour in bilayer Cr<sub>2</sub>Ge<sub>2</sub>Te<sub>6</sub> (Gong et al., 2017) and monolayer CrI<sub>3</sub> (Huang et al., 2017), respectively, using polar magneto-optical Kerr effect microscopy. Similar to CrI<sub>3</sub>, CrCl<sub>3</sub> and CrBr<sub>3</sub> also exhibit ferromagnetism. Researches show that monolayer chromium trihalides can exist as free-standing 2D

crystals (Zhang et al., 2015) and they are dynamically stable. So, it is possible to develop these materials even at room temperature, which is an important factor required for the device application. The most interesting characteristic of these materials is the presence of a completely spin-polarized conduction band edge and valence band edge around Fermi level (Liu et al., 2016; Li et al., 2020). This characteristic makes them suitable for spintronic applications. Since the extraction of 2D  $\text{CrI}_3$  and  $\text{Cr}_2\text{Ge}_2\text{Te}_6$ , a lot of research is going on in the direction to realise more low dimensional magnets experimentally (Sethulakshmi et al., 2019; O'Hara et al., 2018). Along with finding novel 2D ferromagnetic materials with more desirable properties, ongoing intense research is expected to find practical applications for experimentally realized 2D ferromagnetic materials (Huang et al., 2018; Jiang et al., 2018a,b; Wang et al., 2018; Frey et al., 2019). Recent studies on this class of materials so far promise that it could be an integral part of future spintronics devices. However, the field 2D-ferromagnetism is currently in its infancy stage. Extensive research needs to be carried out before using these fascinating materials in advanced spintronic devices.

## 1.5 Scope and Objectives of the Proposed Work

Since conventional charge transport devices are not sufficient to meet future demand, it is imperative to have spin-based transport devices. But such devices that are efficient and suitable for practical applications are yet to be discovered. It is important to know exactly how to inject, manipulate and detect spin in a solid-state system to realize suitable and efficient spin transport devices. Based on the analysis of studies conducted in this field, it can be said that these remain major challenges. There are two main reasons for this. One is the lack of suitable materials which can be used in nano-spintronic devices. The other is the inability to develop suitable magnetic junctions. Only research that focuses on these two fundamental areas can lead the field and realize viable and efficient spin transport devices. Calculation of spin transport through nano-system is extremely challenging, and computationally viable methods for spin transport calculation are still lacking. In this thesis, my broad objectives are the following.

- Study the electronic and magnetic properties of already synthesized low dimensional systems which have the potential for spintronic applications.
- Study the spin injection possibility at various metal-low dimensional material interfaces.

- Develop a general, accurate, and computationally viable method for charge and spin transport calculation in realistic materials.
- Study the spin transport through multilayers and nano contacts.

## 1.6 Organization of the Thesis

The rest of the thesis is organized as follows:

**Chapter 2** discusses the basic concepts and computational methodology of electronic structure calculations and electron transport calculations.

**Chapter 3** presents a detailed investigation of the electronic and magnetic properties of 2D materials. It is extended to the ferromagnetic contact behaviour of Co and TMDC materials.

**Chapter 4** concentrates on spin transport studies. Various magnetic junctions composed of ferromagnetic material Co and TMDC materials are used here for spin transport calculations.

**Chapter 5** presents the study carried out in 2D ferromagnetic materials. The interfacial properties between 2D ferromagnetic materials, chromium trihalides, and 2D TMDC materials are discussed in detail in this chapter. The investigations on the potential of these heterojunctions for the spintronic application are also discussed here.

**Chapter 6** describes spin transport through magnetic junctions composed of 2D ferromagnetic material,  $\text{CrI}_3$ .

**Chapter 7** summarizes the findings of the present research work by highlighting the important results and conclusions drawn from this research work. The scope of further research in this area is also presented here.



# Chapter 2

## Methodology

A proper understanding of material properties is highly essential to understand the potential of using those materials for spin transport studies. The electronic structure is the basis of the fundamental properties of materials. This chapter discusses the basic concepts of electronic structure theory and the first principle methods for electronic structure calculation. The theoretical background of electron transport and the computational methodology for electron transport are also discussed in this chapter.

### 2.1 Electronic Structure Theory

#### 2.1.1 Many-body Schrödinger Equation

The macroscopic properties of bulk materials are governed by classical mechanics. The physical properties of materials fundamentally differ when material size shrinks to nano-scale, and classical mechanics is insufficient to describe the behaviour of materials at that scale. Quantum effects dictate the behaviour of these materials. So, quantum mechanics, which can predict the behaviour of microscopic particles including molecules, atoms, and sub-atomic particles, is required to deal with low dimensional materials and nano-scale materials. The dynamics of a quantum mechanical system are governed by the Schrödinger equation via the wave function. Any isolated system in a non-relativistic, stationary state can be represented by the time-independent Schrödinger equation,

$$\hat{H}\Psi = E\Psi \tag{2.1}$$

where  $\Psi$  is the state vector of the quantum system,  $\hat{H}$  is the Hamiltonian operator which represents total energy, and  $E$  is the energy of the system. Hamiltonian operator of a many electron system consisting of  $M$  nuclei and  $N$  electrons can be written as

$$\hat{H} = \hat{T}_N + \hat{T}_e + \hat{V}_{e-e} + \hat{V}_{N-e} + \hat{V}_{N-N} \quad (2.2)$$

Here  $\hat{T}_N$  and  $\hat{T}_e$  represent kinetic energy operators of nuclei and electrons respectively.  $\hat{V}_{e-e}$ ,  $\hat{V}_{N-e}$ , and  $\hat{V}_{N-N}$  denote potential energy operators of electron-electron interaction, nucleus-electron interaction, and nucleus-nucleus interaction. The kinetic energy operators can be written as

$$\hat{T}_N + \hat{T}_e = -\frac{\hbar^2}{2} \sum_{I=1}^M \frac{1}{M_I} \nabla_I^2 - \frac{\hbar^2}{2m_e} \sum_{i=1}^N \nabla_i^2 \quad (2.3)$$

and potential energy operators can be written as

$$\begin{aligned} \hat{V}_{N-N} + \hat{V}_{N-e} + \hat{V}_{e-e} &= \frac{e^2}{4\pi\epsilon_0} \sum_{I=1}^M \sum_{J>I}^M \frac{Z_I Z_J}{|R_I - R_J|} - \frac{e^2}{4\pi\epsilon_0} \sum_{i=1}^N \sum_{I=1}^M \frac{Z_I}{|R_I - r_i|} \\ &+ \frac{e^2}{4\pi\epsilon_0} \sum_{i=1}^N \sum_{j>i}^N \frac{1}{|r_i - r_j|} \end{aligned}$$

Here,  $I$  and  $J$  run over the  $M$  nuclei while  $i$  and  $j$  denote the  $N$  electrons in the system. In the atomic unit, i.e., by setting atomic constants such as  $e$ ,  $m_e$ ,  $\hbar$ , and  $4\pi\epsilon_0$  to 1, total Hamiltonian can be written as

$$H = -\frac{1}{2} \sum_{I=1}^M \frac{1}{M_I} \nabla_I^2 - \frac{1}{2} \sum_{i=1}^N \nabla_i^2 + \sum_{I=1}^M \sum_{J>I}^M \frac{Z_I Z_J}{|R_I - R_J|} - \sum_{i=1}^N \sum_{I=1}^M \frac{Z_I}{|R_I - r_i|} + \sum_{i=1}^N \sum_{j>i}^N \frac{1}{|r_i - r_j|} \quad (2.4)$$

The corresponding Schrödinger equation must be solved to obtain the energy levels of a molecule. Since the equation depends on the number of nuclei and electrons in the molecule, it becomes difficult solving the Schrödinger equation as the number of electrons and nuclei in the molecule increases. For example, benzene which is having 12 nuclei and 42 electrons requires to solve  $3 \times 12 + 3 \times 42 = 36$  nuclear + 126 electronic = 162 variables for the wave function. This shows it is practically impossible to solve the Schrödinger equation for such molecules having a large number of electrons and nuclei. The necessity of approximations is well demonstrated by such a scenario.

## 2.1.2 Born-Oppenheimer Approximation

Born-Oppenheimer approximation (BO approximation) is one of the most fundamental approximations in molecular dynamics. The approximation is based on the fact that the nuclei are much heavier than the electrons. So, nuclei are nearly fixed concerning electronic motion. Considering this, BO approximation express total wave function as the product of electronic and nuclear wave function, by neglecting the cross terms between electrons and nuclei,

$$\Psi_{total} = \Psi_n \Psi_e \quad (2.5)$$

The decoupled and smaller wave functions can be solved more effectively. BO approximation removes the kinetic energy of the nucleus from the Hamiltonian, which is negligible compared to that of the electron. Furthermore, nuclear positions are considered as a fixed parameter in the remaining Hamiltonian. For a fixed nuclear position,  $\hat{V}_{N-N}(R)$  acts as a constant, which shifts eigenvalue by a constant value. So,  $\hat{V}_{N-N}(R)$  can be excluded from the electronic Hamiltonian. After applying these approximations, the total Hamiltonian is reduced to a Hamiltonian containing only electron's variables called electronic Hamiltonian,

$$\hat{H}_e = \hat{T}_e(r) + \hat{V}_{N-e}(r, R) + \hat{V}_{e-e}(r) \quad (2.6)$$

Corresponding electronic Schrödinger equation is

$$\hat{H}_e \Psi_e = E_e \Psi_e \quad (2.7)$$

Here the electronic eigen value  $E_e$  depends on the chosen nuclear position  $R$ . Electronic Schrödinger equation can be solved repeatedly by varying nuclear position,  $R$ , and it gives  $E_e$  as a function of  $R$ .

BO approximation helps to calculate the electronic structure of a molecule without bothering too much about the nuclei and simplifies the calculation. For benzene, the BO approximation reduces the number of variables for the wave function from 162 to 126.

## 2.1.3 Hartree-Fock approximation

Even after implying BO approximation, solving the Schrödinger equation for an atom with  $N$  electrons is a heavy computational task since it contains numerous electron-electron repulsion terms. In order to calculate electron-electron repulsion,

the wave functions for the other electrons must be known and vice versa. D. R. Hartree introduced such a method called the self-consistent field (SCF) method. Later, V. Fock and J. C. Slater improved this method and formulated Hartree-Fock self-consistent field (HF-SCF) approach.

D.R. Hartree introduced an approximation in which this many-body problem is treated as a single particle problem. In this method, the N-electron wave function is approximated by an antisymmetrized product of N one-electron wave functions  $\psi_i(r_i)$ . This product is usually referred to as a Slater determinant. By using the variational method, one can derive a set of N-coupled equations for the N spin orbitals. Hartree-Fock wave function and energy of the system can be obtained by solving these equations.

Since there are no known analytical solutions for many-electron systems, the problem is solved numerically. The equations are solved using a non-linear method. The Schrödinger equation is solved for one electron, and then the procedure is repeated for other electrons. After the first computation, a set of improved wave functions as the basis set for electrons is obtained. The computation is now repeated with the new set of wave functions for each electron. A new set of wave function is obtained for each electron. The total energy and charge density are then calculated using the new wave function and compare it with the energy and charge density calculated in the previous computational cycle. The process was continued self-consistently until the threshold accuracy was reached.

The Hartree-Fock approximation is considered as the simplest sophisticated approach for solving the many-body Schrödinger equation as described in the Born-Oppenheimer approximation. Nevertheless, the computational effort is still very high, which is enough to make the calculation of a large system impossible. On the other hand, the electronic correlation is not fully taken into account in this method. Thus the resulting energy turned out to be erroneous.

#### 2.1.4 Density Functional Theory (DFT)

It was realized that the wave function approach presented by Schrödinger would be difficult to solve for a system having a large number of electrons. Density functional theory (DFT) is an alternate approach that systematically maps a many-body problem with an electron-electron interaction energy operator to a single body problem without an electron-electron interaction energy operator. The DFT considers electron density ( $\rho(\mathbf{r})$ ), which is the measure of the probability of an electron being present at a specific location, as the key variable. The properties

of a many-body system are determined as the functional (function of a function) of spatially dependent electron density.

DFT has its root in the Thomas-Fermi method, which is a quantum mechanical theory for the electronic structure calculations of many-body systems formulated in terms of electronic density (Thomas, 1927). Although the Thomas-Fermi theory provides a detailed prescription for computationally handling the large many-electron systems, it failed to achieve acceptance due to its poor prediction accuracy. After three and a half decades, Walter Kohn and Pierre C. Hohenberg put forward two theorems on electron density which are considered as the theoretical foundation of DFT (Hohenberg and Kohn, 1964). Those are known as Hohenberg–Kohn (H-K) theorems.

### **The First Hohenberg-Kohn Theorem**

The first H-K theorem establishes that the ground-state properties of a many-electron system are uniquely determined by an electron density that relies solely on three spatial coordinates. By introducing the electron density, the dependency on  $3N$  spatial coordinates of an  $N$  electron system reduces to 3 spacial coordinates of electron density.

### **The Second Hohenberg-Kohn Theorem**

The first theorem states that the ground-state electron density is sufficient to determine all properties of the system. However, there arises a question, how to generate the ground state charge density and how one can be sure that the obtained density is really the ground state density. The second Hohenberg-Kohn theorem answers these queries. The second theorem states that the energy functional delivers the lowest energy of the system if and only if the input density is the true ground state density. And the ground state charge density can be obtained by applying the variational principle.

### **2.1.5 Kohn-Sham DFT**

The Hohenberg-Kohn theorem was used by Walter Kohn and Lu Jeu Sham (Kohn and Sham, 1965) to develop a suitable method to carry out electronic structure calculations of a many-electron system. Kohn and Sham proposed to deal with a non-interacting system instead of an interacting many-electron system. For that

purpose, a fictitious non-interacting system is constructed in such a way that its density should be the same as that of the interacting electrons. Therefore, instead of finding the universal H-K functional, Kohn-Sham DFT finds the fictitious system of non-interacting electrons and systematically improves it by means of the variational principle. Since the expression for the kinetic energy of non-interacting electrons is known, there is no need to approximate kinetic energy functionals of the density. The only approximation one needs to do is on the exchange-correlation part of the potential. Hence appropriate approximation of exchange-correlation potential offers a more accurate electronic structure result.

In the exact electronic Hamiltonian,

$$\hat{H}_e = \sum_{i=1}^N -\frac{1}{2}\nabla_i^2 + \sum_{i=1}^N V_{ext}(r_{ij}) + \sum_{i=1}^N \sum_{j>i}^N \frac{1}{|r_i - r_j|}$$

the interaction term,  $\frac{1}{|r_i - r_j|}$  can not be broken into a sum of terms containing only  $r_i$  and  $r_j$ . However, if electrons are considered as non-interacting, the term can be replaced with a one-electron operator  $V_{av}$ , that describes the ‘‘average’’ effect of the interaction. Moreover, in the case of the non-interacting electrons, the Hamiltonian operator is simply a sum of one-electron operators.

$$\begin{aligned} \hat{H}_{eff} &= \sum_{i=1}^N -\frac{1}{2}\nabla_i^2 + \sum_{i=1}^N V_{ext}(r_i) + \sum_{i=1}^N V_{av}(r_i) \\ &= \sum_{i=1}^N -\frac{1}{2}\nabla_i^2 + \sum_{i=1}^N (V_{ext}(r_i) + V_{av}(r_i)) \\ &= \sum_{i=1}^N -\frac{1}{2}\nabla_i^2 + \sum_{i=1}^N V_{eff}(r_i) \\ &= \sum_{i=1}^N \left(-\frac{1}{2}\nabla_i^2 + V_{eff}(r_i)\right) \\ \hat{H}_{eff} &= \sum_{i=1}^N \hat{h}(r_i) \end{aligned}$$

Applying the variational principle, the functional form of the  $V_{eff}(r_i)$  can be obtained as

$$v_{eff}(r) = v_{ext}(r) + \int \frac{\rho(r')}{|r - r'|} dr' + v_{xc}[\rho(r)]$$

$$\hat{H}_{eff} = \sum_{i=1}^N \hat{h}(r_i) \quad (2.8)$$

That is, the entire Hamiltonian is the sum of all the one-electron Hamiltonians. We can write the Schrödinger equation for one-electron separately,

$$\hat{h}(r_i)\psi_a(r_i) = \epsilon_a\psi_a(r_i) \quad (2.9)$$

The wave function of a single electron is the molecular orbital which is also known as Kohn-Sham orbitals. Kohn-Sham orbitals and orbital energy are obtained from the above equation, known as the Kohn-Sham equation.

The electron density matrix  $\rho(r)$  is determined from the Kohn-Sham orbitals,  $\psi_i$

$$\rho(r) = \sum_{i=1}^N |\psi_i|^2$$

The term  $v_{xc}(\rho)$  is the exchange correlation potential can be obtained by using different approximations. In the case of LDA, we approximate it by means of homogeneous electron gas of constant density and corresponding exchange correlation energy is

$$E_{XC} = \int \rho(r)\epsilon_{XC}[\rho(r)]dr$$

The Kohn-Sham equations are solved in a self-consistent way. Initially, a charge density is needed to calculate  $E_{XC}$ . To obtain charge density, an initial guess to the Kohn-Sham orbitals is needed. The initial guess can be obtained from a set of basis functions.  $V_{XC}$  is computed from  $E_{XC}$ . The Kohn-Sham equations are then solved to obtain an improved set of Kohn-Sham orbitals. These orbitals are then used to calculate a better density. This process is repeated until the exchange-correlation energy and the density converge to within some tolerance.

Although developed in the 1960s, DFT began to be widely used in the 1990s. It was the developments that came in exchange-correlation functionals (Lee et al., 1988; Becke, 1993; Perdew et al., 1996; Heyd et al., 2003) that enabled the Kohn-Sham DFT method to provide a more accurate result. Kohn-Sham DFT is now the most common approach used for electronic structure calculation in chemistry, materials science, and other related fields (Lin et al., 2019). Walter Kohn was awarded Nobel Prize for Chemistry in 1998 for his contribution to developing the

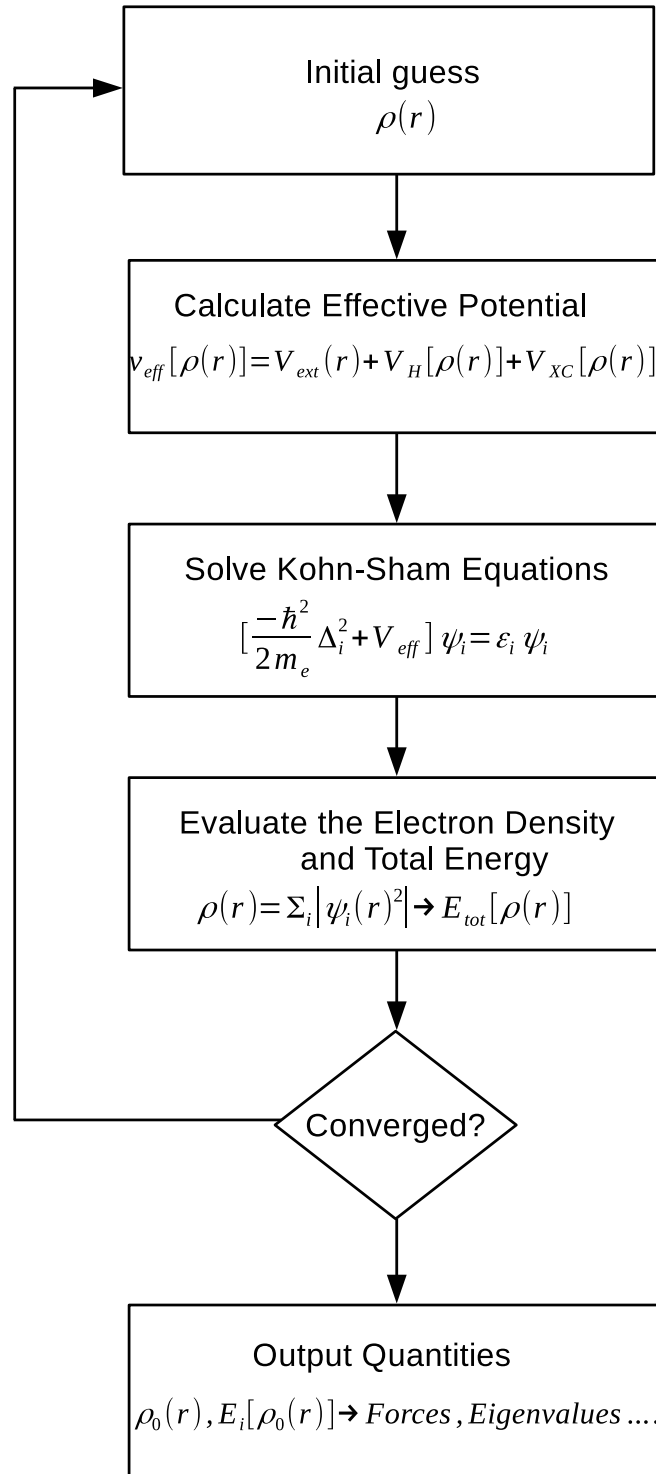


Fig. 2.1: A flow chart of the Kohn-Sham iteration scheme.

DFT.

DFT had a crucial role in accelerating research in the field of material science. What endears the DFT to material science researchers is the ability to precisely understand complex molecular mechanisms and accurately predict their behaviour



through low computational effort.

By the middle of 2000, many open or commercial software packages such as VASP (Kresse and Furthmüller, 1996), SIESTA (Soler et al., 2002), CASTEP (Clark et al., 2005), Qbox (Gygi, 2008), FHI-aims (Blum et al., 2009), NWChem (Valiev et al., 2010), Molpro (Werner et al., 2012), ABINIT (Gonze et al., 2016), Quantum ESPRESSO (Giannozzi et al., 2017), and Quantum ATK (Smidstrup et al., 2019) were developed which calculated electronic structure properties of many body systems by implementing DFT. The availability of these robust and mature software packages also have a prominent role in the widespread application of DFT.

DFT method is adapted to study the electronic structure of various materials required for this work. Various DFT based softwares adopted for electronic structure calculations are VASP, SIESTA, Quantum Espresso, and Quantum ATK.

## 2.2 Quantum Transport

The transport of electrons through a device is a mechanism that needs a different theoretical approach and understanding than what we have discussed so far. It needs to describe excited states, dynamics of the system, and non-equilibrium conditions. DFT, which is a mean-field-based many-body theory of the ground state, is not sufficient to study the transport mechanism.

Spin-polarized transport through the nano-scale magnetic junction is very sensitive to the chemical and material details of the device. It is important to understand the transport mechanism of electrons and spin in nano-scale magnetic junctions.

It has been over a century since humanity began to think about how electrons transport, what factors influence them, how they can be controlled, how we can utilize them, how we can build the variety of utilities we need, and how we can improve it. Although electron has charge and spin properties, the charge is the first to be understood and utilized. In the case of transport properties too, charge transport has been studied first.

The first milestone in the transport theory in the solid-state is the Drude-Sommerfeld model. In 1927 Arnold Sommerfeld developed the theory by combining quantum mechanical Fermi–Dirac statistics and the classical Drude model. According to this model, electrons near the Fermi energy level take part in conduc-

tion, and the conduction electrons are scattered randomly after a given relaxation time. Electron transport, in this case, is described by Ohm's law (Sommerfeld and Bethe, 1933). Conductance  $G$  is related to the cross-sectional area  $A$  and length  $L$  by the relation

$$G = \frac{\sigma A}{L}$$

where  $\sigma$  is the conductivity of the material. According to the above relation, resistance decreases with a decrease in the length of the channel. But this relation does not have to be valid in every case. The size of the conductor is also an important factor.

### 2.2.1 Ballistic transport

When the size of the conductors is much greater than the Fermi wavelength and still shorter than the electrons mean free path and coherent length, they are called mesoscopic conductors. It shows novel conduction properties. An electron in this conductor can propagate without any scattering. Therefore resistance is independent of the conductor's length. This type of electron transport is called ballistic transport (Fig. 2.2).

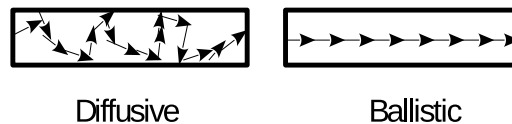


Fig. 2.2: Schematic representation of motion of electrons in a diffusive channel and in a ballistic channel.

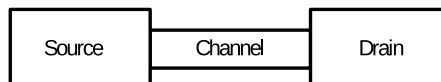


Fig. 2.3: Schematic representation of a mesoscopic channel connected to source and drain.

Consider a mesoscopic material connected to 2 large reservoirs or electrodes (Fig. 2.3). The difference in electronic distribution gives rise to a non-equilibrium condition. The difference in electrode's electronic distributions can be due to a chemical potential difference, electronic temperature difference, or a combination of both. The electrode which is having a higher potential acts as the source and the one having a less potential acts as the drain. The non-equilibrium between source and drain develops a current flow, and the mesoscopic material connected in between acts as the channel for the current. Current flowing through the channel depends on the density of states available in the channel. The only energy region that takes part in the conduction is that in between  $\mu_1$  and  $\mu_2$  (Fig. 2.4).

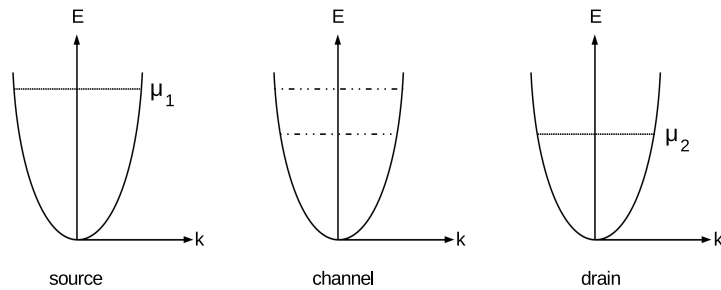


Fig. 2.4: E-k diagram for source, channel and drain. Chemical potential of source is  $\mu_1$  and that of drain is  $\mu_2$ .

The overall bandstructure can be considered as a series of 1D sub-bands, each corresponding to a different transverse mode, much like an electromagnetic waveguide. Electron motion within each 1D sub-band then consists of left-movers ( $-k$  states) and right-movers ( $+k$  states).

Consider a single transverse mode where  $+k$  states are occupied according to some function  $f^+(E)$ . A uniform electron gas moving with a velocity  $v$  carries a current  $nev$  in unit length. So, current carried by  $+k$  states in a conductor of length  $L$  is

$$I^+ = \frac{e}{L} \sum_k v f^+(E) = \frac{e}{L} \sum_k \frac{1}{\hbar} \frac{dE}{dk} f^+(E) \quad (2.10)$$

Assuming periodic condition, sum over  $k$  can be converted into an integral.

Including degenerate electron with opposite spin, current for  $M$  modes is

$$I^+ = \frac{2e}{h} \int_{-\infty}^{\infty} M(E) f^+(E) dE \quad (2.11)$$

Here  $e$  and  $\hbar$  represent the charge of the electron and Planck's constant, respectively.

Assuming the number of modes  $M$  is constant over the energy range  $\mu_1 > E > \mu_2$ ,

$$I = \frac{2e^2}{h} M \frac{(\mu_1 - \mu_2)}{e} \quad (2.12)$$

$$\Rightarrow G_C = \frac{2e^2}{h} M \quad (2.13)$$

$G_C$  is the conductance. So, contact resistance is given by

$$G_c^{-1} = \frac{h}{2e^2 M} \approx \frac{12.9 k\Omega}{M} \quad (2.14)$$

Contact resistance decreases with an increase in the number of modes. For wide conductors having thousands of modes, contact resistance will be negligible.

Equation 2.13 shows that unlike classical case, conductance of a ballistic conductor is independent of conductor's length and it is a discrete multiple of  $\frac{2e^2}{h}$ .  $\frac{2e^2}{h}$  is called quantum of conductance (Fig. 2.5). This discrete nature of conductance is significant only when the width of the conductor becomes comparable to the Fermi wavelength. When the width of the conductor is much greater than the Fermi wavelength number of modes will be a large value. So, discreteness of conductance is not evident.

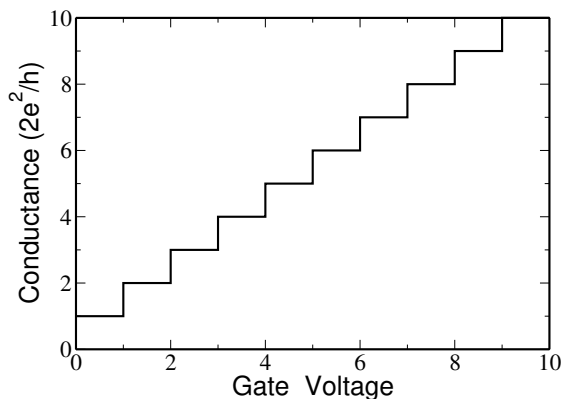


Fig. 2.5: Point contact conductance as a function of gate voltage. Here the conductance is quantized.

## 2.2.2 Landauer's formula

Rolf Landauer incorporated the features of ballistic conductors to the other conductors. He considered a conductor connected to 2 large contacts by 2 leads as shown in Fig. 2.6. Leads are assumed to be ballistic conductors each having  $M$  transverse modes.  $T$  is the average probability that the electron in the lead 1 will transmit to lead 2. Assuming contacts are reflectionless, electrons can exit from the conductor into contacts without any reflections.

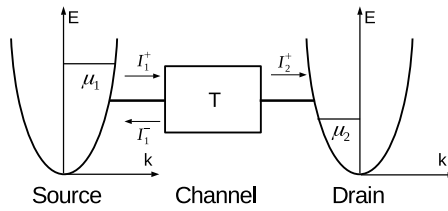


Fig. 2.6: Conductor connected to source and drain by ballistic leads.

The influx of electrons from lead 1 is given by

$$I_1^+ = \frac{2e}{h} M [\mu_1 - \mu_2]$$

Out-flux from lead 2 depends on the transmission probability  $T$ .

$$I_2^+ = \frac{2e}{h} M T [\mu_1 - \mu_2]$$

The rest of the flux is reflected back to contact 1.

$$I_1^- = \frac{2e}{h} M (1 - T) [\mu_1 - \mu_2]$$

The net current flowing at any point in the device is given by

$$I = I_1^+ - I_1^- = I_2^+ = \frac{2e}{h} M (1 - T) [\mu_1 - \mu_2]$$

Hence the conductance is equal to

$$G = \frac{I}{(\mu_1 - \mu_2)/|e|} = \frac{2e^2}{h}MT \quad (2.15)$$

This is called Landauer's formula.

Landauer's formula considers a two-terminal device. This can not be applied directly to multi-terminal devices. There may arise different problems. Terminals may couple differently to  $\pm k$  states, an additional source of scattering can be produced, and interference of waves can take place. In 1985 Büttiker proposed a method to solve this problem (Büttiker, 1986). He showed that one could treat all the probes on an equal footing and extend the two-terminal linear response Landauer's formula to multi-terminal devices by summing over all probes.

$$I_p = \frac{2e}{h} \sum_q [T_{q \leftarrow p} \mu_p - T_{p \leftarrow q} \mu_q]$$

Here  $T_{q \leftarrow p} = M_{q \leftarrow p} T_{q \leftarrow p}$  is the product of transmission probability  $T$  from contact  $p$  to contact  $q$  and number of transverse modes  $M$  between them, is called transmission function. One can describe current flow through a conductor in terms of transmission function. This generalization of the Landauer formula for multiple probes is known as Landauer-Büttiker formalism. It is considered a milestone in mesoscopic physics. It has been widely used in the interpretation of mesoscopic experiments.

If the size of the conductor is much smaller than the phase relaxation length, then transport is said to be coherent, and one can calculate transmission function starting from Schrödinger equation. If the size of the conductor is large, then it can be divided into several coherent conductors and combined incoherently.

### 2.2.3 Scattering Matrix

A coherent conductor can be characterized at each energy by a scattering matrix ( $S$  matrix). It relates outgoing wave amplitude to the incoming wave amplitude at the different leads. Consider a coherent conductor connected to 2 large contacts as shown in Fig. 2.7. Lead connecting left contact and conductor has two propagating modes. Whereas lead connecting right contact and conductor has only one mode. One can represent outgoing waves in terms of incoming waves, as given below.

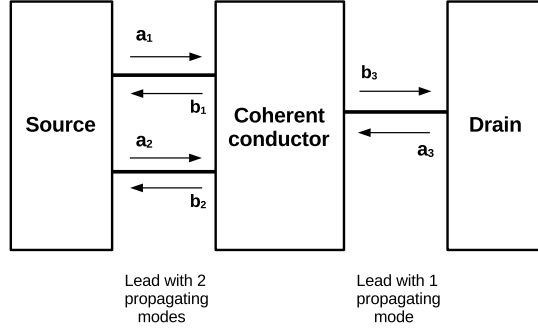


Fig. 2.7: Schematic representation of scattering at a coherent conductor.

$$\begin{bmatrix} b_1 \\ b_2 \\ b_3 \end{bmatrix} = \begin{bmatrix} s_{11} & s_{12} & s_{13} \\ s_{21} & s_{22} & s_{23} \\ s_{31} & s_{32} & s_{33} \end{bmatrix} \begin{bmatrix} a_1 \\ a_2 \\ a_3 \end{bmatrix}$$

Total number of modes is obtained by summing the number of modes in each lead.

$$M_T(E) = \sum_p M_p(E)$$

where  $M_p(E)$  is the total number of propagating modes at lead  $p$  at a given energy. The scattering matrix is of dimension  $M_T \times M_T$ . In principle scattering matrix can be calculated using the Schrödinger equation if potential inside the conductor is known. For a coherent conductor, one can define and calculate a scattering matrix. The transmission probability can be obtained by taking the squared magnitude of the corresponding elements of the  $S$  matrix.

$$T_{n \leftarrow m} = |S_{n \leftarrow m}|^2 \quad (2.16)$$

Transmission function will be the sum of transmission probability  $T_{n \leftarrow m}$  over all modes  $n$  in the lead  $p$  and all modes  $m$  in the lead  $q$ .

$$T_{q \leftarrow p} = \sum_{m \in q} \sum_{n \in p} T_{n \leftarrow m}$$

$S$  matrix tells the response at one lead due to excitation at another. So, it's convenient to incorporate Green's function here. Green's function  $G(r, r')$  gives the response at any point  $r$  due to excitation at any point  $r'$ . This concept

provides a convenient method for calculating the  $S$  matrix of arbitrarily shaped conductors. And it is also helpful in relating the scattering theory to other formalisms. Green's function method will be more convenient when any interactions like electron-electron interaction or electron-phonon interaction are needed to be included. These interactions will give rise to excitations within the conductor and can not be described by a simple  $S$  matrix.

## 2.2.4 Non-Equilibrium Green's Function (NEGF) Theory

Consider a conductor, connected to contacts through a set of semi infinite ballistic leads in which available states are fully occupied upto reservoir's chemical potential. So, these leads are enough to represent reservoirs' influence. And the transmission in a contact-lead-conductor-lead-contact system is equivalent to that in a lead-conductor-lead system. So, for the simplification of calculation can be represented by the system as shown in Fig. 2.8. An excitation due to left contact gives rise to a wave  $Ae^{ikna}$  towards the conductor. The wave travelling towards the conductor is scattered by the conductor into different leads. A portion of the incident wave will get transmitted through the conductor. Let it be  $A\tau e^{ikna}$ . Reflected portion of the wave can be expressed as  $A\rho e^{-ikna}$ .

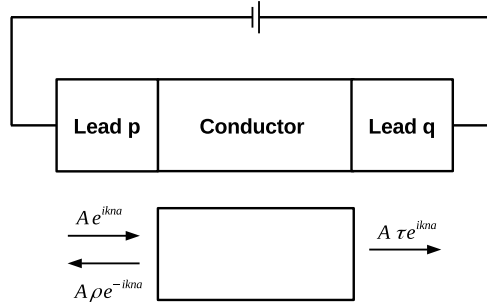


Fig. 2.8: Schematic representation of a conductor connected to reservoirs through a set of semi-infinite ballistic leads.

Here a response occurs at one lead due to the excitation at another. Whenever the response  $R$  is related to the excitations  $S$  by a differential operator  $D$

$$DR = S$$



So, Green's function can be introduced by the relation

$$R = GS$$

where  $G \equiv D^{-1}$

The given situation can be expressed in the form,

$$S + H\psi = E\psi$$

$$[E - H]\psi = S$$

where  $\psi$  is the wave function,  $S$  is an equivalent excitation term due to wave incident from one of the lead and  $H$  is the Hamiltonian operator. Green's function corresponding to this is

$$G = [E - H]^{-1}$$

For a one dimensional system with constant potential energy  $U_0$  and zero vector potential,

$$G = [E - U_0 + \frac{\hbar^2}{2m} \frac{d^2}{dx^2}]^{-1}$$

that is,

$$[E - U_0 + \frac{\hbar^2}{2m} \frac{d^2}{dx^2}]G(x, x') = \delta(x - x')$$

Comparing it with Schrödinger equation,

$$(E - U_0 + \frac{\hbar^2}{2m} \frac{d^2}{dx^2})\psi(x) = 0$$

The Green's function  $G(x, x')$  can be viewed as the wave function at  $x$  resulting from a unit relaxation applied at  $x'$ . Physically such an excitation is expected to give rise to 2 waves travelling outward from the point of excitation with amplitude  $A^-$  and  $A^+$  as shown in Fig. 2.9.

We can write

$$G(x, x') = A^+ e^{ik(x-x')}, x > x'$$

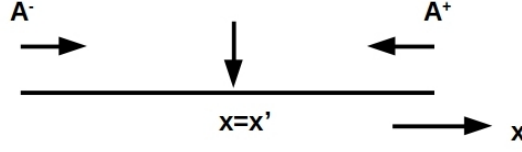


Fig. 2.9: Retarded Green's function for an infinite 1-D wire.

$$G(x, x') = A^- e^{-ik(x-x')}, x < x'$$

Solving this will give,

$$G(x, x') = \frac{-i}{\hbar\nu} e^{ik(x-x')}$$

where  $\nu \equiv \frac{\hbar k}{m}$ . Another solution is also possible. That will be

$$G(x, x') = \frac{i}{\hbar\nu} e^{-ik(x-x')}$$

This solution represents incoming wave to the point  $x = x'$  and disappears at that point. These solutions are called advanced Green's function  $G^A$  and retarded Green's function  $G^R$  respectively. Here the Hamiltonian does not consider the boundary condition. One way to consider the boundary condition itself to the equation is to add an infinitesimal imaginary part to the energy. Including this the equation becomes

$$[E - U_0 + \frac{\hbar^2}{2m} \frac{d^2}{dx^2} + i\eta] G^R(x, x') = \delta(x - x')$$

for retarded Green's function.

For advanced Green's function it will be

$$[E - U_0 + \frac{\hbar^2}{2m} \frac{d^2}{dx^2} - i\eta] G^A(x, x') = \delta(x - x')$$

So in general retarded Green's function can be defined as

$$G^R = [E - H + i\eta]^{-1} (\eta \rightarrow 0^+)$$

The advanced Green's function will be

$$G^A = [E - H - i\eta]^{-1} (\eta \rightarrow 0^+)$$

Consider conductor as a periodic lattice whose points are located at  $x = ja$ ,  $j$  being an integer. The Hamiltonian operator for the conductor will be

$$[H] = \frac{-\hbar^2}{2m} \frac{d^2}{dx^2} + U(x)$$

Using the method of finite differences,

$$\begin{aligned} \left[ \frac{d\psi}{dx} \right]_{x=j} &\rightarrow \frac{1}{a} [\psi_{j+\frac{1}{2}} - \psi_{j-\frac{1}{2}}] \\ \left[ \frac{d^2\psi}{dx^2} \right]_{x=j} &\rightarrow \frac{1}{a^2} [\psi_{j+1} - 2\psi_j + \psi_{j-1}] \end{aligned}$$

Using this relation, Hamiltonian of the conductor can be written as,

$$[H\psi]_{x=j} = (U_j + 2t)\psi_j - t\psi_{j-1} - t\psi_{j+1} \quad (2.17)$$

where  $t \equiv \frac{-\hbar^2}{2ma^2}$

Introducing tight binding approximation, equation 2.17 can rewrite as

$$[H\psi(x)]_{x=j} = \sum_i H(j, i)\psi_i$$

where

$$\begin{aligned} H(j, i) &= U_i + 2t, \text{ if } j=i \\ &= -t, \text{ if } i \text{ and } j \text{ are nearest neighbours} \\ &= 0, \text{ otherwise} \end{aligned}$$

Corresponding matrix representation is as,

$$H = \begin{bmatrix} \dots & -t & 0 & 0 & 0 \\ -t & U_{-1} + 2t & -t & 0 & 0 \\ 0 & -t & U_0 + 2t & -t & 0 \\ 0 & 0 & -t & U_1 + 2t & -t \\ 0 & 0 & 0 & -t & \dots \end{bmatrix} \quad (2.18)$$

Here  $U_j + 2t$  represents the energy of orbital localised at site  $j$  while  $t$  ( $\equiv \frac{\hbar^2}{2ma^2}$ ) represents hopping matrix element.

In the same manner, Hamiltonian can extend to 2 or more dimensions.

$$\begin{aligned} [H]_{ij} &= U - r_i + zt, \text{ if } i=j \\ &= -t_{ij}, \text{ if } i \text{ and } j \text{ are nearest neighbours} \\ &= 0, \text{ otherwise} \end{aligned}$$

where  $z$  is the number of nearest neighbours. It is 2 for linear chain and 4 for a square lattice.  $r_i$  is the position vector for lattice site  $i$ .

Hamiltonian matrix obtained can be used in the Green's function equation

$$G^R = [(E + i\eta)I - H]^{-1} \quad (2.19)$$

Since our system consists of infinite leads, it is not easy to perform the numerical calculations with an infinite Hamiltonian. So, another simplification is introduced. We consider only the scattering region and effect of leads that are included through self-energy,  $\Sigma$ .

Consider a conductor connected to lead  $p$ . We can partition the overall Green's function into sub-matrices.

$$\begin{bmatrix} G_p & G_{pC} \\ G_{Cp} & G_C \end{bmatrix} = \begin{bmatrix} (E + i\eta)I - H & \tau_p \\ \tau_p^+ & EI - H_C \end{bmatrix}^{-1}$$

Sub-matrices represent lead ( $G_p$ ), conductor ( $G_C$ ) and coupling between lead and conductor ( $G_{Cp}$ ).

An expression for sub-matrix  $G_C$  can be derives as,

$$\begin{aligned} [(E + i\eta)I - H]G_{pC} + [\tau_p]G_C &= 0 \\ [EI - H_C]G_C + [\tau_p^+]G_{pC} &= I \end{aligned}$$

From these,

$$G_{pC} = -g_p^R \tau_p G_C$$

where,

$$g_p^R = [(E + i\eta)I - H_p]^{-1}$$

Here,  $(E + i\eta)I - H_p]^{-1}$  is the Green's function of the isolated lead and  $G_{pC}$  is the Green's function for isolated semi-infinite lead. Substituting  $G_{pC}$  in the equation for  $G_C$  gives,

$$G_C = [EI - H_C - \tau_p^+ g_p^R \tau_p]^{-1}$$

$G_C$  is a matrix of finite dimension  $C \times C$  where  $C$  is the number of points in the conductor. Infinite lead is also considered in  $G_C$  through  $\tau_p^+ g_p^R \tau_p$ .  $g_p^R$  represents Green's function for an isolated lead. It can be calculated analytically.

Coupling matrix  $\tau_p$  is zero for all points other than nearest neighbours  $p_i$  and  $p_j$ . So, the calculation of Green's function of isolated lead is limited at the contacts. At this point lead's self-energy can be introduced as,

$$\Sigma = \tau_p^+ g_p^R \tau_p$$

$$\tau(p_i, i) = t$$

So,

$$[\tau_p^+ g_p^R \tau_p]_{ij} = t^2 g_p^R(p_i, p_j)$$

The Green's function of the conductor can be written as

$$G_c^R = [EI - H_c - \Sigma^R]^{-1}$$

where,

$$\Sigma^R = \sum_p \Sigma_p^R \tag{2.20}$$

Green's function of the conductor  $G_C$  represents the propagation of electrons

between two points inside the conductor, taking the effect of leads into account through self-energy term  $\Sigma^R$ .

Consider a conductor connected to a set of leads  $p$  and  $q$ . The interface between lead  $p$  and conductor is defined by  $x_p = 0$ . Let  $G_{qp}^R$  denotes the Green's function between a point lying on the plane  $x_p = 0$  and  $x_q = 0$ . Unit excitation at  $x_p = 0$  gives rise to a wave of amplitude  $A_p^+$  towards the conductor and another wave of amplitude  $A_p^-$  away from the conductor. The wave travelling towards the conductor is scattered by the conductor towards different leads. So Green's function can be expressed in terms of scattering matrix  $S$ , connecting as

$$G_{qp}^R = \delta_{qp}A_p^- + S'_{qp}A_{qp}^+$$

where  $A_p^+ = A_p^- = \frac{-i}{\hbar\nu_p}$  and can define a matrix  $[S']$  in terms of the wave amplitude  $S'_{qp} = S_{qp}\sqrt{\frac{v_p}{v_q}}$ .

Hence,

$$S_{qp} = -\delta_{qp} + i\hbar\sqrt{\nu_q\nu_p}G_{qp}^R$$

This equation express S matrix in terms of Green's function. For a multi-moded system S matrix elements will be

$$S_{nm} = -\delta_{nm} + i\hbar\sqrt{\nu_n\nu_m} \int \int \chi_n(y_q)[G_{qp}^R(y_q; y_p)]\chi_m(y_p)dy_qdy_p$$

Transmission function is the square of scattering matrix.

$$|S_{nm}|^2 = \frac{\hbar^2\nu_n\nu_m}{a^2} \sum_{i,j,i',j'} \chi_n(q_i)G^R(j,i)\chi_m(p_i)\chi_n(q'_j)G^A(i',j')\chi_m(p'_i)$$

Using the relation  $G^A(i',j') = G^R(j',i')^*$  it can be written as,

$$\begin{aligned} T_{qp} &= \sum_{n \in q} \sum_{m \in p} |S_{nm}|^2 \\ &= \sum_{i,j,i',j'} \Gamma_q(j',j)G^R(j,i)\Gamma_p(i,i')G^A(i',j') \\ T_{qp} &= Tr[\Gamma_q G^R \Gamma_p G^A] \end{aligned}$$

where  $\Gamma_p(i,i') = \sum_{m \in p} \chi_m(p_i)\frac{\hbar\nu_m}{a}\chi_m(p'_i)$ . By using the expression for self

energy,

$$\Gamma_p = i[\Sigma_p^R - \Sigma_p^A]$$

where advanced self-energy ( $\Sigma_p^A$ ) is the Hermitian conjugate of the retarded self-energy ( $\Sigma_p^R$ ).

The effect of semi-infinite leads on the conductor is incorporated through self-energy  $\Sigma_p$ , which is a finite operator. The Green's function  $G^R$  and the coupling function  $\Gamma_p$  are explicitly obtained from self energies.

Under non-equilibrium conditions, the density matrix of the central region,  $\rho$ , is given by

$$\rho = \frac{i}{2\pi} \int_{-\infty}^{\infty} G^<(\epsilon) d\epsilon \quad (2.21)$$

This can be considered as a highlight of NEGF theory. Here,  $G^<(\epsilon)$  is calculated using the Keldysh equation

$$G^<(\epsilon) = G^R(\epsilon)\Sigma^<(\epsilon)G^A(\epsilon) \quad (2.22)$$

and

$$\Sigma^<(\epsilon) = i\Gamma_L((\epsilon) - qv_L)f((\epsilon) - \mu_L) + i\Gamma_R((\epsilon) - qv_L)f((\epsilon) - \mu_R) \quad (2.23)$$

where  $f(\epsilon)$  is the Fermi-Dirac distribution function,  $\mu_L$  and  $\mu_R$  are the chemical potentials of left and right leads, respectively.

The power of NEGF lies in equation 2.21, which includes all information of the non-equilibrium quantum statistics of the device.

Hence NEGF provides a method to calculate transport properties of a system under non-equilibrium conditions, which DFT alone can not do.

## 2.2.5 NEGF-DFT Formalism

A combination of DFT with NEGF is a more robust method to study the quantum transport of modelled devices. In this method, the electronic structure of a device is calculated within DFT, and the non-equilibrium quantum statistics that are

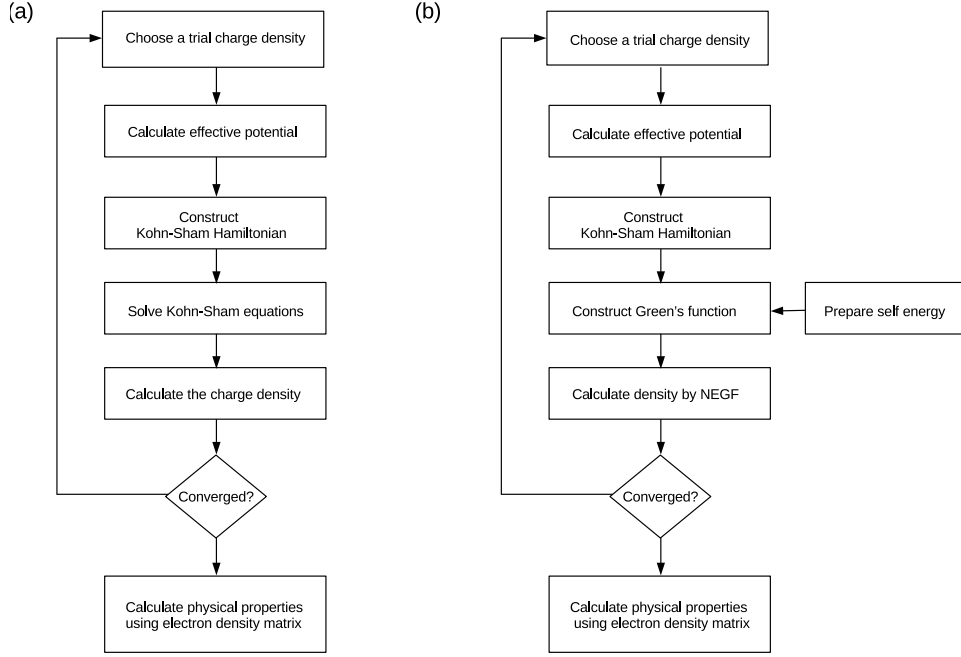


Fig. 2.10: Flowchart illustrating the self-consistent cycle in a) a standard DFT calculation, and b) a NEGF-DFT calculation.

needed to populate the electronic structure during current flow are determined using NEGF.

The NEGF-DFT formalism of electron transport is based on the Kohn–Sham equations, which presents the equation of motion of the electron through the one-electron Schrödinger equation,

$$\left[ \frac{-\hbar^2 \nabla^2}{2m} + V_{eff} \right] \psi_\alpha(r) = \epsilon \psi_\alpha(r) \quad (2.24)$$

where  $\psi_\alpha(r)$  and  $V_{eff}$  are the wave function of the electron in orbital  $\alpha$ , and DFT mean-field potential from the other electrons respectively.

The general two-probe device model discussed here is shown in Fig. 2.11. It consists of 3 regions. Two semi-infinite electrodes and a central scattering region (device region) sandwiched between the electrodes. It is assumed that electrodes have bulk properties. Few layers of electrode material are included in the device region in order to reduce scattering at the electrode-device region interface. In general, the device is x-y periodic, and transport is along the z-direction.

The properties of the electrodes are calculated first, using standard DFT techniques for periodic systems. The boundary conditions for the central region are determined by the solutions for electrodes. Then the central region is solved



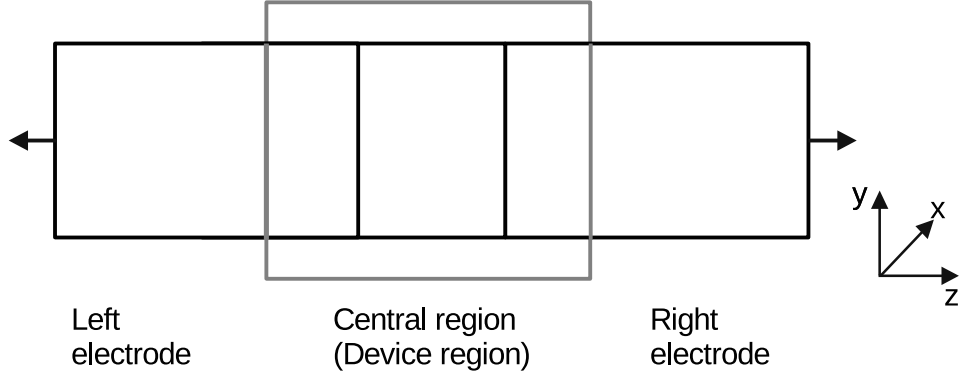


Fig. 2.11: Schematic diagram of a two-probe device model.

self-consistently (Stokbro, 2008).

The one-electron wave function  $\psi_\alpha$  can be expanded in terms of basis function  $\phi_i(r)$ , that are localized around each atom,

$$\psi_\alpha(r) = \sum_i c_{\alpha i} \phi_i(r) \quad (2.25)$$

where  $c_{\alpha i}$  denotes the expansion co-efficient. The one-electron Schrödinger equation (Equation 2.24) can be represented as a matrix equation,

$$Hc_\alpha = \epsilon_\alpha S c_\alpha \quad (2.26)$$

Here  $c_\alpha$ , H, and S are vectors of the expansion coefficients for orbital  $\alpha$ , Hamiltonian matrix, and overlap matrix respectively. The Hamiltonian matrix H and overlap matrix S are defined by,

$$H_{ij} = \int_v \phi_i(r) \left[ \frac{-\hbar^2 \nabla^2}{2m} + V_{eff} \right] \phi_j(r) dr \quad (2.27)$$

$$S_{ij} = \int_v \phi_i(r) \phi_j(r) dr \quad (2.28)$$

and these are block-diagonal matrices. The Hamiltonian matrix H can be separated into diagonal blocks,  $H_{LL}$ ,  $H_{CC}$ ,  $H_{RR}$ , and couplings  $H_{LC}$ ,  $H_{RC}$ .

Since the electrode region has periodic boundary conditions, the DFT method is used to calculate its properties. But, the central region, which is coupled to the left and right electrodes, requires the NEGF method to calculate its electron density. Retarded Green's function of the central part is defined through the matrix,

$$G_{CC}(\epsilon) = [(\epsilon + i\delta)S_{CC} - H_{CC} - \Sigma_{CC}^L - \Sigma_{CC}^R]^{-1} \quad (2.29)$$

Here  $\delta$  is an infinitesimal. The coupling between the central region and electrodes are described by the self-energy terms,  $\Sigma_{CC}^L$  and  $\Sigma_{CC}^R$ .

The density matrix,  $D_{ij}$  is obtained from the retarded Green's function. The density matrix at the equilibrium condition is,

$$D_{ij} = \frac{1}{\pi} \int_{-\infty}^{\mu} \text{Im}[G_{ij}(\epsilon)] d\epsilon \quad (2.30)$$

Here,  $\mu$  denotes the equilibrium chemical potential of the system. When there is an applied bias, the chemical potentials of left and right electrodes change, and a non-equilibrium condition arises. If the applied bias is  $V$ , then the chemical potential of left and right electrodes are related by  $\mu_L - \mu_R = eV$ . The corresponding matrix is,

$$D_{ij} = \frac{1}{\pi} \int_{-\infty}^{\mu_L} G(\epsilon) \text{Im}[\Sigma^L] G(\epsilon)^+ d\epsilon + \frac{1}{\pi} \int_{-\infty}^{\mu_R} G(\epsilon) \text{Im}[\Sigma^R] G(\epsilon)^+ d\epsilon \quad (2.31)$$

The density matrix gives electron density,

$$\rho(r) = \sum_{ij} D_{ij} \phi_i(r) \phi_j(r) \quad (2.32)$$

Using this  $\rho(r)$ , the KS-DFT equation will be solved in a self-consistent manner, and it gives new electron density. The self-consistent DFT solutions provide an adequate one-electron description of the system. Then the electron transport properties are calculated by using the Kohn–Sham Hamiltonian for propagating each electron. The total number of states propagating from left to right at a given energy is quantified by the transmission coefficient. The transmission coefficient  $T(\epsilon)$ , and electron occupation in the electrode reservoirs described by the Fermi function  $F(\epsilon)$ , determines the current through the device.

$$I = \frac{e}{h} \int_{-\infty}^{\infty} T(\epsilon) [F(\epsilon - \mu_L) - F(\epsilon - \mu_R)] d\epsilon \quad (2.33)$$

NanoDCal (Taylor et al., 2001), ATK (Brandbyge et al., 2002), MatDCal (Ning and Guo, 2008), and SMEAGOL (Clemmer and Davies, 2011) are certain widely used simulation softwares for quantum transport and device physics. In this work, the DFT-NEGF method implemented in TranSIESTA is used for the transport studies of modelled devices.

## 2.3 Transport Calculation Using TranSIESTA

TranSIESTA is a NEGF+DFT code handling device with one or multiple electrodes with individual chemical potentials and electronic temperatures (Papior et al., 2017). TranSIESTA uses a finite basis set. The system Hamiltonian is divided into three independent parts, which are known as the contact region (C), left electrode (L) and right electrode (R).

$$H_{TranSIESTA} = \begin{bmatrix} (H_L + \Sigma_L) & V_{LC} & 0 \\ V_{CL} & H_C & V_{CR} \\ 0 & V_{RC} & H_R + \Sigma_R \end{bmatrix}^{-1}$$

Here  $H_{L,R}$  are Hamiltonian matrices and  $\Sigma_{L,R}$  are self energies. The bulk electrode values in the L,R parts of the system Hamiltonian are computed separately from a previous bulk calculation of the electrodes with periodic boundary conditions. The interaction between the electrode-contact region  $V_{LC,RC}$  and the Hamiltonian of the contact region  $H_C$  are calculated explicitly with TranSIESTA Green's functions in an open boundary system.

### Calculation of Density Matrix

The density matrix is different at equilibrium condition (i.e. at zero bias) and at non-equilibrium condition (i.e. at finite bias).

(i) Equilibrium

At equilibrium, all Fermi distribution functions of electrodes are equal, i.e.,  $f_e(\epsilon) = f(\epsilon)$ . Green's function,  $G^<$  determines the density matrix by

$$D_{\mu\nu} = \frac{1}{2\pi i} \int d\epsilon G_{\mu\nu}^< = \int_{-\infty}^{\infty} d\epsilon \hat{\rho}_{\mu\nu} f(\epsilon - \mu_F)$$

where  $f(\epsilon)$  and  $\mu$  are Fermi distribution function and chemical potential. The spectral density matrix can be written as

$$\hat{\rho}(\epsilon) = \frac{1}{\pi} \text{Im}[G^R(\epsilon + i\delta)]$$

When electron-phonon interaction or phonon-phonon interactions are not taken into account  $G^<(\epsilon)$  can be expressed only in terms of  $G^R(\epsilon)$ .

$$G^R = [E.S - H - \Sigma_L(\epsilon) - \Sigma_R(\epsilon)]^{-1}$$

The density matrix for a real basis set  $\phi(r)$  is

$$\rho(r) = \Sigma_{\mu\nu} D_{\mu\nu} \phi_\mu(r) \phi_{\nu}^*(r)$$

(ii) Non-equilibrium

When a finite bias applies between electrodes, electrode potential at the left electrode ( $\mu_L$ ) and right electrode differs ( $\mu_R$ ), a non-equilibrium condition arises and current flows between electrodes.

The non-equilibrium density matrix is

$$D_{\mu\nu} = \int_{-\infty}^{\infty} d\epsilon (\hat{\rho}_{\mu\nu}^L f(\epsilon - \mu_L) + \hat{\rho}_{\mu\nu}^R f(\epsilon - \mu_R)) \quad (2.34)$$

where the spectral density matrix is given by

$$\rho_{\mu\nu}^L(\epsilon) = [G^R \frac{1}{\pi} \text{Im}[\Sigma_L] G^A]_{\mu\nu}$$

## 2.4 Spin Transport

For spin-dependent transport, modelling of the system is essentially the same as for the spin-independent case, except for the fact that we need to include the electron's spin degrees of freedom. For the spin-dependent case, electrodes are made of ferromagnetic materials.

The ability to inject a highly spin-polarized current into a semiconductor is the basic requirement for spin transport. The generic spin-electronic device consists of a ferromagnetic injector at one end, a semiconducting transport medium (either an

ordinary or magnetic semiconductor) in the middle, and a spin detector/magnetic drain at the other end. This should result in a conductance that depends on the relative magnetic orientation of the two contacts. It operates as follows: spin-polarized electrons are injected from a magnetic source (injector), manipulated, and controlled with a gate above the semiconducting transport medium before they are collected at the magnetic drain. To obtain a measurable spin-polarized current, the ratio of conductivity of ferromagnetic layer to that of medium/semiconductor should be less than or close to one ( $\frac{\sigma_{FM}}{\sigma_{SC}} \approx 1$ ) (Schmidt et al., 2000). It neglects spin scattering at interfaces.

In order to represent spin transport, the matrices used for the quantum transport have to be extended into spin-space. Each matrix element used in the non-spin formalism (Taylor et al., 2001) becomes a 2 x 2 matrix and those terms specify spin-up, spin-down, and the connection between the two spin spaces.

Introducing the spin-degree of freedom, the Hamiltonian and the Green's function of the device are now further subdivided into the following spin-dependent sub-matrices:

$$H_C = \begin{bmatrix} H_C^{\uparrow\uparrow} & H_C^{\uparrow\downarrow} \\ H_C^{\downarrow\uparrow} & H_C^{\downarrow\downarrow} \end{bmatrix} \quad (2.35)$$

$$G_C = \begin{bmatrix} G_C^{\uparrow\uparrow} & G_C^{\uparrow\downarrow} \\ G_C^{\downarrow\uparrow} & G_C^{\downarrow\downarrow} \end{bmatrix} \quad (2.36)$$

Then, Hamiltonian is solved self-consistently by solving Kohn-Sham equation. The self-consistent DFT calculation is illustrated in the flow chart given in Fig. 2.10. The spin-dependent exchange-correlation is considered for the calculation. The electron density,  $\rho$  is distinguished as spin-up density ( $\rho^\uparrow$ ) and spin-down density ( $\rho^\downarrow$ ) and total electron density,  $\rho = \rho^\uparrow + \rho^\downarrow$ . The self energy terms are also extended to spin-space. Thus, the transmission can be resolved into the different spin-channels. The spin dependent transmission co-efficient for the spin index  $\sigma$ (= $\uparrow$  or  $\downarrow$ ) can be expressed in the form

$$T_\sigma(E) = Tr[\Gamma_R^\sigma(E)G_R^\sigma(E)\Gamma_L^\sigma(E)G_R^{\sigma\dagger}(E)] \quad (2.37)$$

The spin-polarized current,  $I_{\uparrow(\downarrow)}$  through the device is,

$$I_{\uparrow(\downarrow)} = \frac{e}{h} \int_{-\infty}^{\infty} T_{\uparrow(\downarrow)}(E, V_b)[F(E - \mu_L) - F(E - \mu_R)]dE$$

## Conclusion

The detailed electronic structure calculations of the materials are a way to understand the properties and extract various other information about the material. The first principle methods followed to calculate electronic structure are discussed in this chapter. Kohn-Sham DFT is considered the most suitable method for the electronic structure calculation of a many-electron system. However, this method, which is limited to the periodic or finite system in equilibrium, is not sufficient to deal with the electron transport between source and drain. This chapter also discussed the electron transport mechanism through mesoscopic materials, which is different from electron transport through macroscopic materials. The non-equilibrium Green's function (NEGF) provides a theoretical framework for quantum transport. DFT combined with NEGF is considered a suitable method to predict the transport properties. Here, DFT is used to calculate tight-binding like Hamiltonian, and the NEGF formalism is used for obtaining the associated non-equilibrium density matrix. The effects of the semi-infinite leads with an externally applied bias voltage, are also included in this formalism. This chapter concludes with a comprehensive discussion on spin-dependent transport modeling in a device.

# Chapter 3

## Electronic Structure of Low Dimensional Materials

### 3.1 Introduction

Materials are the foundation stone for technology. It is essential to find suitable materials for the development of technology. And the selection is not possible without accurate knowledge of the fundamental properties of the materials. Therefore, it is essential to understand the fundamental properties of different materials and their changes in different conditions. The density of states and electronic band-structure are parameters that shed light on the material's fundamental properties. The density of states (DOS) of a material describes the number of energy states present in unit volume and energy, that electrons are allowed to occupy (Pillai, 2006). It is a predominant factor in determining the properties of materials (Yeo et al., 2019). The electronic band structure, which is another characteristic of a material, describes the energy and momentum of electrons in the material. This work aims to identify the potential 2D materials for spintronic applications. This chapter presents the result of the electronic structure study of 2D materials and their metal interface.

### 3.2 Methodology

The geometrical structures used for the electronic structure study are optimized using the density functional theory (DFT), as implemented in the Vienna Ab initio Simulation Program (VASP) package (Kresse and Furthmüller, 1996). The

generalized gradient approximation (GGA) by Perdew-Burke-Ernzerhof (PBE) is used for the exchange and correlation functional (Perdew et al., 1996). The energy cut-off for the plane-wave basis set was 450 eV, and  $12 \times 12 \times 1$  k-point sampling was used following the Monkhorst-Pack scheme.

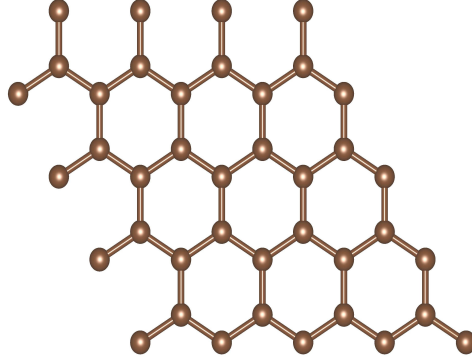


Fig. 3.1: Optimised geometrical structure of graphene. Brown balls represent C atoms.

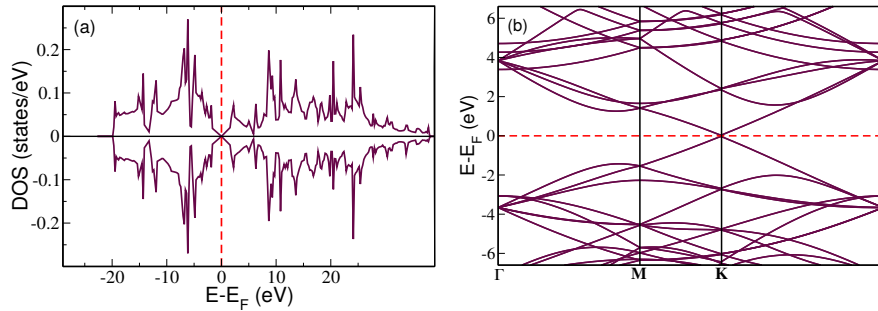


Fig. 3.2: (a) Density of states and (b) band structure of graphene.

## 3.3 Results and Discussions

### 3.3.1 Graphene

Graphene is a 2-dimensional allotrope of carbon. This monolayer material is a basic building block of graphite. Graphene, however, has several features that make it different from graphite. In this one atom thick material, carbon atoms are arranged in a hexagonal honeycomb lattice as shown in Fig. 3.1. Lattice parameters of graphene are  $a = b = 2.44 \text{ \AA}$ ,  $\alpha = \beta = 90^\circ$ ,  $\gamma = 120^\circ$ . Each carbon in the lattice forms a strong covalent bond with its neighbours with a bond length of  $1.42 \text{ \AA}$ .



The electronic structure of graphene shows valence band and conduction band of graphene meets at a single point at the wave vector 'K'(Fig. 3.2). Thus, this zero bandgap material obtains a semi-metallic behaviour. The energy-momentum dispersion relation becomes linear at this point, and it can be expressed using the relation  $E = \hbar k|_{v_F}$  where  $v_F$  is the Fermi velocity, and  $\hbar k$  is the momentum. We know that the linear dispersion of band refers to a different electronic behaviour compared to the conventional parabolic energy dispersion (Andrei et al., 2012). Here the electron behaves more like a massless photon. The effective mass is the parameter that describes how an electron at a particular wave vector responds to the applied force. Even though the electron has a definite mass, the effective mass of the electron can be zero. The vanishing of the effective mass of graphene indicates the velocity of an electron confined on graphene remains constant.

### 3.3.2 Transition Metal Dichalcogenides

Even though there are many interesting properties of graphene, certain drawbacks of graphene have led to the search for other 2D materials having more suitable properties. Although it may not be present in nature as 2D material, some materials have the potential to be transformed into 2D material. Transition Metal Dichalcogenides (TMDC) is a set of materials with such capability. This group of materials shares the similar chemical formula  $MX_2$ , where M is a transition metal (Mo, W, etc.) and X is a chalcogen atom (S, Se, etc). From the structural point of view, TMDC materials are similar to graphene, with a thickness of 0.6 nm to 0.7 nm. Adjacent layers in the TMDC materials are attached via van der Waals forces. So, these materials can be easily shaped into monolayers (Novoselov et al., 2005b). Since TMDC materials containing transition metal atoms that are heavy, with valence d orbitals, these materials have a strong spin-orbit interaction. TMDC materials exhibit many properties which are favorable for applications in various fields, especially in spintronics (Manzeli et al., 2017).

#### Molybdenum Disulfide ( $MoS_2$ )

$MoS_2$  is a prominent material among TMDCs. It occurs naturally as the mineral 'molybdenite'. This sandwiched structure consists of Mo(+4) and S(-2), and they form a covalent bond in the sequence of S-Mo-S. Sandwiched layers interact through relatively weak van der Waals forces. The weak interlayer interaction allows these layers to slide over one another. So, it is easy to prepare  $MoS_2$  in monolayer and few-layer form.

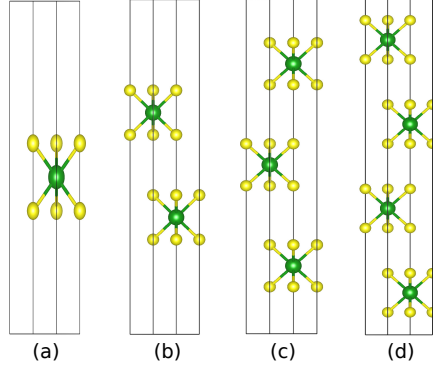


Fig. 3.3: Unit cells of (a) monolayer MoS<sub>2</sub>, (b) bilayer MoS<sub>2</sub>, (c) trilayer MoS<sub>2</sub>, and (d) bulk MoS<sub>2</sub>. Here molybdenum atoms and sulfur atoms are represented by green and yellow color balls respectively.

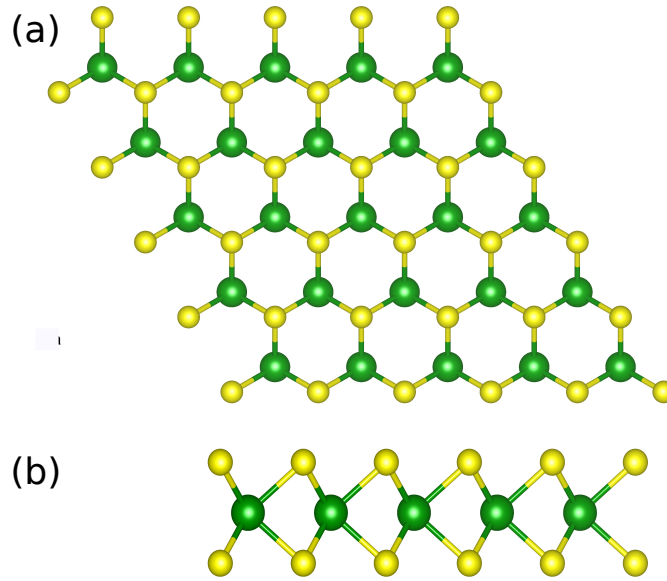


Fig. 3.4: (a) Top view and (b) side view of the crystal structure of monolayer MoS<sub>2</sub> showing a layer of molybdenum atoms (green) sandwiched between two layers of sulfur atoms (yellow).

To study the properties of layered MoS<sub>2</sub>, the bulk lattice parameters are optimized initially. The layer structures were extracted from the bulk structure considering the optimized in-plane lattice parameters and inserting empty space along the out-of-plane direction. Sufficient empty space ( $\approx 10$  Å) has been considered in the unit cell along the out-of-plane direction to avoid the interaction between the periodic images. Optimised geometries show that these hexagonal structures are having lattice parameter  $a = b = 3.18$  Å,  $c = 13.37$  Å,  $\alpha = \beta = 90^\circ$ ,  $\gamma = 120^\circ$ . The S-Mo bond length is obtained as 2.42 Å. Then the electronic structure of these materials is investigated carefully. The study shows that they are semiconductors. Interestingly the bandgap of this semiconductor material varies with the number of layers. The bandgap of bulk MoS<sub>2</sub> is obtained as 1.2 eV and

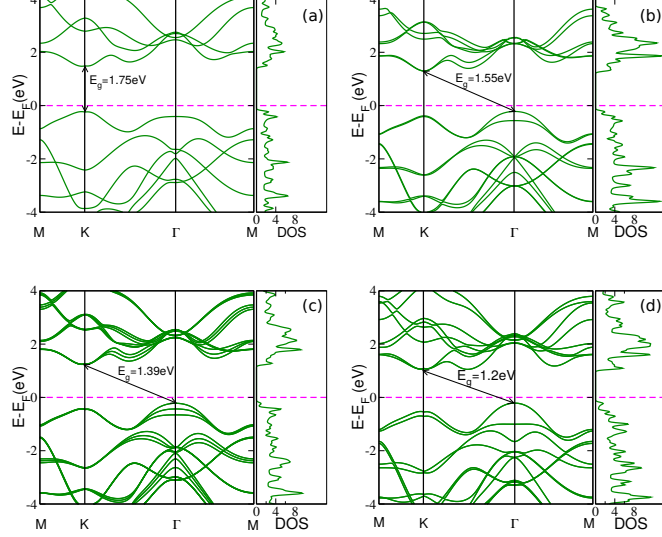


Fig. 3.5: The band structures and the density of states of (a) monolayer MoS<sub>2</sub>, (b) bilayer MoS<sub>2</sub>, (c) trilayer MoS<sub>2</sub>, and (d) bulk MoS<sub>2</sub>. The magenta dotted line represents the Fermi level.

that of trilayer and bilayer are 1.39 eV and 1.55 eV, respectively. All these multilayer MoS<sub>2</sub> forms have an indirect bandgap. But monolayer MoS<sub>2</sub> exhibits a direct bandgap of 1.75 eV (Fig. 3.5). The obtained bandgap values come to agree with experimental values (Mak et al., 2010; Hu et al., 2019). The experimental bandgaps for bulk, trilayer, bilayer, and monolayer MoS<sub>2</sub>s are 1.29 eV, 1.46 eV, 1.6 eV and 1.8 eV respectively. It can be seen that the bandgap increases as the number of layers decreases, which is due to the quantum confinement effect.

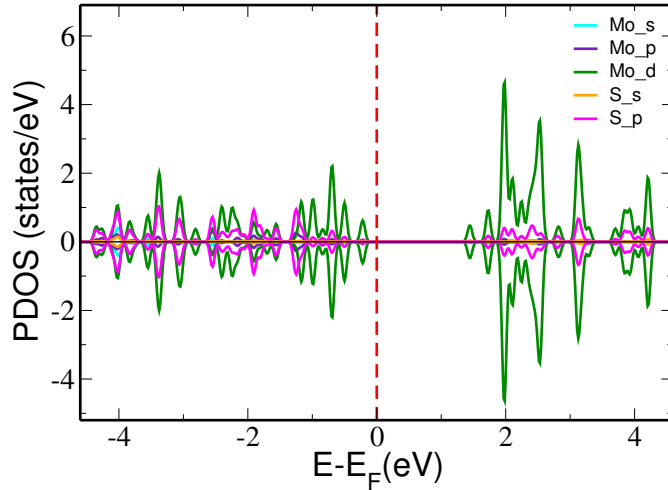


Fig. 3.6: The partial density of states of different orbitals of Mo and S in the monolayer MoS<sub>2</sub>.

The Mo-*d* and S-*p* orbitals play a pivotal role in the material's electronic properties (Fig. 3.6). In the MoS<sub>2</sub>, indirect bandgap depends on the overlap of *d* orbital of Mo and *p<sub>z</sub>* orbital of S. It strongly depends on the interlayer cou-

pling. Thus, as the number of layers decreases, the intrinsic direct bandgap of the material becomes more pronounced. The interlayer interaction is absent in the monolayer MoS<sub>2</sub>, which shows a direct bandgap. MoS<sub>2</sub> does not exhibit any spin polarization in the spin resolved electronic structure calculation (Fig. 3.6). This shows MoS<sub>2</sub> is a perfect non-magnetic material.

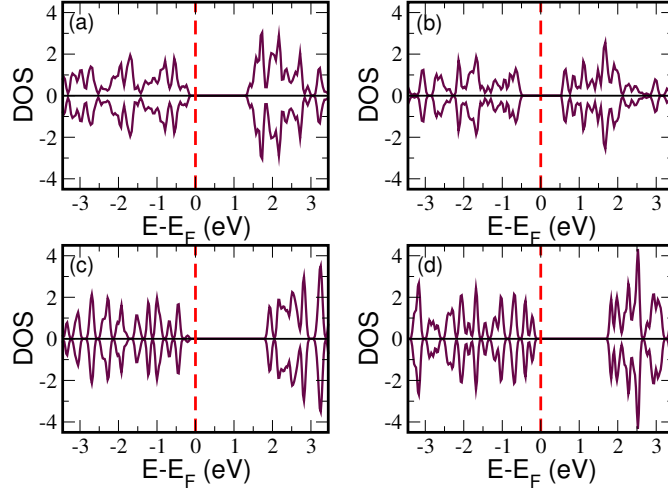


Fig. 3.7: Density of states of (a) monolayer MoSe<sub>2</sub>, (b) monolayer MoTe<sub>2</sub>, (c) monolayer WS<sub>2</sub>, and (d) monolayer WSe<sub>2</sub>.

### Other TMDC Materials

The other major TMDC materials are MoSe<sub>2</sub>, MoTe<sub>2</sub>, WS<sub>2</sub> and WSe<sub>2</sub>. Monolayers of these materials are geometrically optimized. All these structures are hexagonal with  $\alpha = \beta = 90^\circ$  and  $\gamma = 120^\circ$ . The lattice parameter of MoSe<sub>2</sub>, MoTe<sub>2</sub>, WS<sub>2</sub> and WSe<sub>2</sub> are 3.327 Å, 3.518 Å, 3.191 Å, and 3.327 Å respectively. The density of states of these materials are calculated and are shown in Fig. 3.7. Monolayer MoSe<sub>2</sub> is having a bandgap of 1.50 eV, whereas that of monolayer MoTe<sub>2</sub>, WS<sub>2</sub> and WSe<sub>2</sub> are 1.03 eV, 1.93 eV and 1.65 eV respectively. The bandgap of TMDC monolayer materials ranges from near-infrared to visible range. Similar to MoS<sub>2</sub> other TMDC materials are also not showing spin-polarized nature and all of these materials are exhibiting non-magnetic nature.

### 3.3.3 Co/monolayer TMDC Interfaces

Efficient spin injection in the semiconducting transport layer from ferromagnetic lead is a major challenge in advanced spintronics. Detailed understanding of the magnetic metal-semiconductor interfaces is essential. On the other hand, proper-

ties of semiconducting materials can be altered when it comes into contact with other materials. Therefore, interfaces are constructed considering different TMDC materials and magnetic cobalt surfaces to understand the interface properties and to check the tuning possibility in TMDC materials.

### Co/MoS<sub>2</sub> Interface

The Co/MoS<sub>2</sub> interface is constructed by superimposing  $5 \times 5$  Co cells along the Z direction and  $4 \times 4$  monolayer MoS<sub>2</sub> cells to have a minimal in-plane lattice mismatch of 4%. The optimized Co/MoS<sub>2</sub> interface structure is shown in Fig. 3.8. The average inter-layer distance between MoS<sub>2</sub> and Co is 2.30 Å which is close to the Co-S bond length measured in bulk cobalt sulphides (2.32 Å for CoS<sub>2</sub> with the pyrite structure (Nowack et al., 1991)). Note that S atoms at the interface are covalently bonded to the Co atoms, which indicates higher stability of the MoS<sub>2</sub> on top of the Co surface.

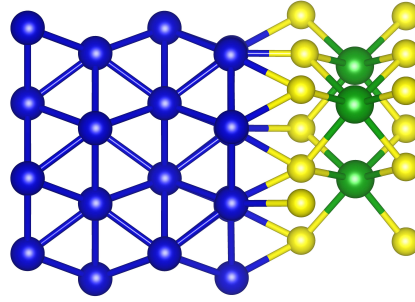


Fig. 3.8: Optimised geometrical structure of Co/MoS<sub>2</sub>. Blue, green, and yellow balls represent Co, Mo, and S atoms respectively.

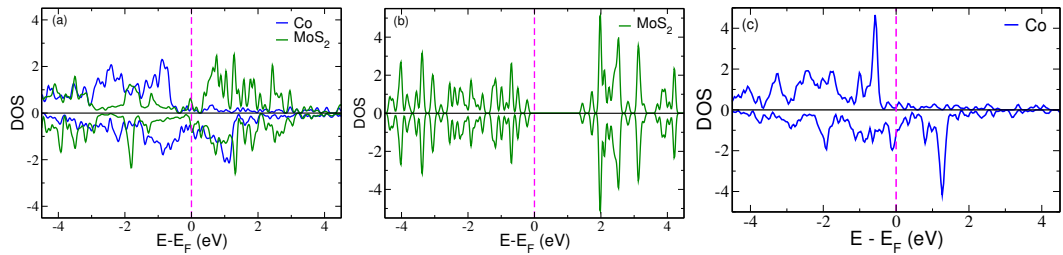


Fig. 3.9: The density of states for (a) Co and MoS<sub>2</sub> in Co/MoS<sub>2</sub> interface. (b) The density of states of isolated monolayer MoS<sub>2</sub>. (c) Density of states of Co in the isolated structure.

The electronic structure properties of the Co/MoS<sub>2</sub> interface are investigated in detail. It is evident from the results that the DOS of heterostructure is not a simple aggregation of the individual density of states of Co and MoS<sub>2</sub> (Fig. 3.9). New hybridized states are formed in the heterostructure. To understand

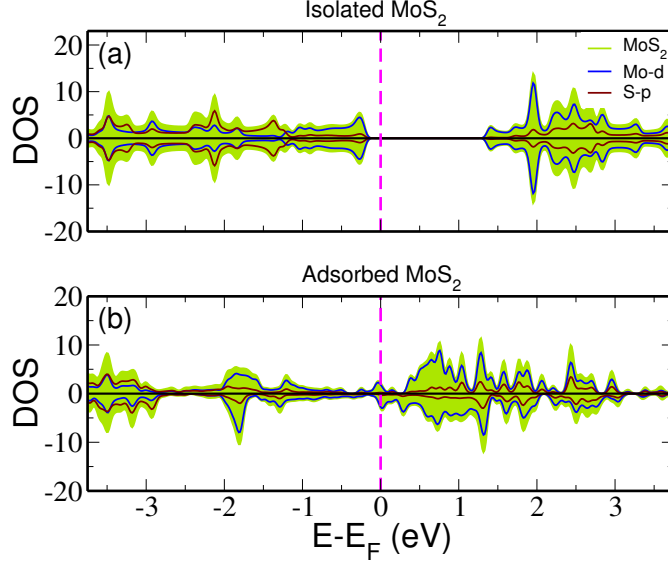


Fig. 3.10: Density of states of monolayer MoS<sub>2</sub> in the isolated structure and Co/MoS<sub>2</sub> heterostructure.

the microscopic changes that occurred in the electronic structure of MoS<sub>2</sub> when it comes in contact with Co, the DOS of adsorbed MoS<sub>2</sub> is compared to that of isolated MoS<sub>2</sub> (Fig. 3.10). Monolayer MoS<sub>2</sub> exhibits semiconducting nature with a bandgap of 1.75 eV. The strong interaction between Co and MoS<sub>2</sub> induces bandgap states in the adsorbed MoS<sub>2</sub>. The orbital-projected DOS was also calculated as it would give more clarity to understand the changes at the interface. While analyzing the orbital-wise contribution to the DOS of MoS<sub>2</sub>, it can be seen that the main contribution to the DOS of MoS<sub>2</sub> comes from Mo-d orbital and S-p orbital. In Fig. 3.10, Mo-d orbital and S-p orbital contributions are marked in blue and brown colors respectively. It is observed that PDOS of S-p orbital is similar to that of Mo-d orbitals in isolated MoS<sub>2</sub>. The same trend is observable in the adsorbed MoS<sub>2</sub> too, except at the bandgap state. Mo-d orbital contribution determines the bandgap state in adsorbed MoS<sub>2</sub>. DOS of spin-up (positive value) and spin-down (negative value) states are same in isolated MoS<sub>2</sub>. But a dissimilarity in DOS can be seen in adsorbed MoS<sub>2</sub> in the spin-up and spin-down state. The proximity of ferromagnetic material Co is the reason behind the spin polarization observed here.

The spin polarization is defined as the difference between the densities of states of spin-up and spin-down states divided by their sum. The spin polarization ( $P_s$ ) is estimated for the adsorbed MoS<sub>2</sub> using the relation,

$$P_s = \frac{DOS_{\uparrow} - DOS_{\downarrow}}{DOS_{\uparrow} + DOS_{\downarrow}} \quad (3.1)$$

The absolute value of the spin polarization thus obtained is shown in Fig. 3.11.

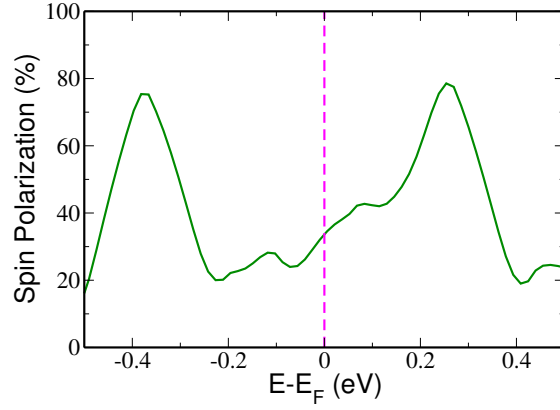


Fig. 3.11: Spin polarization in the MoS<sub>2</sub> layer. The Fermi energy is set to zero.

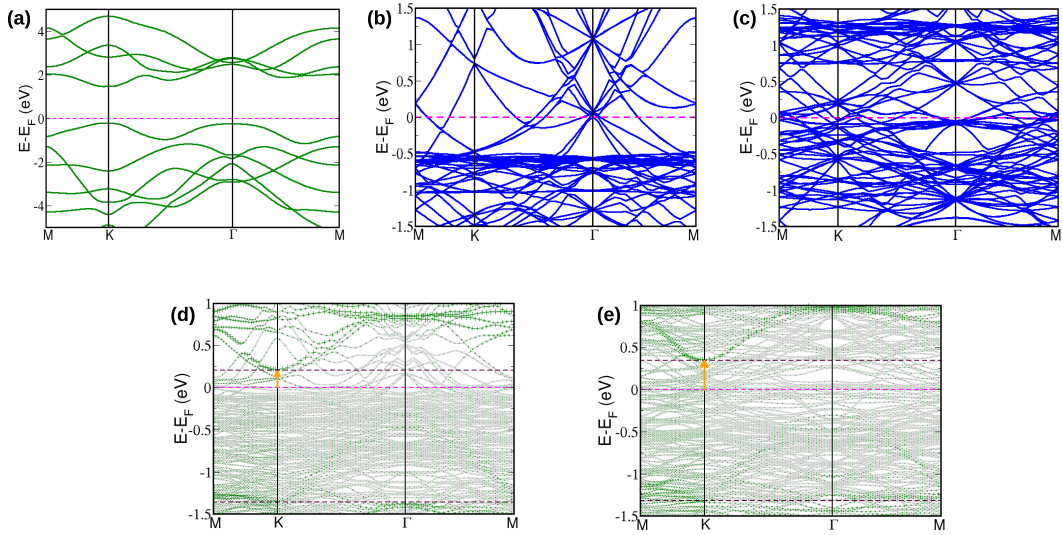


Fig. 3.12: (a) Band structure of isolated monolayer MoS<sub>2</sub>. (b) and (c) represent spin-up and spin-down energy band structure of Co. Spin-up and spin-down energy band structures of Co/MoS<sub>2</sub> are shown in (d) and (e). Total band structures is represented by grey lines, and the contributions of MoS<sub>2</sub> orbitals is represented in green color. CBO and VBO are marked in maroon dashed lines. Orange arrow marked in (d) and (e) represent the Schottky barrier height.

At Fermi level, MoS<sub>2</sub> is showing 34% spin polarization. This clearly shows that Co-electrode can be used to inject spin polarized current to MoS<sub>2</sub>.

The calculation shows that in the isolated MoS<sub>2</sub>, the valence band offset (VBO) is closer to the Fermi energy, manifesting a p-type semiconductor (Fig. 3.12 (a)). Whereas in the case of adsorbed MoS<sub>2</sub> on Co-layer, the conduction band offset (CBO) is nearer to the Fermi level. It represents the n-type contact. The shift of CBO of MoS<sub>2</sub> towards the Fermi level also indicates a reduction in the

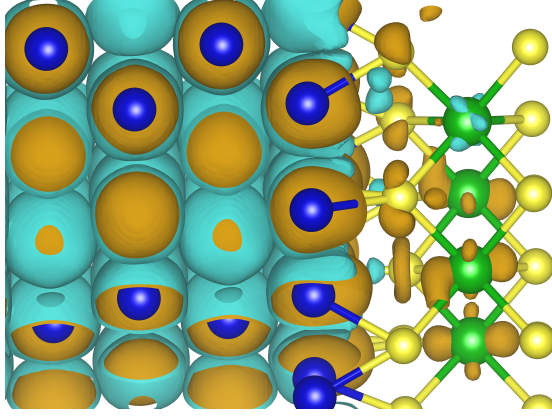


Fig. 3.13: Magnetization density plot for Co/MoS<sub>2</sub> heterostructure. The orange and cyan surfaces indicate the positive and negative magnetization densities respectively.

Schottky barrier height. To determine the Schottky barrier, an accurate energy band structure of Co/MoS<sub>2</sub> is calculated. Fig. 3.12 (d) and (e) represent spin-up and spin-down state band structure of Co/MoS<sub>2</sub>. Total band structures are represented by grey curves, and the contributions of MoS<sub>2</sub> orbitals are represented in green color. Comparing projected bands of MoS<sub>2</sub> in Co/MoS<sub>2</sub> structure and isolated monolayer MoS<sub>2</sub> bands (Fig. 3.12 (a)), it is evident that new bands are formed in the heterostructure. To identify the exact locations of CBO and VBO of adsorbed MoS<sub>2</sub>, the band structure of isolated monolayer MoS<sub>2</sub> and Co/MoS<sub>2</sub> are analysed in detail. The CBO appears at 0.20 eV in the spin-up band structure and 0.35 eV in the spin-down band structure. Corresponding VBO are at -1.37 eV and -1.31 eV respectively. Spin splitting occurs here due to the ferromagnetic properties of Co.

CBO is closer to the Fermi level than VBO, which implies n-type contact. The n-type Schottky barrier height for adsorbed MoS<sub>2</sub> is found as 0.20 eV for spin-up electrons and 0.35 eV for spin-down electrons. Interaction with Co induces spin densities on MoS<sub>2</sub> as shown in magnetization density plot, Fig. 3.13. A decrease is observed in the spin magnetic moment of Co atoms at the interface. The average spin magnetic moment of outermost layer Co atoms is 1.75  $\mu_B$ . But it decreases to 1.58  $\mu_B$  when it comes to the Co layer bounded to MoS<sub>2</sub>. Each Mo and S atoms of MoS<sub>2</sub> layer in the heterostructure are carrying small spin moments of 0.015  $\mu_B$  and 0.034  $\mu_B$ , respectively, which are ferromagnetically coupled with the Co magnetic moments.

The spin-polarized charge transfer at the Co/MoS<sub>2</sub> interface are also subjected to study. For that purpose, the spin-up (spin-down) electron density of Co/MoS<sub>2</sub>  $n_{\uparrow(\downarrow)Co/MoS_2}$  are calculated in the first step. The next step was the calculation of the spin-up (spin-down) electron density of Co ( $n_{\uparrow(\downarrow)Co}$ ) by keeping Co and



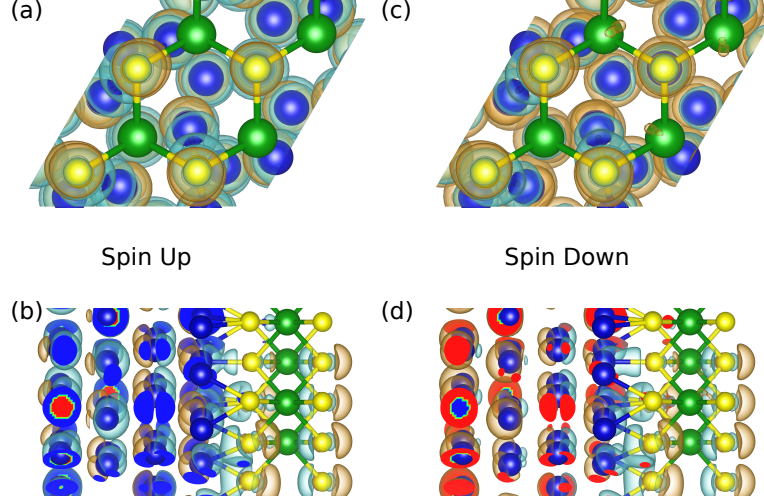


Fig. 3.14: (a) Top view and (b) side view of the spin-up charge transfer  $\Delta n_{\uparrow}(\mathbf{r})$  at the interfaces of the slab. (c) Top view and (d) side view of the spin-down charge transfer  $\Delta n_{\downarrow}(\mathbf{r})$  at the interface. Positive and negative values are respectively shown with cyan and orange colors. Blue, green, and yellow spheres (when visible) display the position of Co, Mo, and S atoms, respectively.

removing Mo and S atoms from the supercell. In the same manner, electron density of MoSe<sub>2</sub> ( $n_{\uparrow(\downarrow)MoSe_2}$ ) is also calculated. Then the spin-up (spin-down) space-dependent charge transfer is calculated using the relation,

$$\Delta n_{\uparrow(\downarrow)}(\mathbf{r}) = n_{\uparrow(\downarrow)Co/MoSe_2}(\mathbf{r}) - (n_{\uparrow(\downarrow)Co}(\mathbf{r}) + n_{\uparrow(\downarrow)MoSe_2}(\mathbf{r})) \quad (3.2)$$

Top and side views of the calculated spin-up resultant transferred spin-densities have been calculated and shown in Fig. 3.14. Note that the charge transfer occurs between interface Co and S atoms along the Co-S covalent bond. Also, a significant difference is observed in the distribution of transferred charges for two different spin-channels which is expected to take a lead role during the spin-injection process.

### Co/MoSe<sub>2</sub> Interface

Similar to MoS<sub>2</sub>, another interface between monolayer TMDC material- MoSe<sub>2</sub> and Co has been constructed by superimposing 4 × 4 monolayer MoSe<sub>2</sub> on 5 × 5 Co(10 $\bar{1}$ 0)(Fig. 3.15). The geometry optimized structure shows that covalent bonds are formed between atoms of interface Co and MoSe<sub>2</sub>. This implies to strong interaction at the interface. The equilibrium vertical distance ( $d_{eq}$ ) of Co-MoSe<sub>2</sub> is found to be 2.39 Å.

The large exchange interaction present in the ferromagnetic Co may alter the

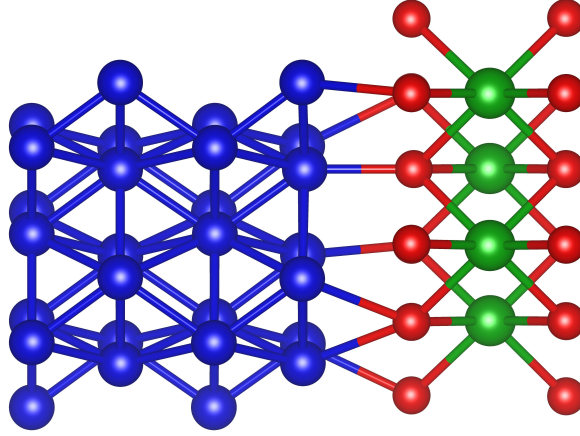


Fig. 3.15: Optimised geometrical structure of Co/MoSe<sub>2</sub>. Blue, green, and red balls represent Co, Mo, and Se atoms respectively.

electronic and magnetic structure of MoSe<sub>2</sub>. Similar to the MoS<sub>2</sub>, calculations reveal that while making an interface with Co, MoSe<sub>2</sub> also shows magnetic and conducting behaviour (Fig. 3.16). New spin-polarized hybridized states appear in the gap regions (bandgap state) in adsorbed MoSe<sub>2</sub>/Co system, mainly from Mo atoms of d-orbital character. Spin polarization on MoSe<sub>2</sub> is obtained as 26%, clearly indicates that efficient spin-injection is possible in MoSe<sub>2</sub> using a Co-lead.

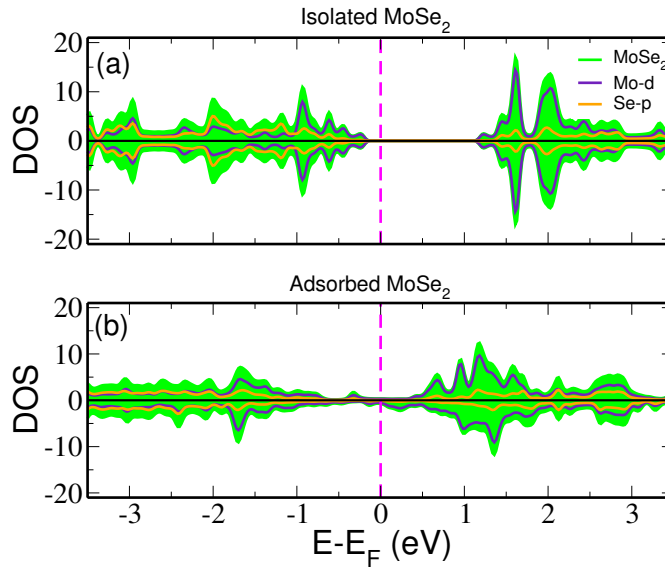


Fig. 3.16: Density of states of monolayer MoSe<sub>2</sub> in the isolated structure and Co/MoSe<sub>2</sub> heterostructure.

Next, the interface magnetic properties of the Co/MoSe<sub>2</sub> interface have been carefully studied. Mo atoms carry a spin magnetic moment of 0.019  $\mu_B$ . Se atoms that are bonded to Co atoms having a spin magnetic moment in the range 0.014  $\mu_B$  to 0.017  $\mu_B$  and Se atoms that are not directly bound to Co atoms also possess a very small magnetic moment in the range 0.002  $\mu_B$  to 0.010  $\mu_B$ . A decrease

in the spin magnetic moment of Co atoms was observed at the interface. The average spin magnetic moment of the outermost layer of Co atoms is  $1.75 \mu_B$ . Nevertheless, it decreases to  $1.66 \mu_B$  when the Co layer is bonded to  $\text{MoSe}_2$ .

### 3.4 Conclusion

The electronic structure of various 2D materials is studied using first-principle density functional calculations. Particular attention was given to the TMDC layered materials. The thickness-dependent bandgap of TMDC materials is illustrated by using monolayer, bilayer, trilayer, and bulk  $\text{MoS}_2$ . Due to the quantum confinement, the bandgap increases with a decrease in the number of layers. Unlike multilayer  $\text{MoS}_2$  materials, monolayer  $\text{MoS}_2$  exhibits a direct bandgap.

The interface structures are modelled by using a highly spin-polarized ferromagnetic metal, Co, and TMDC materials. The electronic structure and magnetic properties are calculated and investigated the potential of spin injection at the interface.

The study shows a significant change in the electronic structure and magnetic properties of monolayer TMDC materials when they form an interface with Co. Monolayer TMDC materials become conducting, magnetic, and spin-polarized in the proximity of Co. The spin injection efficiency calculated for the Co-TMDC interfaces shows that Co has the potential to inject spin-polarized current to TMDC materials.

# Chapter 4

## Spin Transport Through Magnetic Junctions Composed of Transition Metal Dichalcogenides

### 4.1 Introduction

The fascinating properties of 2D TMDC materials make them a desirable material for research in multiple areas, including spintronics. Several experimental and theoretical investigations have been carried out in the magnetic tunnelling junctions (MTJs) formed with layered TMDC materials. Wang et al. introduced a monolayer MoS<sub>2</sub> based spin valve in 2015 considering NiFe permalloy as electrode material (Wang et al., 2015). Their temperature-dependent magneto-resistance (MR) measurement reports a maximum of 0.73% MR in the system. Even if it was not a good MR for device applications, this remarkable work showed that TMDC materials could be used as spacer material in magnetic junctions with suitable modifications. Efforts have been made to prepare MoS<sub>2</sub> based MTJ. High MR has been predicted theoretically in multiple layers of MoS<sub>2</sub> sandwich between Fe electrodes (Dolui et al., 2014). A similar study has recently been done considering planar MoS<sub>2</sub> nano-ribbon structure (Tarawneh et al., 2016).

Various research findings reported in the past few years show the potential of using TMDC materials for spin transport applications. The electronic structure study discussed in the previous chapter also supports this. The study of transport properties in the magnetic junctions made of TMDC layers and different magnetic metal electrodes may pave the way to design spintronic devices with better properties. In particular, the ferromagnetic compounds with high exchange splitting,

such as Co, will be an appropriate choice as the electrode material, which may support an efficient spin injection process and, in turn, significantly improve the performance of the device. This chapter explores spin-polarized transport through the magnetic junction composed of TMDC barriers between two Co electrodes.

## 4.2 Methodology

The structures used for the transport study are optimized using SIESTA (Soler et al., 2002). Self-consistent calculations are performed considering a 300 Ry mesh cut-off. A linear combination of numerical atomic orbitals with double zeta polarizations (DZP) basis set is used. The conjugate gradient method is used to relax the ionic coordinates until the force on each atom is reduced to less than 0.01 eV/Å. The transport properties of the magnetic junctions are investigated with the fully self-consistent NEGF method implemented in TransSIESTA. Calculations are carried out at 300 K temperature. The transmission function  $T(E)$ , which describes the probability for an electron with incident energy  $E$  under bias voltage  $V_b$  to transfer from the left semi-infinite electrode to the right semi-infinite electrode is calculated. The spin-dependent transmission coefficient is calculated using the mathematical relation (Yang et al., 2011),

$$T_\sigma(E) = Tr[\Gamma_R^\sigma(E)G_R^\sigma(E)\Gamma_L^\sigma(E)G_R^{\sigma\dagger}(E)] \quad (4.1)$$

Here  $\sigma$  represent the spin-index,  $\Gamma_{L,R}^\sigma(E) = (\Sigma_{L,R}^\sigma(E) - \Sigma_{L,R}^{\sigma\dagger}(E))$  describes the level broadening due to the coupling between left(L)(right(R)) electrode and the central scattering region.  $\Sigma_{L,R}^\sigma(E)$  corresponds to the retarded self-energy associated with this coupling.  $G_R^\sigma = (ES - H^\sigma - \Sigma_L^\sigma - \Sigma_R^\sigma)^{-1}$  represents the retarded Green's function. The Hamiltonian and the overlap matrix are represented by  $H$  and  $S$  respectively.

The spin-polarized current,  $I_{\uparrow(\downarrow)}$  through the device was calculated by using Landauer-Büttiker formula.

$$I_{\uparrow(\downarrow)} = \frac{e}{h} \int_{-\infty}^{\infty} T_{\uparrow(\downarrow)}(E, V_b) [F(E - \mu_L) - F(E - \mu_R)] dE \quad (4.2)$$

Where  $F(E)$  is the Fermi Dirac distribution for an energy level  $E$  under the bias voltage  $V_b$ . The bias window is kept from  $-V_b/2$  to  $V_b/2$ . Magnetoresistance of different magnetic junctions is also estimated. The magnetoresistance of a magnetic junction is defined as the conductance difference between parallel ( $G_{PC}$ ) and

anti-parallel ( $G_{APC}$ ) orientations of electrodes and normalized by the conductance in anti-parallel configuration (Tsymbal et al., 2003).

$$MR = \frac{G_{PC} - G_{APC}}{G_{APC}} \quad (4.3)$$

This can also be expressed in terms of current (Chen et al., 2016) as

$$MR = \frac{I_{PC} - I_{APC}}{I_{APC}} \quad (4.4)$$

Here  $I_{PC}$  and  $I_{APC}$  correspond to the total current through the junction in parallel and anti-parallel magnetic configuration of the electrodes. In this work, the MR value is estimated directly from the output current.

The spin injection efficiency (SIE) is also estimated at different bias voltages using the output current. Formula used to calculate SIE is (Xu et al., 2012)

$$SIE = \frac{I_{\uparrow} - I_{\downarrow}}{I_{\uparrow} + I_{\downarrow}} \quad (4.5)$$

where  $I_{\uparrow}$  and  $I_{\downarrow}$  denoted spin-up and spin-down current respectively.

## 4.3 Results and Discussions

### 4.3.1 MoS<sub>2</sub> Based Magnetic Junctions

#### Co/monolayer MoS<sub>2</sub>/Co Magnetic Junction

The transport studies are started from a magnetic junction composed of Co and monolayer MoS<sub>2</sub>. We modelled the two probe device as shown in Fig. 4.1. It has 3 regions- left electrode, device region, and right electrode. Four Co(10 $\bar{1}$ 0) layers are considered in each electrode region of this two-probe structure. The device region consists of monolayer MoS<sub>2</sub> along with two layers of Co atoms of buffer layers on each side to reduce the scattering at the lead-barrier interface. The system is periodically extended along the transverse (X, Y) directions. The spacer lies in the XY plane and transport calculation has been done along the Z direction.

Device performance can be characterized largely by the transport at equilibrium conditions. Therefore, the equilibrium transmission behaviour is investigated

first. The equilibrium transmission spectrum for Co/monolayer MoS<sub>2</sub>/Co magnetic junction is shown in Fig. 4.2. The spin-dependent transmission spectrum at

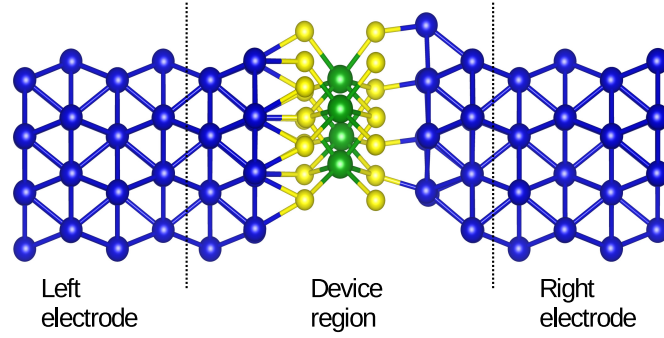


Fig. 4.1: Schematic view of Co/monolayer MoS<sub>2</sub>/Co device model. Blue, green, and yellow solid spheres represent Co, Mo, and S atoms respectively. The device region is shown within the two dashed lines and the remaining parts are the semi-infinite left and right electrodes.

equilibrium indicates that the transmission is highly spin sensitive. The Co/MoS<sub>2</sub> interface study described in the previous chapter can shed light on the reason for spin-dependent transport obtained here. The accumulation of a spin-polarized density of states at the Co/MoS<sub>2</sub> interface along with a large exchange splitting in Co electrodes, effectively works as a spin filter and supports high spin injection into the system. Note that the transmission through the up spin channel is much greater than that of the down spin channel at the Fermi energy, which confirms that the Co electrode is an efficient majority spin injector for the spacer.

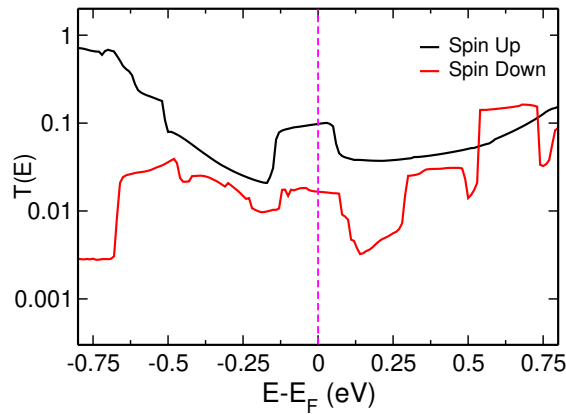


Fig. 4.2: Spin-polarized transmission spectrum at the equilibrium condition for Co/monolayer MoS<sub>2</sub>/Co magnetic junction. Black and red curves represent current through spin-up and spin-down channels respectively.

Even though spin injection to MoS<sub>2</sub> from Co and spin-polarized transport through Co/monolayer MoS<sub>2</sub>/Co at equilibrium condition are established, two more possibilities are needed to be explored before use this magnetic junction as an effective spin transport device at the application level. First, spin-polarized

transmission through the junction needs to be investigated in the presence of applied bias. On the other hand, the magnetic orientation of the Co-lead in the device can also be altered by applying an external magnetic field. So, Co/monolayer MoS<sub>2</sub>/Co magnetic junction can be in the parallel magnetic configuration as well as the anti-parallel magnetic configuration. A significant difference in transmission through the junction when the configuration of electrodes changes leads to a high magnetoresistance in the system, which has widespread industrial applications. So, the transmission function is calculated for this two-probe model under the influence of applied bias and subsequently estimated the current through the junction considering parallel and anti-parallel magnetic orientations of Co-electrodes. The applied bias is systematically increased from 0.2 V to 1 V. The transmission spectrum in the presence of external bias in the parallel and anti-parallel magnetic configurations of electrodes are shown in Fig. 4.3(a). An asymmetry is observed in the transmission through the two different spin channels at all voltages when the magnetic orientations of electrodes are parallel. A noticeable change in transmission spectrum was observed when the magnetic field orientations of electrodes were altered from parallel to anti-parallel configurations.

Current through the magnetic junction is related to the transmission through the junction. Spin-polarized current is calculated using the equation 4.2. Spin-polarized current thus obtained for Co/monolayer MoS<sub>2</sub>/Co is shown in Fig. 4.3(b). In the case of the parallel configuration, the spin-up current is much greater than the spin-down current at all voltages. An abrupt increase is observed in the spin-up current through the junction at an applied bias of 0.6 V and above. This increase can be easily correlated with the obtained transmission spectrum (Fig. 4.3(a)). Note that the current is proportional to the product of transmission and the Fermi function. Since the Fermi function reduces exponentially to zero at energies away from Fermi energy, the contribution from those energy levels in the total current is negligible. Hence, the current through the transistor is determined by transmission values closer to the Fermi level. Therefore, it is clear from Fig. 4.3(a), as voltage increases, a large peak of spin-up transmission approaches the Fermi energy. Thus, a significant contribution comes from transmission through the spin-up channel in determining current. Spin-down transmission peaks are also shifted with voltage. At 0.8 V, the spin-down transmission peak reaches Fermi energy, which results in a relatively higher spin-down current at that voltage.



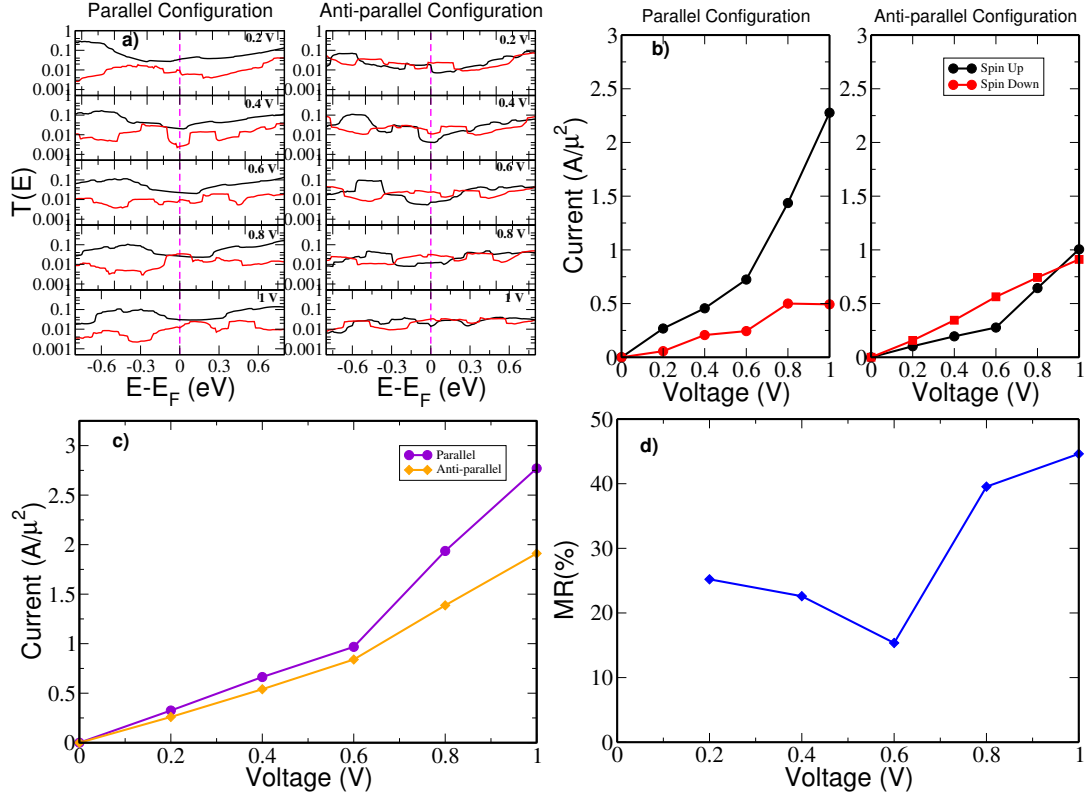


Fig. 4.3: a) Spin-polarized transmission spectrum, b) voltage-spin current characteristics, c) voltage-total current characteristics, and d) magnetoresistance of Co/monolayer MoS<sub>2</sub>/Co magnetic junction. Black and red curves represent current through spin-up and spin-down channels respectively.

It is also observed that the change in the magnetic orientation of electrodes impacted differently on the current through the spin-up and spin-down channels, which is reflected in the voltage-current characteristics (Fig. 4.3(b)). The maximum change in current occurs when the applied bias voltage is 0.8 V and above. Although the total current is always less in the anti-parallel configuration, compared to parallel configuration, the difference becomes significant at higher voltages (Fig. 4.3(c)).

Significant differences in electrons transmission and current due to the change of the relative orientations of the electrodes magnetization lead to higher magnetoresistance of the system. The magnetoresistance of Co/monolayer MoS<sub>2</sub>/Co is calculated using the equation 4.4 and is shown in Fig. 4.3(d). The abrupt increase in the total current after 0.6 V in the parallel configuration reflects as high MR at 0.8 V and 1 V. The calculation estimates MR of  $\sim 45\%$  for Co/MoS<sub>2</sub>/Co at 1 V applied voltage.

## Co/trilayer MoS<sub>2</sub>/Co Magnetic Junction

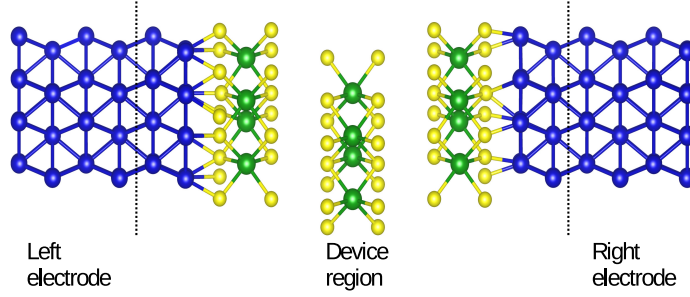


Fig. 4.4: Schematic view of Co/trilayer MoS<sub>2</sub>/Co device model. Blue, green, and yellow solid spheres represent Co, Mo, and S atoms respectively. The device region is shown within the two dashed lines and the remaining parts are the semi-infinite left and right electrodes.

Next, trilayer MoS<sub>2</sub> is considered in the device region as shown in Fig. 4.4. Equilibrium transmission is calculated for this magnetic junction as well (Fig. 4.5). Similar to the monolayer MoS<sub>2</sub> magnetic junction, trilayer MoS<sub>2</sub> magnetic junction also gives spin-polarized transmission at the equilibrium condition. The dominance of spin-up transmission at the Fermi level was also observed. In comparison to the monolayer magnetic junction, the transmission is significantly reduced in the case of a three-layer magnetic junction. This can be understood from the electronic structure of the heterojunction. In the proximity of Co, the MoS<sub>2</sub> monolayer has a finite density of state at the Fermi energy (Fig. 4.6(a)). In contrast, in the case of a three-layer system, the first and third layer has finite DOS at the Fermi level but the second layer which is in the middle shows semiconducting nature as shown in shaded orange color in Fig. 4.6(b). As a result, the net transmission reduces drastically.

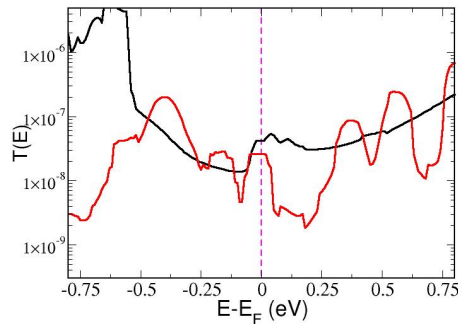


Fig. 4.5: Spin-polarized transmission spectrum at the equilibrium condition for Co/trilayer MoS<sub>2</sub>/Co magnetic junction. Black and red curves represent current through spin-up and spin-down channels respectively.

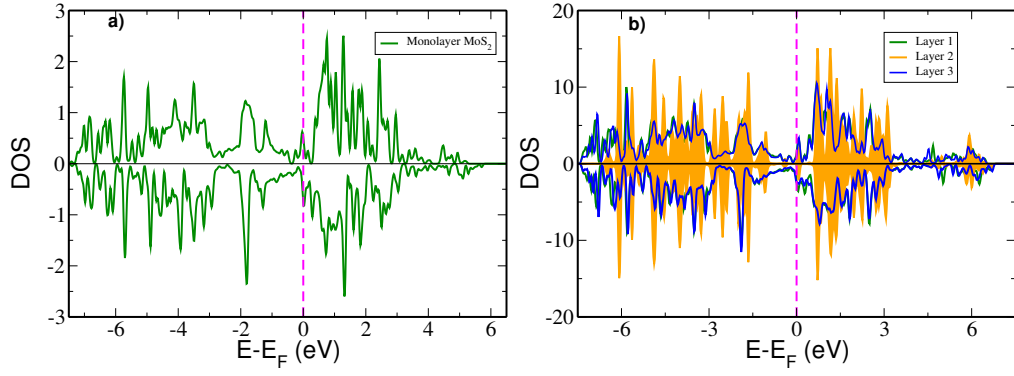


Fig. 4.6: (a) Total contribution of density of state from MoS<sub>2</sub> in the Co/MoS<sub>2</sub> heterostructure. (b) Total density of state of each MoS<sub>2</sub> layer in the Co/trilayer MoS<sub>2</sub>/Co system.

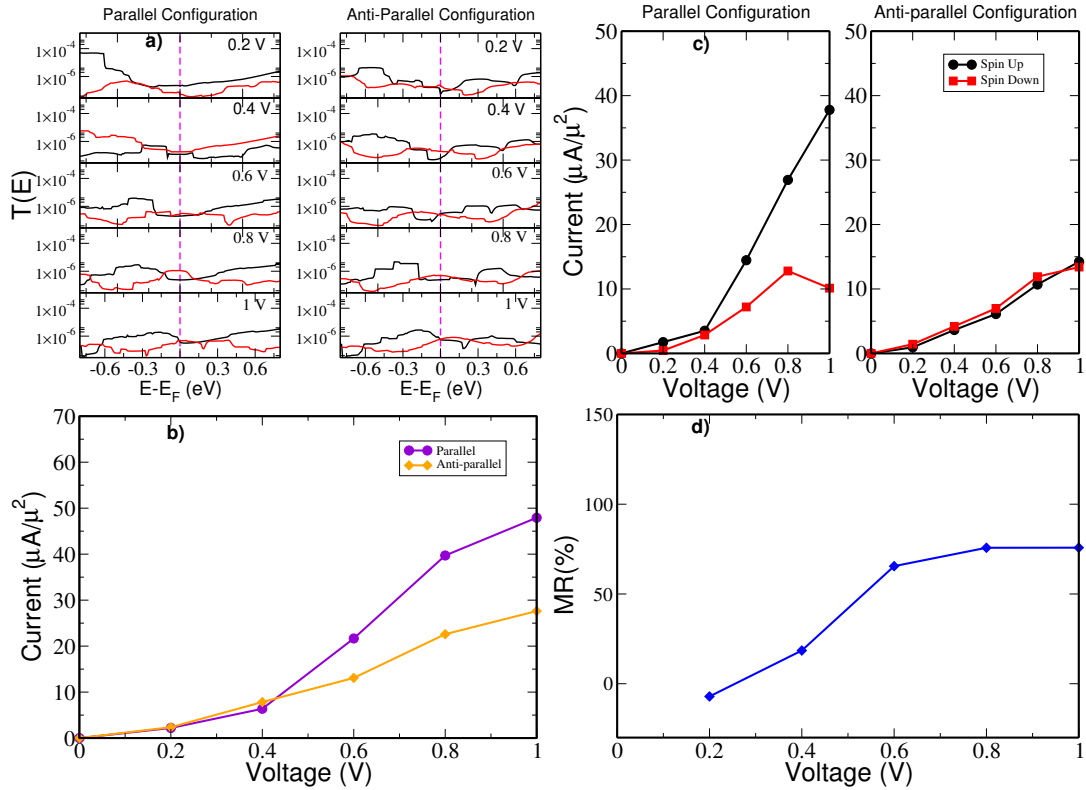


Fig. 4.7: a) Spin-polarized transmission spectrum, b) voltage-total current characteristics, c) voltage-spin current characteristics, and d) magnetoresistance of Co/trilayer MoS<sub>2</sub>/Co magnetic junction. Black and red curves represent current through spin-up and spin-down channels respectively.

The transmission function and total spin current through the junction in different applied biases are shown in Fig. 4.7(a) and Fig.4.7(b) respectively. Note that the spin current sensitivity appears only at higher applied bias voltage, i.e., 0.6 V and above. The additional MoS<sub>2</sub> layers in the spacer region have a significant influence on the total spin current passed through the junction. In addition, it

also enhances the spin-current sensitivity with respect to the relative magnetic orientation of electrodes. Spin-dependent current through the junction for two different relative orientations of electrodes magnetization is shown in Fig. 4.7(c).

It is evident from the voltage-current characteristics that the total current in the parallel configuration and anti-parallel configuration are nearly the same at lower voltages. In the parallel magnetic orientation of electrodes, more spin-up current passes through the junction when the applied bias goes up. In contrast, the spin-up current is drastically reduced in the anti-parallel configuration, and almost the same amount of spin-up and spin-down currents are passing through the junction.

The magnetoresistance values are calculated for different applied biases (shown in Fig. 4.7), which gradually increases with the increment of applied bias voltage. The maximum MR value calculated for this system is 76%. This value is greater than the maximum MR produced by monolayer MoS<sub>2</sub> magnetic junction. Therefore, an additional number of layers in the spacer region helps to improve the MR values.

### Co/MoS<sub>2</sub>/MoSe<sub>2</sub>/MoS<sub>2</sub>/Co Magnetic Junction

An attempt was then made to study how the change in structure in the spacer region is reflected in the transport properties and MR values, indicating the possibility of tunability. To start with, the middle layer MoS<sub>2</sub> at the trilayer magnetic junction was replaced by a layer of another similar transition metal dichalcogenide material MoSe<sub>2</sub> (Fig. 4.8).

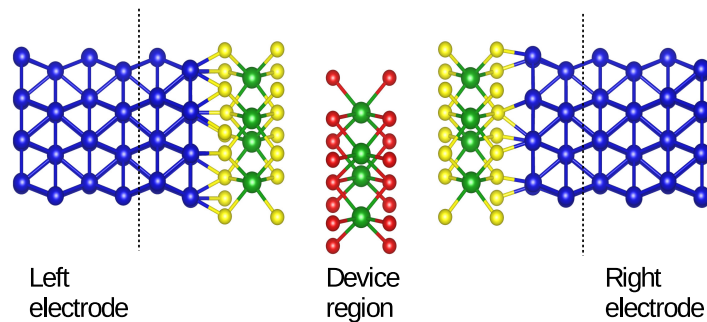


Fig. 4.8: Schematic view of Co/MoS<sub>2</sub>/MoSe<sub>2</sub>/MoS<sub>2</sub>/Co device model. Blue, green, yellow, and red solid spheres represent Co, Mo, S, and Se atoms respectively. The device region is shown within the two dashed lines and the remaining parts are the semi-infinite left and right electrodes.

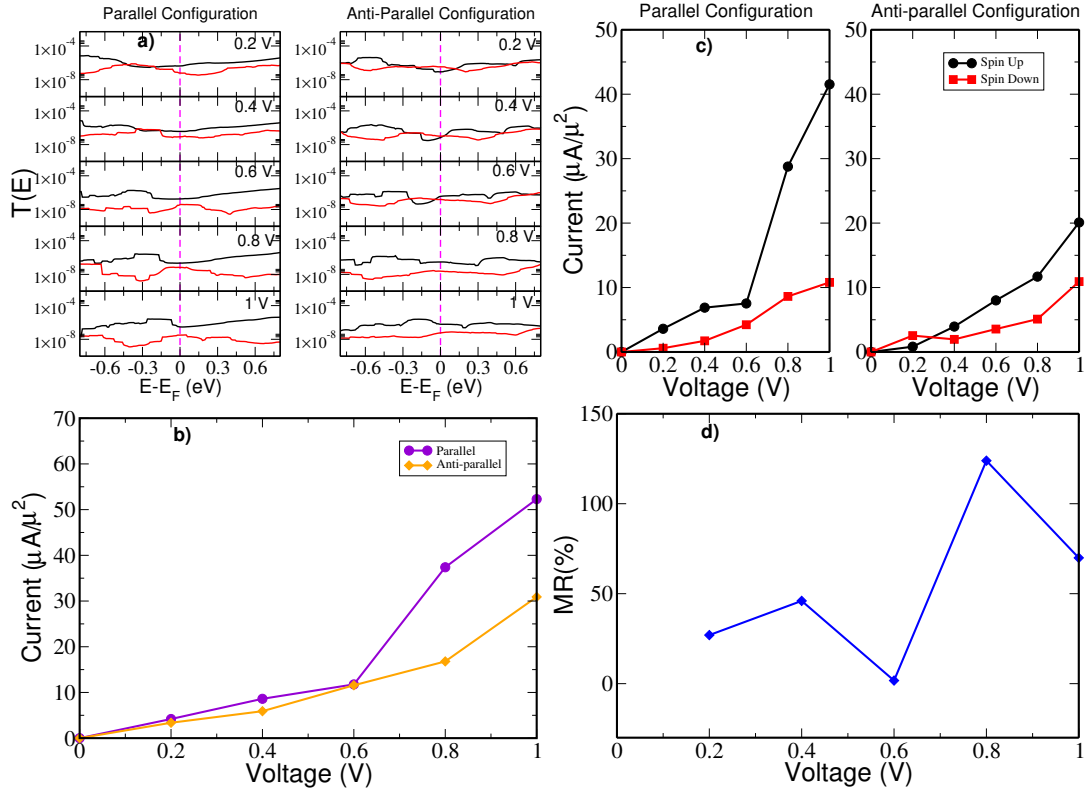


Fig. 4.9: a) Spin-polarized transmission spectrum, b) voltage-total current characteristics, c) voltage-spin current characteristics, and d) magnetoresistance of Co/MoS<sub>2</sub>/MoSe<sub>2</sub>/MoS<sub>2</sub>/Co magnetic junction. Black and red curves represent current through spin-up and spin-down channels respectively.

Transmission spectrum and voltage-current characteristics are calculated for this structure with an external bias voltage varying from 0.2 V to 1 V, in two different magnetic orientations similar to the layered MoS<sub>2</sub> systems. The transmission spectra and the total spin current in different magnetic orientations of electrodes are shown in Fig. 4.9(a) and Fig. 4.9(b) respectively. The spin-current passing through the junction, in this case, is much less compared to the Commonlayer-Co junction. The values are in the same range as those obtained in the trilayer MoS<sub>2</sub> magnetic junction. However, this change in the composite structure made it possible to change the transmission spectrum and, more precisely, the voltage-current characteristics. When the magnetic orientation of electrodes is changed from parallel to anti-parallel configuration, the spin-up current was less pronounced (Fig. 4.9(c)). However, the spin-up current in both configurations is superior to the spin-down current. Excess current can flow through the junction when the electrodes are aligned in a parallel configuration. The applied-bias dependent magnetoresistance is also calculated for this junction and is shown in Fig. 4.9d. A high MR -  $\sim 123\%$  - is exhibited at 0.8 V. This magnetic junction composed of multilayer heterostructure spacer gives better MR than monolayer and trilayer MoS<sub>2</sub> magnetic junctions. Note that the maximum value obtained in

this study is much higher than previously reported bias dependent MR values in similar studies (Dolui et al., 2014; Tarawneh et al., 2016). In the first principle study conducted at the magnetic junction using Co as the electrode and MgO as the tunnel barrier, the zero bias MR was 27.28% (Aadhityan et al., 2018). The maximum MR obtained by Chakraverty et. al in a similar magnetic junction in the presence of external bias is 91% (Chakraverty and Harisankar, 2018). Interestingly, a slight change in the composite structure gives a remarkable change in the MR. This indicates the possibility of further tuning of MR with the change in the layer structure in the spacer region.

### **Co/MoS<sub>2</sub>/graphene/MoS<sub>2</sub>/Co magnetic junction**

The study is further extended to another hybrid structure of 2D materials, which is a combination of monolayer MoS<sub>2</sub> and graphene, as a barrier (Fig. 4.10). The transmission function for this two-probe model is calculated under the influence of applied bias and subsequently estimated the current through the junction considering parallel and anti-parallel magnetic orientations of the Co electrodes. The applied bias is systematically increased from 0.2 to 1 V. The transmission spectrum in the presence of an external bias in the parallel and anti-parallel magnetic configurations of the electrodes are shown in Fig. 4.11(a) and (b), respectively. Calculations show that high asymmetry in the transmission through two different spin channels is maintained at all voltages when the magnetic orientations of the electrodes are parallel. The transmission across the spin-up channel dominates in this configuration at the Fermi level at all voltages. Interestingly, a large transmission peak that was far below the Fermi energy approaches toward the Fermi energy while increasing the applied bias voltage, and it makes a significant difference in spin-up and spin-down transmission in the proximity to the Fermi energy. On the other hand, the behaviour of the transmission function in an anti-parallel configuration is quite different from a parallel configuration at higher voltages. Transmission through the spin-down channel is dominating near the Fermi energy at a lower bias. However, this spin-down transmission becomes comparable in magnitude to the spin-up transmission at a higher applied bias near the Fermi level. The spin-up transmission peak below the Fermi energy is observed to be moving away from the Fermi energy as the voltage increases, opposite of what happened in the case of a parallel configuration.

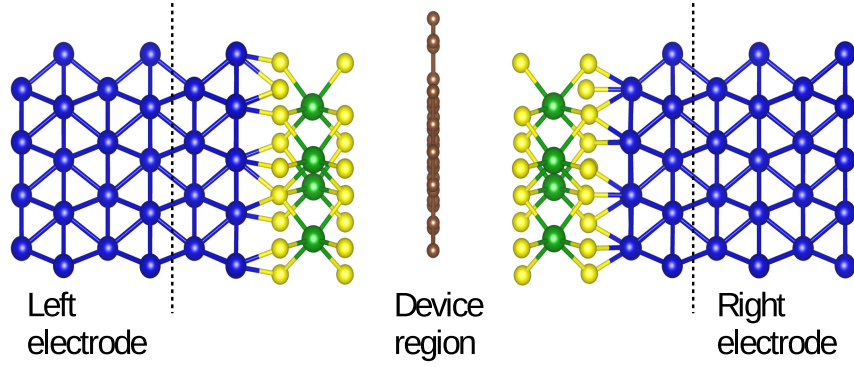


Fig. 4.10: Schematic view of Co/MoS<sub>2</sub>/graphene/MoS<sub>2</sub>/Co device model. Blue, green, yellow, and brown solid spheres represent Co, Mo, S, and C atoms respectively. The device region is shown within the two dashed lines and the remaining parts are the semi-infinite left and right electrodes.

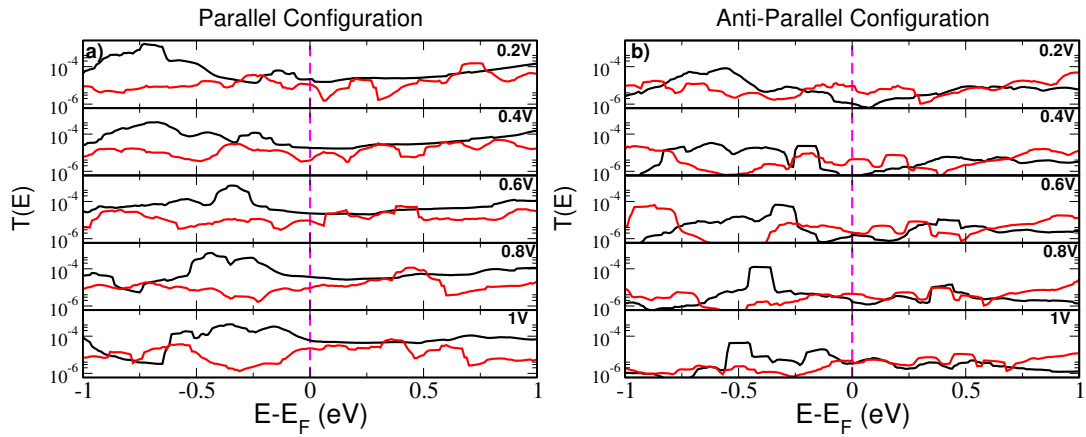


Fig. 4.11: Spin-polarized transmission spectrum of Co/MoS<sub>2</sub>/graphene/MoS<sub>2</sub>/Co magnetic junction in the (a) parallel configuration and in the (b) anti-parallel configuration. Black and red curves represent current through spin-up and spin-down channels respectively.

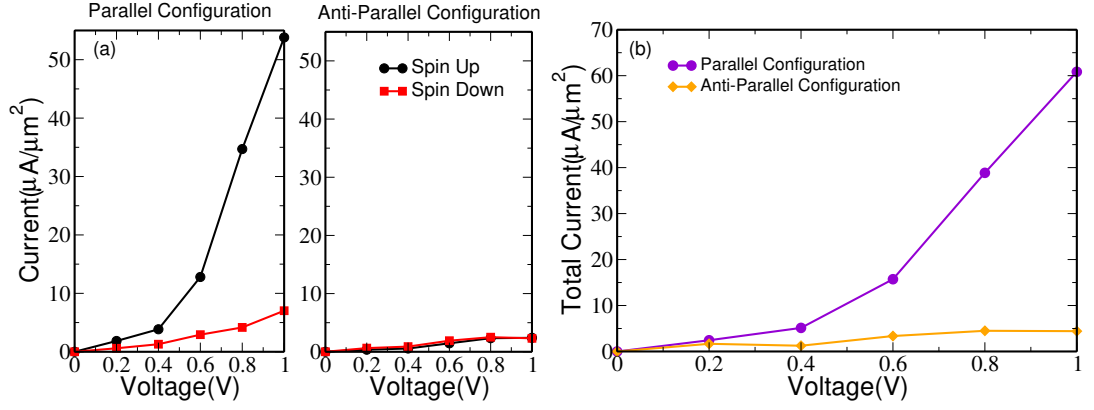


Fig. 4.12: (a) Spin resolved current-voltage characteristics and (b) total current-voltage characteristics of Co/MoS<sub>2</sub>/graphene/MoS<sub>2</sub>/Co magnetic junction in the parallel configuration and anti-parallel configuration.

The spin-resolved current-voltage characteristics in the parallel and anti-parallel configurations are depicted in Fig. 4.12. The calculation shows that the spin current is highly sensitive to the relative magnetic orientation of electrodes. In the parallel configuration, the spin-up current is higher than the spin-down current at all voltages, and their difference is significantly increased at higher voltages. Also, the total current in this configuration is rapidly increasing with an increase of applied bias. Switching of the relative magnetic orientation of electrodes from a parallel to an anti-parallel configuration significantly affects the current-voltage characteristics of the junction. Current through both spin channels is drastically reduced in this configuration. There is hardly any difference observed between the spin-up and spin-down current and the total current remains close to zero in all applied biases as shown in Fig. 4.12(b).

A significantly large difference in the spin-current flow through the junction due to a change in the relative magnetic orientation of the electrodes indicates the possibility of having a high magnetoresistance. So, the magnetoresistance of this system is calculated using different applied bias voltages and is displayed in Fig. 4.13(a). Investigation shows that the MR shoots up as the external bias increases. The calculation estimates a maximum of 1270% MR value in this magnetic junction at 1 V applied bias, which can be considered as an excellent MR value, suitable for manufacturing spintronic devices. One of the main reasons for such a large MR could be due to a large spin injection efficiency (SIE) at the Co-MoS<sub>2</sub> interface as it measures the extent of spin polarization in the transport current. SIE calculated for the magnetic junction using the relation, 4.5 is shown in Fig. 4.13(b). The estimated spin injection efficiency (SIE) in this system remains very high (more than 60%) in the parallel magnetic configuration of electrodes at all applied bias voltages, which is monotonically increased with the increment of the bias voltage.



On the other hand, the SIE is drastically reduced with the increment of the applied bias in the anti-parallel configuration. To gain better insight into the transport

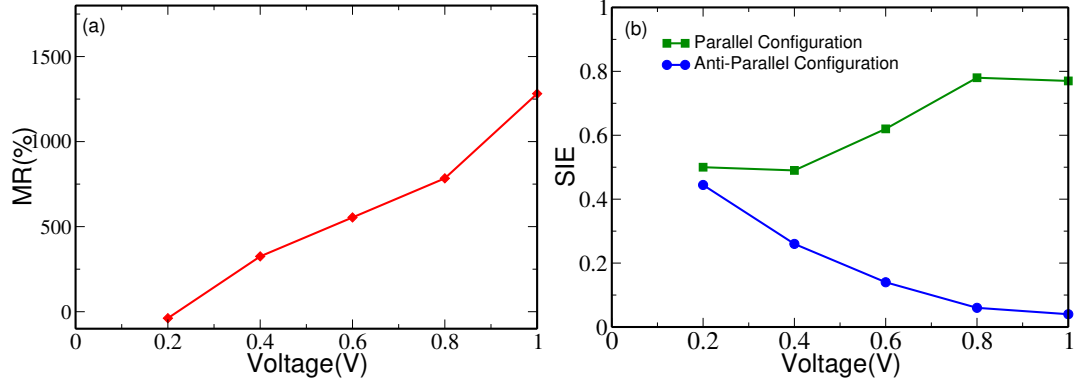


Fig. 4.13: (a) Magnetoresistance (MR) and (b) spin injection efficiency (SIE) of Co/MoS<sub>2</sub>/graphene/MoS<sub>2</sub>/Co magnetic junction in the parallel configuration and anti-parallel configuration.

through the junction, the transmission spectrum across the barrier as a function of the reciprocal  $k_y$  vector component is further calculated. Fig. 4.14 shows spin-resolved  $T(k_y)$  in the parallel and anti-parallel configuration of electrodes at 1 V. High transmission spin-up electrons in the parallel configuration results in a very high spin-up current at 1 V. As discussed earlier the hybridized state appears in

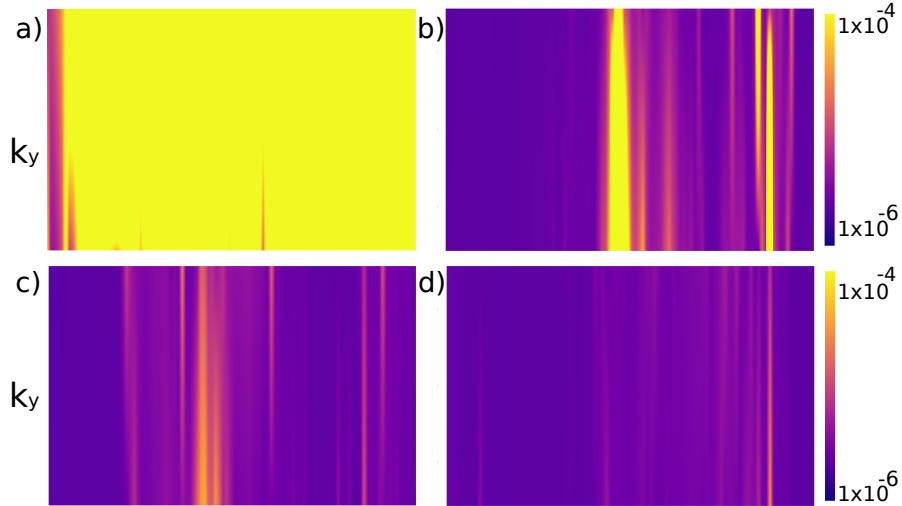


Fig. 4.14: The  $k$ -resolved and spin-resolved transmission spectrum along the  $k_y$  direction. (a)–(d) represent parallel spin-up, parallel spin-down, anti-parallel spin-up, and anti-parallel spin-down configurations of Co/MoS<sub>2</sub>/graphene/MoS<sub>2</sub>/Co magnetic junction, respectively, at an applied bias 1 V.

the Co/MoS<sub>2</sub> junction acts as a spin filter and supports high spin injection into the system when both electrodes are in a parallel configuration. Therefore, in the parallel orientation of electrode magnetization, a large number of spin-polarized

electrons are injected from one electrode. The presence of semi-metal graphene in the scattering region helps to efficiently transport those spin-polarized electrons to the other electrode. On the contrary, a smaller number of spin-polarized electrons are injected into the system from the first electrode in case of antiparallel configuration, which is further scattered back due to the opposite polarity of the second electrode. Hence the current produced in the system is very low as shown in Fig. 4.12(b). At 1 V applied bias, the estimated total currents passing through the junction in the parallel and anti-parallel configurations are 61 and 4  $\mu\text{A}/\mu\text{m}^2$ , respectively. A large difference in current flow through this junction in different magnetic orientations of the electrodes results in a giant magnetoresistance of 1270% in the system.

Although large MR value estimated in this calculation is based on an ideal situation in which a defect-free perfect  $\text{MoS}_2/\text{graphene}/\text{MoS}_2$  spacer has been considered, in reality, impurity/vacancy defects will be present in the scattering region that may reduce the spin polarization of the current through the junction. As a result, inelastic scattering from the impurity/defect site may alter the experimental MR value for this system. Therefore, the calculated MR value from the ballistic transport scenario for a defect-free  $\text{MoS}_2/\text{graphene}/\text{MoS}_2$  junction may be slightly overestimated. However, from this careful study, it is anticipated that  $\text{MoS}_2/\text{graphene}/\text{MoS}_2$  would be an excellent compound for highly efficient spin-valve device applications in the near future.

### 4.3.2 $\text{MoSe}_2$ Based Magnetic Junctions

Transport studies carried out in the  $\text{MoS}_2$  based magnetic junctions have shown that varying the number of layers in the scattering region and modifying the scattering region structure can change the MR values. It is important to know whether it is applicable in magnetic junctions composed of other TMDC materials. For that purpose, another 2D TMDC material  $\text{MoSe}_2$  is considered. Device models of  $\text{MoSe}_2$  based magnetic junctions considered for calculations are shown in Fig. 4.15. A monolayer  $\text{MoSe}_2$  is considered initially as the spacer material. The transmission spectrum is calculated for the magnetic junction in the parallel and anti-parallel magnetic orientations by varying the applied bias from 0.2 V to 1 V. Similar to the monolayer  $\text{MoS}_2$  magnetic junction, a spin-sensitive transmission spectrum is obtained. When transmission through the spin-up channel dominates in the parallel configuration of electrodes, anti-parallel configuration favors the transmission through the spin-down channel (Fig. 4.16(a)). It reflects in the spin-resolved current-voltage characteristics shown in Fig. 4.3(b). A

larger amount of current passes through the spin-up channel when electrodes are in the parallel configuration. In the anti-parallel configuration, it is through the spin-down channel. The total current flowing through Co/monolayer MoSe<sub>2</sub>/Co magnetic junction is more when electrodes are in the parallel configuration as in the previous cases. Even-though transport and current-voltage characteristics of Co/monolayer MoSe<sub>2</sub>/Co magnetic junction shows similarity to Co/monolayer MoS<sub>2</sub>/Co magnetic junction, its variance of magnetoresistance with respect to voltage differ significantly. Here MR is maximum at 0.2 V and then its value reduces on the increment of the applied bias potential. The MR value increases again when the applied bias is 0.6 V and more. The later higher MR is found at 1 V. Even that comes to about half of the MR at 0.2 V. The maximum MR in the bias range is 78%, which is greater than that in the Co/monolayer MoS<sub>2</sub>/Co magnetic junction. Magnetic junctions formed by similar materials producing different MR characteristics open up a possibility to tune MR and obtain better values by changing the spacer material.

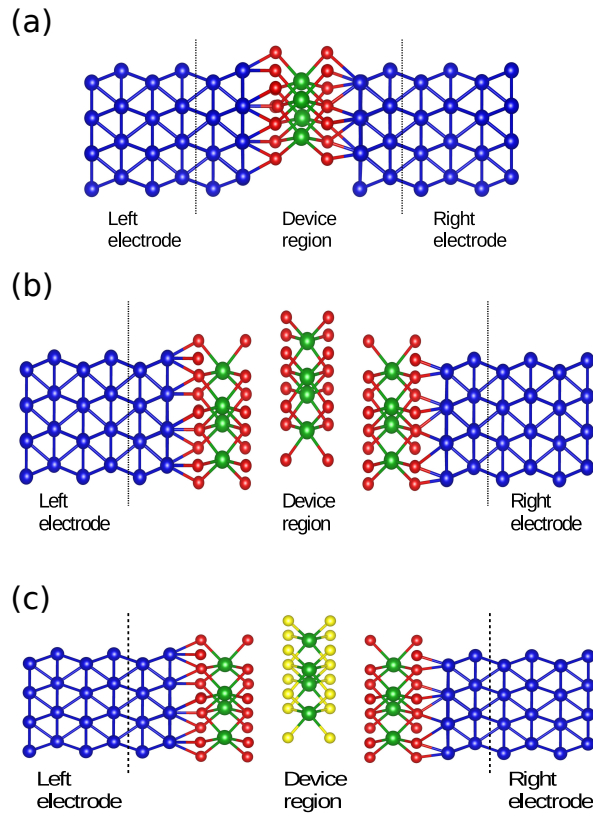


Fig. 4.15: Schematic view of (a) Co/monolayer MoSe<sub>2</sub>/Co, (b) Co/trilayer MoSe<sub>2</sub>/Co and (c) Co/MoSe<sub>2</sub>/MoS<sub>2</sub>/MoSe<sub>2</sub>/Co device model. Blue, green, yellow and red solid spheres represent Co, Mo, S, and Se atoms respectively. The device region is shown within the two dashed lines and the remaining parts are the semi-infinite left and right electrodes.

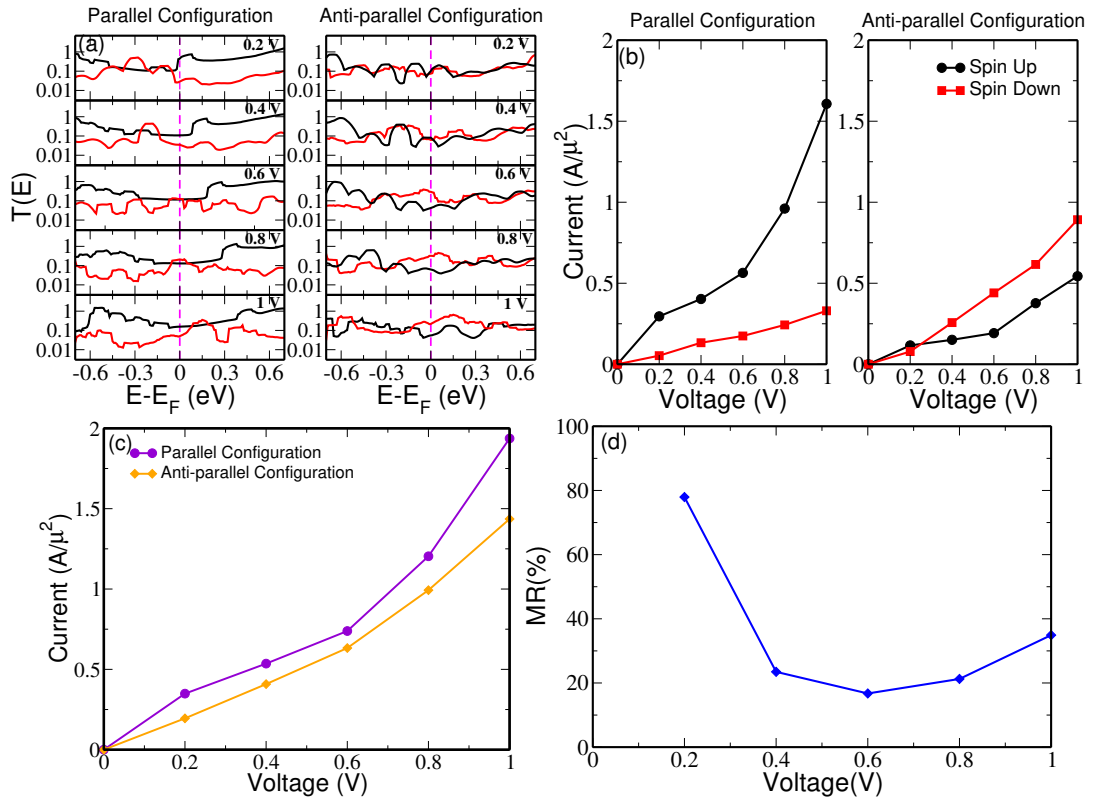


Fig. 4.16: (a) Transmission spectrum, (b) voltage-total current characteristics, (c) voltage-spin current characteristics, and (d) magnetoresistance of Co/monolayer MoSe<sub>2</sub>/Co magnetic junction.

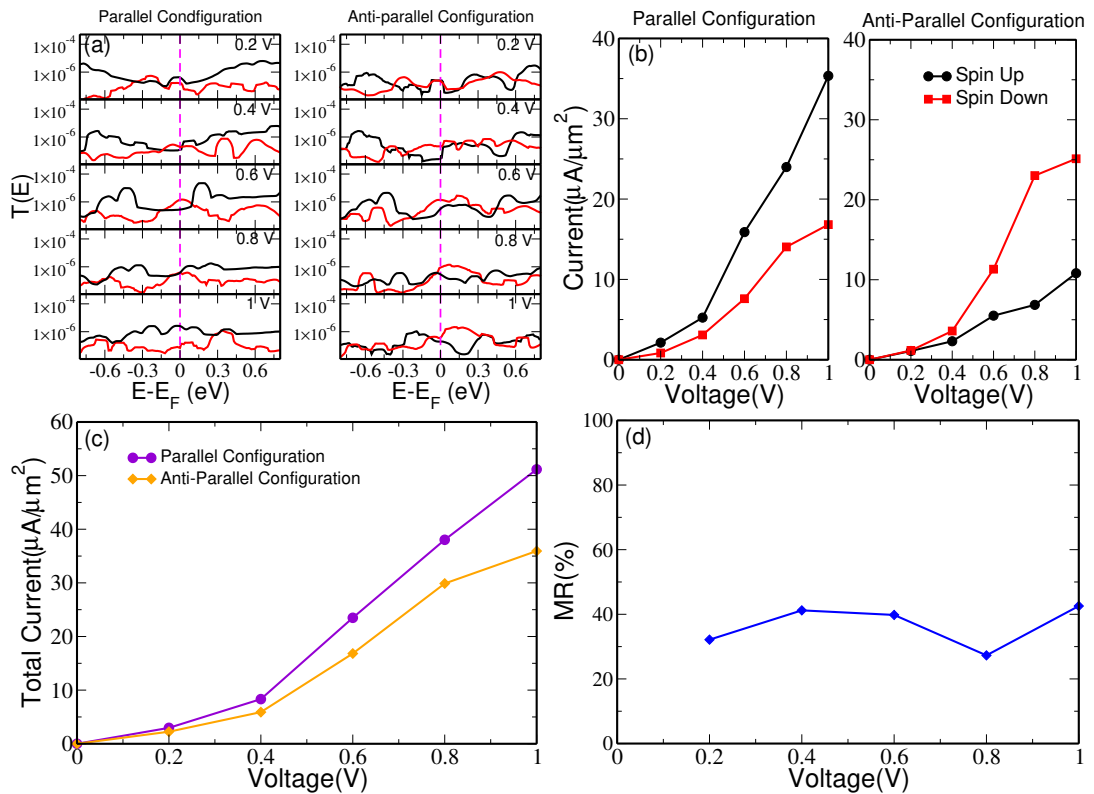


Fig. 4.17: (a) Transmission spectrum, (b) voltage-total current characteristics, (c) voltage-spin current characteristics, and (d) magnetoresistance of Co/trilayer MoSe<sub>2</sub>/Co magnetic junction.

Then the study is continued in multilayer magnetic junctions- Co/trilayer MoSe<sub>2</sub>/Co and Co/MoSe<sub>2</sub>/MoS<sub>2</sub>/MoSe<sub>2</sub>/Co (Fig. 4.15 (b), (c)). The transmission spectrum and voltage-current characteristics of the trilayer magnetic junction resembles the transmission and voltage-current characteristics of the monolayer magnetic junction (Fig. 4.17, Fig. 4.18). Here also change in applied bias and magnetic configuration brings a change in the transmission through the junction. The spin-up current dominates in the parallel configuration and spin-down current dominates in the anti-parallel configuration (Fig. 4.17(b), Fig. 4.18(b)). Similar to the monolayer magnetic junction, in trilayer magnetic junctions more current passes through junction when the electrodes are in the parallel configuration. Even-though magnetoresistance of Co/trilayer MoSe<sub>2</sub>/Co and Co /MoSe<sub>2</sub> /MoS<sub>2</sub> /MoSe<sub>2</sub> /Co magnetic junctions are different (Fig. 4.17(d), Fig. 4.18(d)), in the applied bias range 0 to 1 V, Co/MoSe<sub>2</sub>/MoS<sub>2</sub>/MoSe<sub>2</sub>/Co magnetic junction shows higher magnetoresistance than monolayer and trilayer MoSe<sub>2</sub> magnetic junctions. This magnetic junction exhibits 93 % magnetoresistance at 0.8 V which is the maximum value among three magnetic junctions considered here. The multilayer heterostructure magnetic junction, Co/MoSe<sub>2</sub>/MoS<sub>2</sub>/MoSe<sub>2</sub>/Co not only gives higher MR than the monolayer and trilayer MoSe<sub>2</sub> magnetic junction, but also shows relatively high magnetoresistance in all the applied bias considered.

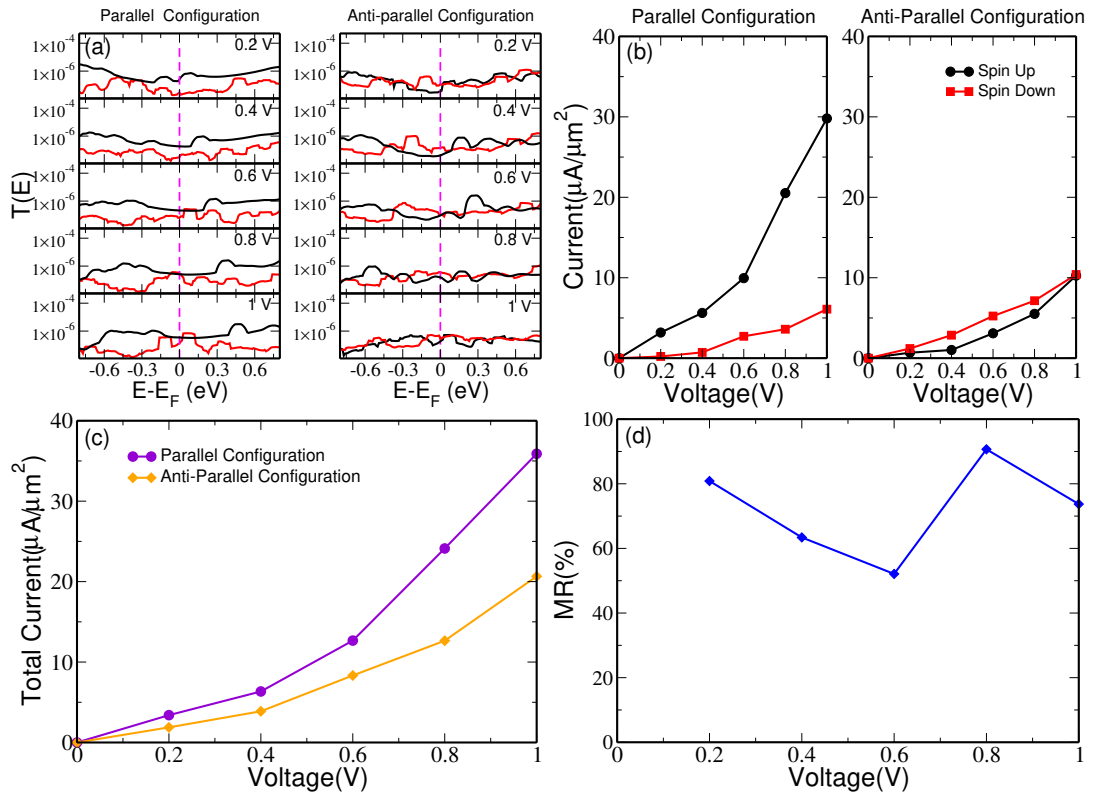


Fig. 4.18: (a) Spin-polarized transmission spectrum, (b) voltage-total current characteristics, (c) voltage-spin current characteristics, and (d) magnetoresistance of Co/MoSe<sub>2</sub>/MoS<sub>2</sub>/MoSe<sub>2</sub>/Co magnetic junction.

### 4.3.3 WS<sub>2</sub> Based Magnetic Junctions

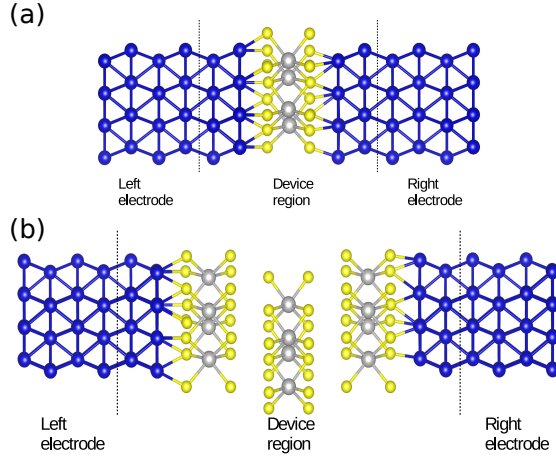


Fig. 4.19: Schematic view of (a) Co/monolayer WS<sub>2</sub>/Co, and (b) Co/trilayer WS<sub>2</sub>/Co device model. Blue, grey, and yellow solid spheres represent Co, W, and S atoms respectively. The device region is shown within the two dashed lines and the remaining parts are the semi-infinite left and right electrodes.

An investigation of transport properties and MR are also carried out in another TMDC 2D material, WS<sub>2</sub>. Similar to the prior studies, here also monolayer magnetic junction is considered first. Device model of Co/monolayer WS<sub>2</sub>/Co magnetic junction is shown in Fig. 4.19(a). As expected from the earlier studies, here also spin dependent transmission spectrum (Fig. 4.20(a)) and voltage-current characteristics (Fig. 4.20(b)) are obtained. The spin-up current is significantly greater than the spin-down current in the parallel configuration of electrodes. The difference between spin-up current and spin-down current decreases in the anti-parallel configuration and spin-down current is greater than spin-up current. The total current through the monolayer WS<sub>2</sub> junction is nearly equal when electrodes are in the parallel and anti-parallel configuration at lower biases. After 0.4 V, the difference in total current is more visible with the change in the magnetic configuration of electrodes. Magnetoresistance calculation shows maximum MR of Co/monolayer WS<sub>2</sub>/Co magnetic junction in the bias range 0.2 to 1 V is at 0.2 V. MR at this bias is 49%. MR value decreases further, but not in a uniform manner. The second highest MR is at 0.6 V, which is equal to 41.71%. Interestingly the minimum MR value of 18.49% is obtained at higher bias 1 V.

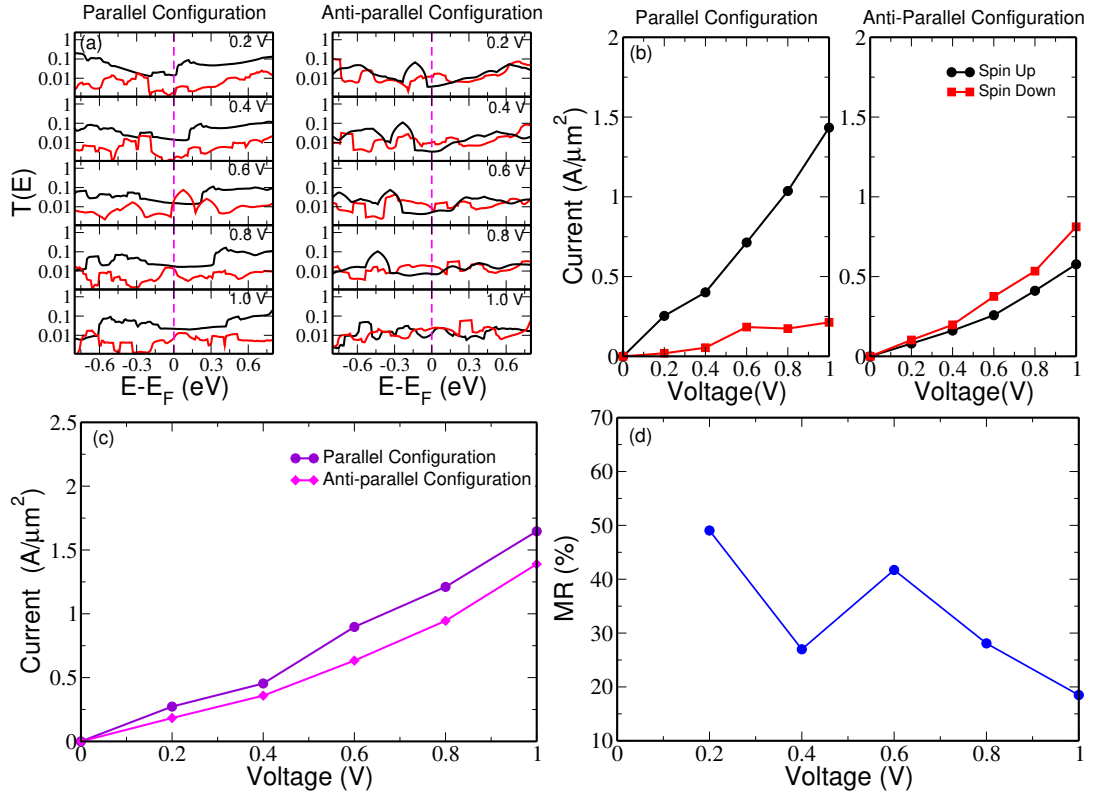


Fig. 4.20: (a) Spin-polarized transmission spectrum, (b) voltage-total current characteristics, (c) voltage-spin current characteristics, and (d) magnetoresistance of Co/monolayer WS<sub>2</sub>/Co magnetic junction.

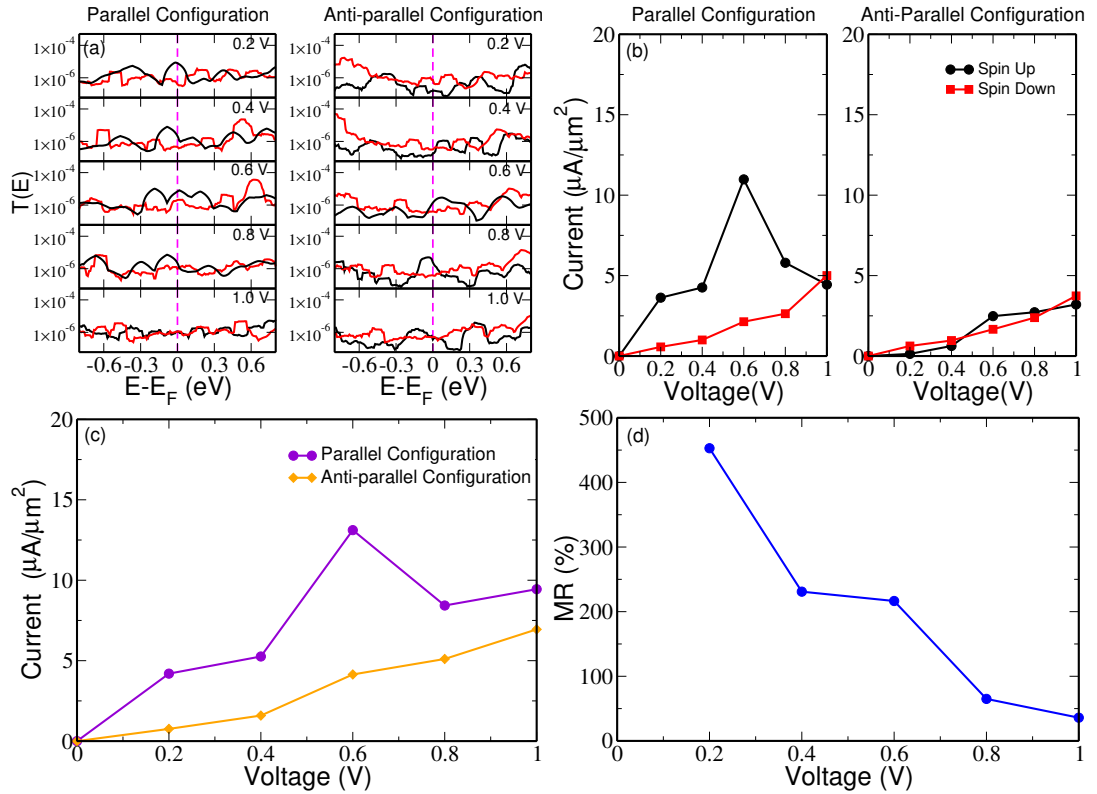


Fig. 4.21: (a) Spin-polarized transmission spectrum, (b) voltage-total current characteristics, (c) voltage-spin current characteristics, and (d) magnetoresistance of Co/trilayer WS<sub>2</sub>/Co magnetic junction.

A completely different MR spectrum is seen in the case of trilayer MoS<sub>2</sub> magnetic junction (Fig. 4.21(d)). An increase in the number of layers in the spacer region of Co/WS<sub>2</sub>/Co magnetic junction brings a significant change in the MR. The difference obtained in the maximum MR between monolayer and trilayer junction in the WS<sub>2</sub> magnetic junction is much greater than that obtained for MoS<sub>2</sub> and MoSe<sub>2</sub> magnetic junctions. Maximum MR obtained for trilayer WS<sub>2</sub> magnetic junction is 450%, whereas the same for trilayer MoS<sub>2</sub> junction is 76% and MoSe<sub>2</sub> junction is 43%. The bias voltage of 0.2 V gives maximum MR in the trilayer WS<sub>2</sub> magnetic junction. MR value decreases further. But 0.4 and 0.6 V also give comparatively higher MR values, 228% and 216% respectively. Unlike the other junctions with different TMDC compounds, the high MR value in this system is not sustained at a higher bias range.

## 4.4 Conclusion

In conclusion, spin transport through various magnetic junctions composed of 2D TMDC materials is studied using the combination of DFT and NEGF methods. Co, a ferromagnetic metal with high spin polarization, has been considered as the electrode material. Monolayers, trilayers, and heterostructures of TMDC materials are considered in the device region of the two probe models. Spin-polarized transmission and currents are calculated in each magnetic junction at various applied bias voltages in the parallel and anti-parallel relative magnetic configurations. Changes in the applied bias and relative magnetic configuration of electrodes changes the transport properties. Magnetoresistance is also calculated for all magnetic junctions at various applied bias. The study showed MR can be tuned by varying the number of layers and type of layers in the device region as well as by varying applied bias. A giant MR value of 1270% is estimated in the Co/MoS<sub>2</sub>/graphene/MoS<sub>2</sub>/Co magnetic junction at an external bias of 1 V, which is the maximum value obtained in this whole study. The device parameters obtained show that Co/MoS<sub>2</sub>/graphene/MoS<sub>2</sub>/Co magnetic junction can be a promising candidate for designing future spintronic devices.



# Chapter 5

## Electronic Structure of Two-Dimensional Ferromagnetic Materials

### 5.1 Introduction

The search is constantly underway for suitable low-dimensional materials to build spintronics devices. 2017 witnessed some of the most promising findings for those involved in such investigations. Experiments by Zhang *et al.* and Xu *et al.* found that layered magnetic compounds retain their magnetic properties up to monolayers. Since this intrinsic ferromagnetic behaviour is very desirable for spintronics devices, it is expected that such materials will lead to better spintronic devices. Recent experiments and studies show that layered magnetic compounds, chromium tri-halides ( $\text{CrX}_3$ ) integrated with 2D materials are viable for realizing efficient magnetic junctions. Therefore, it is essential to study heterostructures composed of  $\text{CrX}_3$  and 2D materials. Liu *et al.* thoroughly investigated  $\text{CrX}_3$ /graphene interfaces using the first principle calculation and showed spin-dependent Schottky barrier at the interface (Li *et al.*, 2020). A detailed understanding of the  $\text{CrX}_3$  interfaces with other 2D materials essential for device application is still lacking and needs further exploration.

This chapter, therefore, discusses the electronic structure and magnetic properties of 2D ferromagnetic materials - chromium tri-halides. The interface structures of monolayer  $\text{CrX}_3$  materials with various TMDC layers materials previously studied in detail have been constructed and studied. The detailed theoretical result of this study has also been discussed here.

## 5.2 Methodology

Structural relaxations and electronic properties were calculated using density functional theory as implemented in the Vienna Ab initio Simulation Package (VASP) (Kresse and Furthmüller, 1996). The exchange-correlation is evaluated using the generalized gradient approximation (GGA) as suggested by Perdew, Burke, and Ernzerhof (PBE) (Perdew et al., 1996). The on-site Coulomb repulsion of Cr 3d electrons was taken into account using the DFT + U method with  $U_{Cr}$  as 5 eV (Yang et al., 2020). Interlayer van der Waals interactions are adjusted using the dispersion-corrected DFT method (DFT-D3) (Grimme et al., 2010, 2011).

The plane wave cut-off is taken as 450 eV. A vacuum thickness of more than 10 Å is used to avoid the artificial interaction between the images of slabs. The forces acting on atoms are calculated by using the Hellmann-Feynman theorem and subsequently, the geometric structure relaxation was performed using the conjugate-gradient method. The convergence criteria set for electronic energy was  $10^{-5}$  eV and with the convergence for interatomic forces on all atoms set to  $0.01 \text{ eV}\text{Å}^{-1}$ . The Brillouin zone is sampled with a Monkhorst–Pack grid (Monkhorst and Pack, 1976) with k points mesh of  $3\times 3\times 1$  for geometry optimization. A denser mesh of  $12\times 12\times 1$  was used for the electron density of states  $D(E)$ , and atom projected density of states (PDOS) calculation.

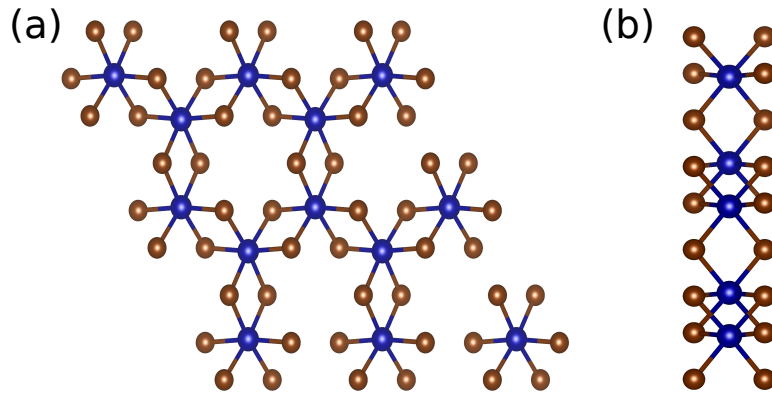


Fig. 5.1: Top (a) and side view (b) of  $\text{CrX}_3$  monolayer. Blue and brown solid spheres represent Cr and X ( $X = \text{Cl}, \text{Br}$  and  $\text{I}$ ) atoms respectively.

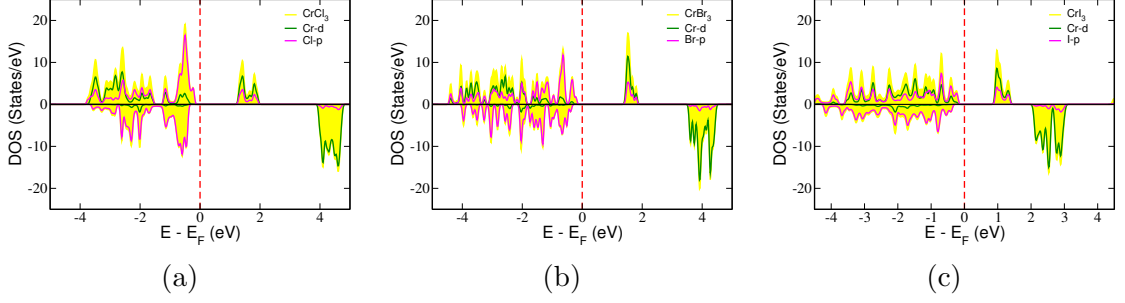


Fig. 5.2: Spin polarised density of states (DOS) of  $\text{CrX}_3$  monolayers. (a), (b), and (c) represent spin polarized DOS of  $\text{CrCl}_3$ ,  $\text{CrBr}_3$  and  $\text{CrI}_3$  respectively. Yellow shaded region represents total DOS. The green color curve represents Cr-d orbital and magenta represents X-p orbital. The Fermi energy is set to zero.

	$E_{gup}$ eV	$E_{gdn}$ eV	$\Delta_{cbm}$ eV	$\Delta_{vbm}$ eV
$\text{CrCl}_3$	2.45	4.38	2.69	-0.21
$\text{CrBr}_3$	1.68	3.91	2.07	-0.19
$\text{CrI}_3$	1.16	2.47	1.13	-0.17

Table 5.1: Band gap in spin-up direction ( $E_{gup}$ ), band gap spin-down direction ( $E_{gdn}$ ), difference of the band edge energy between the two spin components for the conduction band minimum ( $\Delta_{cbm}$ ) and the valance band maximum ( $\Delta_{vbm}$ ) of  $\text{CrX}_3$  monolayers are given in the table.

## 5.3 Results and Discussions

### 5.3.1 Monolayer $\text{CrX}_3$ Materials

To start with, structural, electronic, and magnetic properties of monolayer chromium tri-halides ( $\text{CrX}_3$ ) are obtained. Hexagonal  $\text{CrX}_3$  structures with Cl, Br, and I atoms as X are considered. As shown in Fig.5.1, Cr atoms, which are marked in blue, are arranged in a plane, forming a honeycomb lattice. Each Cr atom is surrounded by six nearest neighboring X atoms, which are arranged in an octahedron. In Fig. 5.1, X atoms are marked in red. The optimised lattice parameters for  $\text{CrX}_3$  are 6.045 Å ( $\text{CrCl}_3$ ), 6.446 Å ( $\text{CrBr}_3$ ) and 7.007 Å ( $\text{CrI}_3$ ). The lattice parameter increases with an increase in the atomic number of the halogen atom X. The bond length between Cr-Cl, Cr-Br, and Cr-I are measured as 2.38 Å, 2.55 Å, and 2.78 Å. Obtained values of lattice parameters and Cr-X bond lengths in optimized structures agree well with the reported values from the previous studies. (Yang et al., 2020; Liu et al., 2016). Next, we calculated the electronic structure of monolayer chromium tri-halides. The density of states (DOS) and band structures of monolayer chromium tri-halides are shown in Fig. 5.2 and Fig. 5.3, respectively. A clear distinction is observed in the density of states available for spin-up and

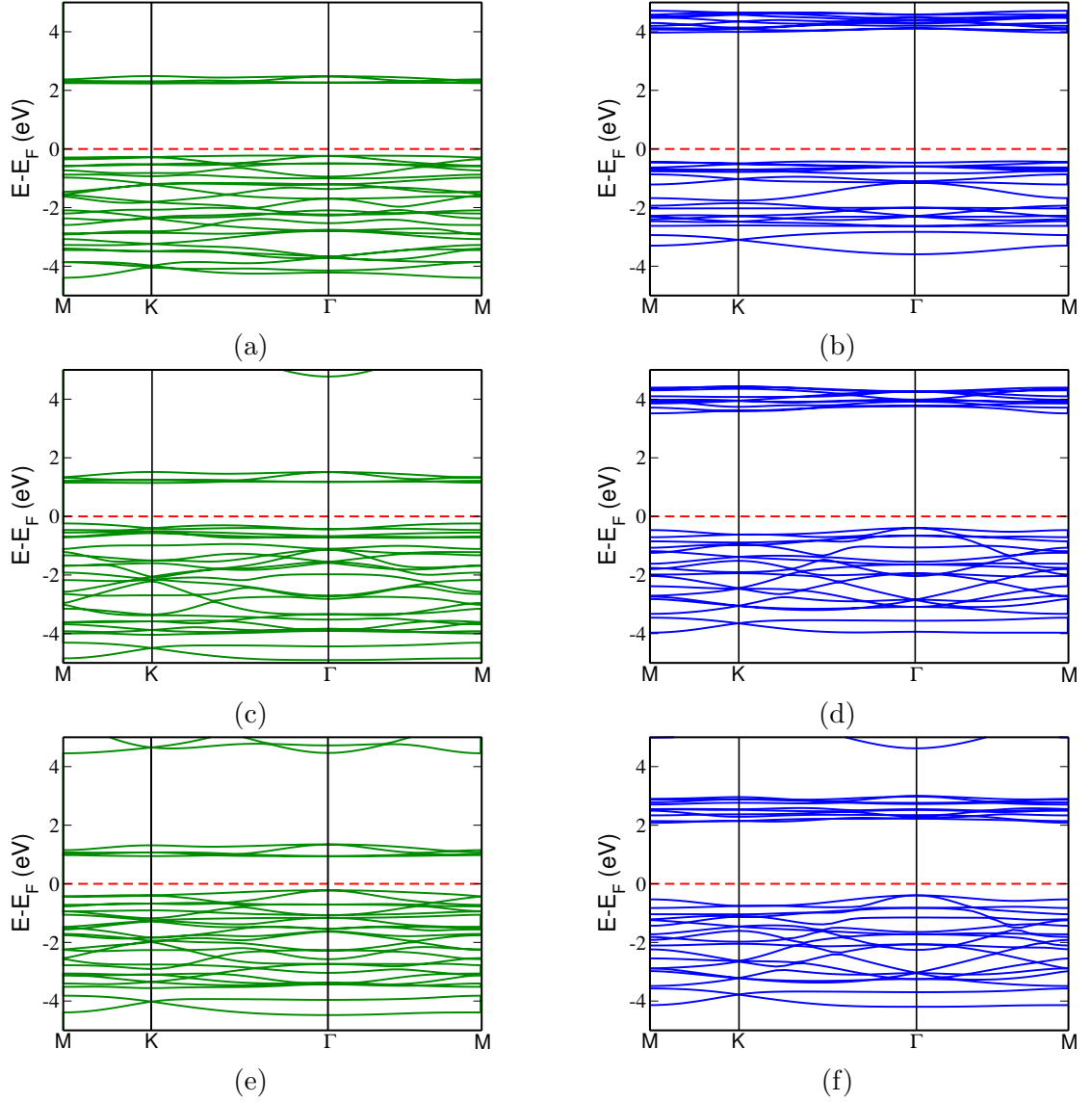


Fig. 5.3: Spin polarised band structures of  $\text{CrX}_3$  monolayers. (a), (c), and (e) represent spin-up band structures of  $\text{CrCl}_3$ ,  $\text{CrBr}_3$  and  $\text{CrI}_3$ . (b), (d), and (f) represent spin-down band structures of  $\text{CrCl}_3$ ,  $\text{CrBr}_3$  and  $\text{CrI}_3$ . Green curves represent spin-up band structures and blue curves represents spin-down band structures. The Fermi energy is set to zero.

spin-down electrons in all  $\text{CrX}_3$  monolayers. Unlike the other 2D semiconductors, a large exchange splitting is present between two different spin-channels, which further leads to different bandgaps for spin-up and spin-down density of states (Table.5.1). Interestingly a partial conducting characteristic to  $\text{CrX}_3$  monolayers is observed in our study. Calculations show that the bandgap decreases with an increase in the atomic number of X. Since the conduction band and valence band edges are fully spin polarised, the difference of band edge energy between two spin components is also estimated. The difference of band edge energy between spin-up and spin-down component for conduction band and valence band are defined as  $\Delta_{cbm} = E_{cbm}^{down} - E_{cbm}^{up}$  and  $\Delta_{vbm} = E_{vbm}^{down} - E_{vbm}^{up}$  respectively (Zhang et al., 2015). Here  $E_{cbm}^{up(down)}$  denotes band edge energy of spin-up (spin-down) at the conduction band and  $E_{vbm}^{up(down)}$  denotes band edge energy of spin-up (spin-down) at the valence band. The calculated values are displayed in Table.5.1. High  $\Delta_{cbm}$  hints at the potential of using  $\text{CrX}_3$  monolayers for spin-polarized carrier injection and detection. Note that the occupied Cr-3d orbitals are present only in the spin-up channel (Fig. 5.2 ). Spin-down Cr-3d orbitals are completely unoccupied (Zhang et al., 2015). Also the X-p orbital is dominating the valence band edge in the spin-down channel irrespective of the X atom in chromium tri-halides. Whereas, both Cr-3d orbital and X-p orbital contribute to the valence band edge for the spin-up channel. Interestingly, the contribution from Cr-d orbital reduces as the atomic number of X increases. Our calculation also shows that  $\text{CrX}_3$  monolayers are robust intrinsic ferromagnetic materials with a high magnetic moment. In  $\text{CrCl}_3$ , Cr atoms have a local magnetic moment of  $3.195 \mu_B$ . A tiny magnetic moment of  $0.084 \mu_B$  also present on each Cl atoms and are anti-parallel to the Cr spin moment. The magnetic moments on atoms in  $\text{CrBr}_3$  are more than that in the  $\text{CrCl}_3$ . In  $\text{CrBr}_3$  magnetic moment of Cr and Br is  $3.353 \mu_B$  and  $-0.125 \mu_B$ , respectively. The maximum value of atomic moment is observed in  $\text{CrI}_3$  system. Here Cr possesses a magnetic moment of  $3.592 \mu_B$  which is greater than that in the other two monolayers. I-atoms also possess relatively higher magnetic moment of  $0.176 \mu_B$  which is aligned opposite to the Cr moment direction. Note that the atomic magnetic moment of Cr atom in different  $\text{CrX}_3$  system systematically reduces with the increment of the electro-negativity of the X atom. This could be the effect of stronger Cr-X covalent bonding.

### 5.3.2 $\text{CrX}_3$ /TMDC Heterostructure

Next, the  $\text{CrX}_3$ /TMDC heterostructures are modelled by superimposing  $2 \times 2$  supercell of the TMDC ( $\text{MoS}_2$ ,  $\text{MoSe}_2$ ,  $\text{WS}_2$ , and  $\text{WSe}_2$ ) and  $1 \times 1$  cell of  $\text{CrX}_3$  (Fig. 5.4). The interlayer distance is measured for the optimized structures and is

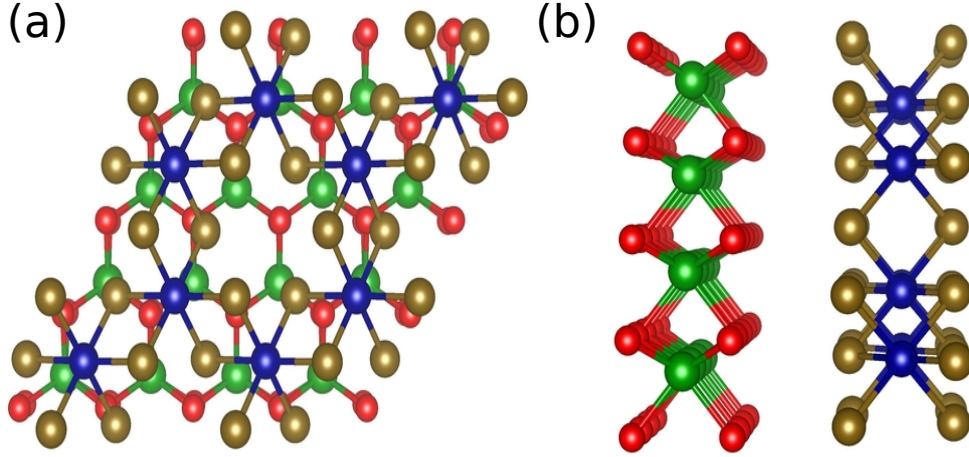


Fig. 5.4: Top (a) and side view (b) of supercell of  $\text{CrX}_3/\text{TMDC}$  heterostructure. Blue and brown solid spheres represent Cr and X atoms in the  $\text{CrX}_3$  monolayer respectively. X can be Cl, Br and I. Green and red solid spheres represent atoms in the TMDC monolayer. Green spheres can be Mo or W and red spheres can be S or Se atoms.

given in Table.5.2. The interlayer distance in all these structures is greater than the sum of covalent atomic radii of the halogen atom in the  $\text{CrX}_3$  and chalcogen atom in the TMDC. This implies that there is no covalent bond existing that exists between two different  $\text{CrX}_3$  and TMDC monolayers. Therefore  $\text{CrX}_3$  and TMDC monolayer interact through van der Waals force.

The cohesive energy ( $E_{\text{coh}}$ ) is calculated for  $\text{CrX}_3/\text{TMDC}$  heterostructures using the relation,

$$E_{\text{coh}} = E_{\text{CrX}_3/\text{TMDC}} - E_{\text{CrX}_3} - E_{\text{TMDC}} \quad (5.1)$$

where  $E_{\text{CrX}_3/\text{TMDC}}$ ,  $E_{\text{CrX}_3}$ , and  $E_{\text{TMDC}}$  represent the total energy of the relaxed  $\text{CrX}_3/\text{TMDC}$  heterostructure, isolated  $\text{CrX}_3$  monolayer and isolated TMDC monolayer. The negative cohesive energy values obtained in each case as shown in the Table.5.2 indicate that  $\text{CrX}_3/\text{TMDC}$  form stable interfaces.

The electronic structures of optimized  $\text{CrX}_3/\text{TMDC}$  heterostructures are calculated, which shows that DOS and band structure of different  $\text{CrX}_3/\text{TMDC}$  structures have similar features. The DOS of  $\text{CrBr}_3/\text{TMDC}$  heterostructures are displayed in Fig. 5.5 considering four different TMDC monolayers  $\text{MoS}_2$ ,  $\text{MoSe}_2$ ,  $\text{WS}_2$  and  $\text{WSe}_2$ . The interlayer interactions do not considerably alter the characteristics of  $\text{CrBr}_3$ . Cr-d and Br-p states are not disturbed in a significant manner. Spin-dependent characteristics of isolated  $\text{CrBr}_3$  are preserved in all these heterostructures. The bandgap of  $\text{CrX}_3$  monolayers in the heterostructure form is

	<b>d</b> (Å)	$E_{coh}$ (eV)	$\phi_{SB_e}^{up}$ (eV)	$\phi_{SB_e}^{dn}$ (eV)	$\phi_{TB}$ (eV)
CrCl <sub>3</sub> /MoS <sub>2</sub>	3.35	-0.46	0.26	1.97	5.62
CrCl <sub>3</sub> /MoSe <sub>2</sub>	3.71	-0.57	0.07	1.80	5.42
CrCl <sub>3</sub> /WS <sub>2</sub>	3.32	-0.48	0.15	1.86	5.64
CrCl <sub>3</sub> /WSe <sub>2</sub>	3.64	-0.58	0.06	1.76	5.43
CrBr <sub>3</sub> /MoS <sub>2</sub>	3.35	-0.63	0.61	2.52	6.43
CrBr <sub>3</sub> /MoSe <sub>2</sub>	3.36	-0.67	0.10	2.31	6.01
CrBr <sub>3</sub> /WS <sub>2</sub>	3.37	-0.65	0.42	2.37	6.44
CrBr <sub>3</sub> /WSe <sub>2</sub>	3.37	-0.62	0.05	2.30	5.99
CrI <sub>3</sub> /MoS <sub>2</sub>	3.52	-0.81	0.35	2.70	5.47
CrI <sub>3</sub> /MoSe <sub>2</sub>	3.66	-0.71	0.20	2.33	5.81
CrI <sub>3</sub> /WS <sub>2</sub>	3.60	-0.82	0.19	2.59	5.55
CrI <sub>3</sub> /WSe <sub>2</sub>	3.58	-0.79	0.06	2.42	5.38

Table 5.2: The calculated parameters in CrX<sub>3</sub>/TMDC. The interlayer distance (d), cohesive energy ( $E_{coh}$ ), Schottky barrier height for spin-up electron ( $\phi_{SB_e}^{up}$ ) and spin-down electron ( $\phi_{SB_e}^{dn}$ ) and tunnel barrier height ( $\phi_{TB}$ ).

also very close to that in the isolated structure. But the position of CBM and VBM of CrBr<sub>3</sub> changes concerning the Fermi level in each heterostructure.

The contact properties of CrX<sub>3</sub>/TMDC heterostructures are investigated next. Electron transports through CrX<sub>3</sub>/TMDC encounter the Schottky barrier and tunnel barrier. The Schottky barrier height is estimated from the electronic band structure of CrBr<sub>3</sub>/TMDC heterostructures. Spin-up and spin-down band structures plotted separately are shown in Fig. 5.6. The Schottky barrier height for spin-up and spin-down electrons ( $\phi_{SB_e}^{up/dn}$ ) are estimated using Schottky-Mott rule (Tung, 2014),

$$\phi_{SB_e}^{up/dn} = E_{CBM}^{up/dn} - E_F \quad (5.2)$$

Here,  $E_F$  represents the Fermi energy.  $E_{CBM}^{up/dn}$  represents the energy of the conduction band minimum (CBM) in spin-up/down directions of CrX<sub>3</sub> in the heterostructure.

Schottky barrier height calculated for spin-up and spin-down electrons ( $\phi_{SB_e}^{up/dn}$ ) in various CrX<sub>3</sub>/TMDC heterostructures are listed in Table.5.2. Calculation shows that the Schottky barrier height for spin-up electrons is much less than that of spin-down electrons in all structures. Therefore, spin-up and spin-down electrons encounter different barriers while transporting through the interface due to the exchange spin splitting in magnetic semiconductor CrX<sub>3</sub>, which in turn produces a spin filtering effect at the interface.

From Table.5.2, it can be seen that difference between  $\phi_{SB_e}^{up}$  and  $\phi_{SB_e}^{dn}$  is rela-

tively more in CrI<sub>3</sub>/TMDC heterostructures and less in CrCl<sub>3</sub>/TMDC heterostructures. We also observed low  $\phi_{SB_e}^{up}$  for CrX<sub>3</sub> spin-up electron when they come across a WSe<sub>2</sub> barrier.

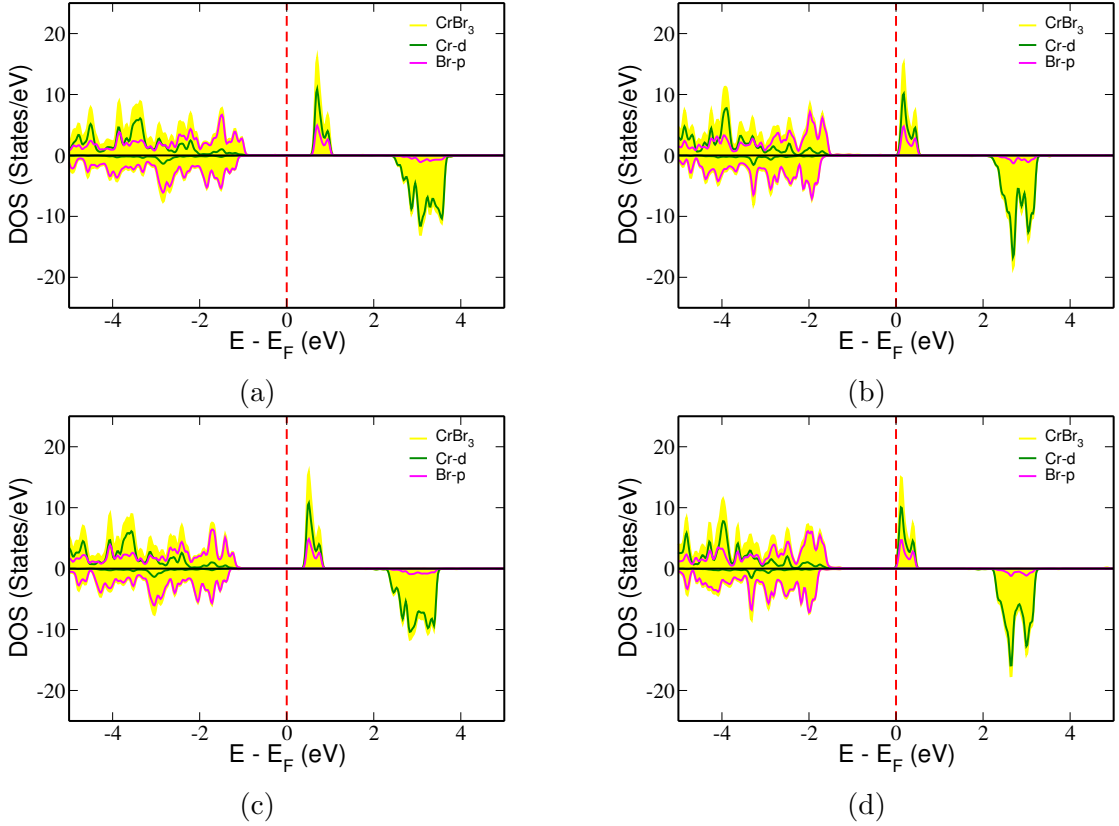


Fig. 5.5: Spin polarised density of states (DOS) of CrBr<sub>3</sub> monolayer in CrBr<sub>3</sub>/TMDC heterostructures. (a), (b), (c), and (d) represent spin polarized DOS of CrBr<sub>3</sub> in CrBr<sub>3</sub>/MoS<sub>2</sub>, CrBr<sub>3</sub>/MoSe<sub>2</sub>, CrBr<sub>3</sub>/WS<sub>2</sub> and CrBr<sub>3</sub>/WSe<sub>2</sub> heterostructures. Yellow shaded region represents total DOS of CrBr<sub>3</sub>. The green color curve represents Cr-d orbital and magenta represent X-p orbital. The Fermi energy is set to zero.



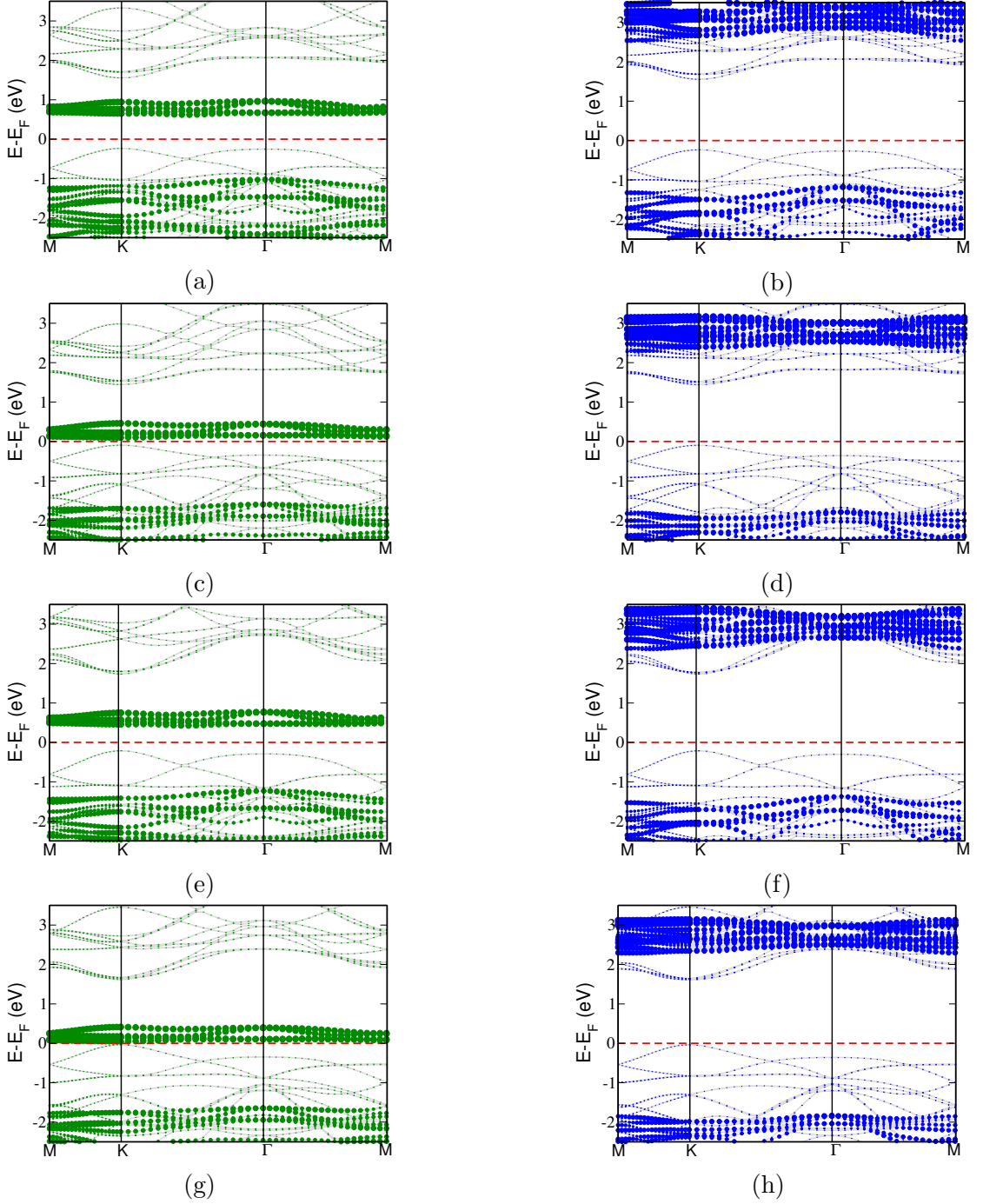


Fig. 5.6: Spin polarised band structure of  $\text{CrBr}_3/\text{TMDC}$  heterostructures. (a), (c), (e), and (g) represent spin-up bandstructure of  $\text{CrBr}_3/\text{MoS}_2$ ,  $\text{CrBr}_3/\text{MoSe}_2$ ,  $\text{CrBr}_3/\text{WS}_2$  and  $\text{CrBr}_3/\text{WSe}_2$  heterostructures. Green lines represent projected bands of  $\text{CrBr}_3$ . (b), (d), (f), and (h) represent spin-down band structure of  $\text{CrBr}_3/\text{MoS}_2$ ,  $\text{CrBr}_3/\text{MoSe}_2$ ,  $\text{CrBr}_3/\text{WS}_2$  and  $\text{CrBr}_3/\text{WSe}_2$  heterostructures. Blue lines represent projected bands of  $\text{CrBr}_3$ . The Fermi energy is set to zero.

Since there is no strong orbital overlap at the  $\text{CrX}_3/\text{TMDC}$  interface, there exists a significant tunnelling barrier at the van der Waals contact (Allain et al., 2015). Tunnelling barrier is characterized by tunnelling barrier height ( $\phi_{TB}$ ), and

tunnelling barrier width ( $w_{TB}$ ) (Jin et al., 2017). Electron injection efficiency is high when  $\phi_{TB}$  is low and  $w_{TB}$  is narrow. The effective potential ( $V_{eff}$ ) at the interface- which represents the carrier interaction with other electrons, and the external electrostatic field determines the magnitude of tunnelling barrier (Shen et al., 2019). The estimated  $\phi_{TB}$  values for  $\text{CrX}_3/\text{TMDC}$  heterostructures are given in Table.5.2. These values are much larger than metal/TMDC tunnelling barrier height (Popov et al., 2012). But these values are comparable to  $\text{CrX}_3/\text{graphene}$  tunnelling barrier height (Li et al., 2020). As the tunnelling barrier is determined by the Coulomb interaction, it does not show any spin dependency. However, the transport of electrons in  $\text{CrX}_3/\text{TMDC}$  heterostructure will be spin-dependent since spin-up electrons and spin-down electrons experience different Schottky barrier heights at the interface. Therefore, a significant difference in the Schottky barrier height can induce a highly spin-polarized transmission through the interface. Hence  $\text{CrX}_3/\text{TMDC}$  heterostructures can be considered as suitable materials for spin transport devices.

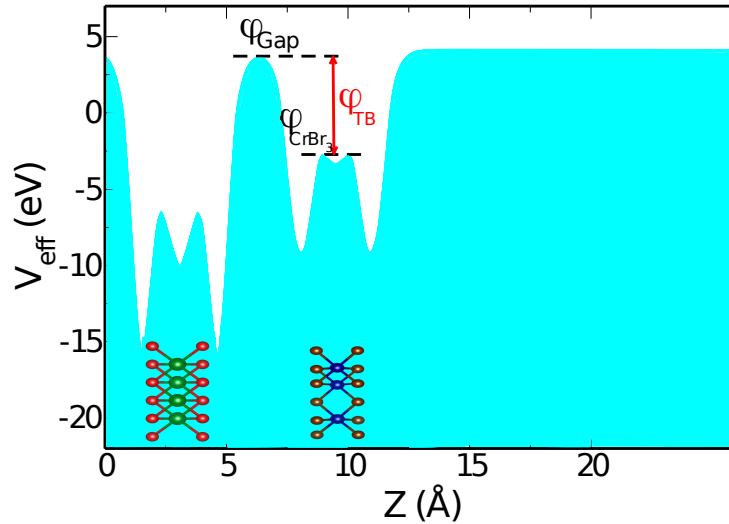


Fig. 5.7: Effective potential profile of the  $\text{MoS}_2/\text{CrBr}_3$  interface.

## 5.4 Conclusion

The electronic and magnetic properties of monolayer  $\text{CrX}_3$  materials are studied using first-principle electronic structure calculations. High band edge energy difference in monolayer  $\text{CrX}_3$  materials indicate that these materials are suitable for spintronic applications.  $\text{CrX}_3/\text{TMDC}$  van der Waals heterostructures are modeled

and interface properties are systematically studied. The electronic structure calculations showed that the interlayer interaction between  $\text{CrX}_3$  and TMDC monolayer does not significantly alter the electronic properties of  $\text{CrX}_3$ . A substantial spin-dependent Schottky barrier exists for electrons in the  $\text{CrX}_3$  monolayer when they form a heterostructure with TMDC monolayers.  $\text{CrX}_3/\text{TMDC}$  heterostructure can act as an efficient spin filter tunnel barrier. Comparing the results obtained for various  $\text{CrX}_3/\text{TMDC}$  heterostructures showed that the interface properties can be tuned by varying the materials. These results also guide to tune Schottky barrier height and tunnel barrier height of  $\text{CrX}_3$  monolayers and provide insight into realizing  $\text{CrX}_3/\text{TMDC}$  based magnetic tunnel junctions.

# Chapter 6

## Spin Transport in Magnetic Junctions with 2D Ferromagnetic Materials

### 6.1 Introduction

The electronic structure studies carried out in recently discovered 2D ferromagnetic materials-CrX<sub>3</sub>-show that these materials are well suited for spintronic applications. Magnetic tunnel junction (MTJ) is one area where 2D ferromagnetic materials can find wide-ranging applications soon. Ferromagnetic materials have a crucial role in magnetic tunnel junctions as a spin filter. Magnetic junction with 2D ferromagnetic materials and van der Waals heterostructure can perform better spin filtering than a traditional magnetic junction. The flat atomic interface in van der Waals heterostructures can render uniform tunnelling, leading to high magnetoresistance (Li et al., 2020). Furthermore, the interlayer space in van der Waals heterostructures can serve as a natural tunnelling barrier.

Only a limited number of research works have been carried out so far about the magnetic junctions with chromium tri-halides. A large magnetoresistance is reported in graphite/CrI<sub>3</sub>/graphite junctions as a function of magnetic field and temperature (Klein et al., 2018). Kim *et al.* demonstrated a tunnel junction heterostructure consisting of CrI<sub>3</sub>, sandwiched between few-layers of graphene electrodes and sealed with hexagonal boron nitride (hBN) and observed a substantial negative magnetoresistance (Kim et al., 2018). They have extended transport study to hBN/graphene/CrX<sub>3</sub>/graphene/hBN van der Waals heterostructure magnetic junction by changing bias, temperature, and thickness (Kim et al., 2019).

Their experimental observations show that thicker samples with smaller work function graphene electrodes generally show higher MR. This is due to multiple spin filters of tunnelling electrons acting in series. This chapter describes our recent spin-transport study on this material. The ferromagnetic Co has been considered as lead material and the magnetic junctions are composed of trilayer CrX<sub>3</sub>s and heterostructures of CrX<sub>3</sub> and TMDC materials.

## 6.2 Methodology

The structures used for the transport calculation are optimized within the density functional theory (DFT) framework, as implemented in the SIESTA package (Soler et al., 2002). A 300 Ry mesh cut-off is used for the self-consistent calculation. A linear combination of numerical atomic orbitals with double zeta polarizations (DZP) basis set is used.

The transport properties of magnetic junctions are investigated with the fully self-consistent NEGF method as implemented in the TranSIESTA. The transmission spectrum which describes the probability for an electron with incident energy  $E$  under bias voltage  $V_b$  to transfer from the left semi-infinite electrode to the right semi-infinite electrode is calculated. The spin dependent ( $\sigma = \uparrow$  or  $\downarrow$ ) transmission co-efficient is calculated using the mathematical relation,

$$T_\sigma(E) = Tr[\Gamma_R^\sigma(E)G_R^\sigma(E)\Gamma_L^\sigma(E)G_R^{\sigma\dagger}(E)] \quad (6.1)$$

The level broadening due to the coupling between left(L) (right(R)) electrode and the central scattering region is represented here using  $\Gamma_{L,R}^\sigma(E) = (\Sigma_{L,R}^\sigma(E) - \Sigma_{L,R}^{\sigma\dagger}(E))$ .  $\Sigma_{L,R}^\sigma(E)$  corresponds to the retarded self-energy associated with this coupling.  $G_R^\sigma = (ES - H^\sigma - \Sigma_L^\sigma - \Sigma_R^\sigma)^{-1}$  represents the retarded Green's function. The Hamiltonian and the overlap matrix are represented by H and S respectively.

The spin-polarized current,  $I_{\uparrow(\downarrow)}$  through the device was calculated by using Landauer-Büttiker formula

$$I_{\uparrow(\downarrow)} = \frac{e}{h} \int_{-\infty}^{\infty} T_{\uparrow(\downarrow)}(E, V_b)[F(E - \mu_L) - F(E - \mu_R)]dE \quad (6.2)$$

Where  $F(E)$  is the Fermi Dirac distribution for an energy level  $E$  under the bias voltage  $V_b$ . The bias window is kept from  $-V_b/2$  to  $V_b/2$ .

Spin injection efficiency (SIE) is calculated from the output current using the

relation,

$$SIE = \frac{I_{\uparrow} - I_{\downarrow}}{I_{\uparrow} + I_{\downarrow}} \quad (6.3)$$

Here  $I_{\uparrow}$  and  $I_{\downarrow}$  represent spin-up current and spin-down current respectively.

Magnetoresistance (MR) is estimated using the relation,

$$MR = \frac{I_{PC} - I_{APC}}{I_{APC}} \quad (6.4)$$

The total current through parallel configuration and anti-parallel configuration are represented by  $I_{PC}$  and  $I_{APC}$  respectively.

## 6.3 Results and Discussions

### 6.3.1 Spin Transport through Co/trilayer $\text{CrI}_3$ /Co Magnetic Junctions

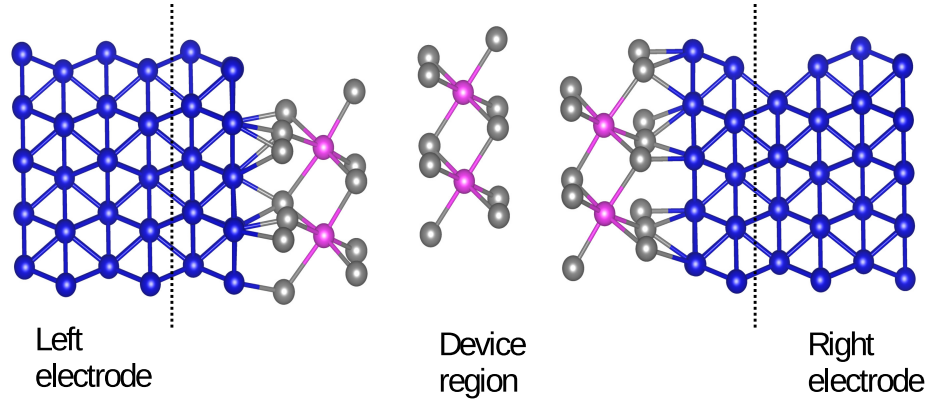


Fig. 6.1: Schematic representation of Co/trilayer  $\text{CrI}_3$ /Co magnetic junction. Blue, pink and grey solid spheres represent Co, Cr and I atoms respectively.

A magnetic junction is composed using a ferromagnetic semiconductor material,  $\text{CrI}_3$ . The electrode regions are made of semi-infinite Co-leads. Three layers of  $\text{CrI}_3$  along with few layers of Co has been considered in the device region (Fig. 6.1). To start with, the spin-dependent transmission spectrum is calculated in the absence of external bias. The obtained equilibrium transmission spectrum shown in the Fig. 6.2 indicates a substantial difference in the transmission through different spin channels. This motivates us to further investigate the spin-transport behaviour through this magnetic junction in the presence of external biases.

The external bias is systematically increased from 0.2 to 1 V, and calculated

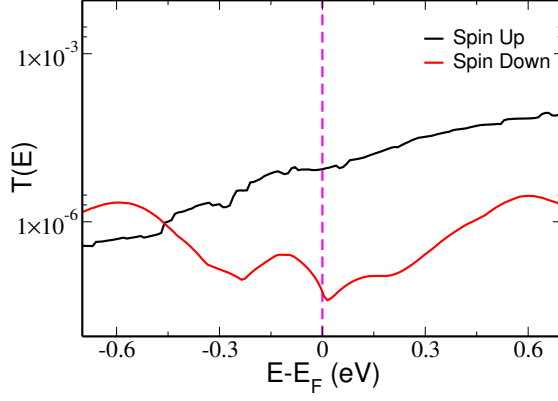


Fig. 6.2: Transmission spectrum at the equilibrium condition for Co/trilayer CrI<sub>3</sub>/Co magnetic junction. Black and red curves represent current through spin-up and spin-down channels respectively.

spin-resolved transmission and current-voltage characteristics when electrodes are in both parallel and anti-parallel magnetic configurations. The calculated transmission spectra as shown in Fig. 6.3 (a) indicate high spin-selective transmission near Fermi level in all cases. A large difference in the transmission through different spin-channel is observed at higher applied bias. The change in the relative magnetic orientation of electrodes (from parallel to anti-parallel configuration) also shows a significant impact on the transmission behaviour. In the parallel configuration, the difference between spin-up transmission and spin-down transmission at the Fermi level decreases with an increase in the applied bias. However, the trend is different in the case of anti-parallel configuration. There, the increase in applied bias elevates the difference between transmission through both spin channels at the Fermi level.

Next, the spin-resolved current-voltage characteristics were calculated and shown in Fig. 6.3(b). Parallel configuration is favorable for the spin-up current transmission. Note that in this configuration, a negligibly small spin-down current is passing through Co/trilayer CrI<sub>3</sub>/Co magnetic junction at the lower bias region. As the voltage increases, a slight increase in the spin-down current is observed. Calculation shows that a comparatively large minority-spin current is passing through the junction in the anti-parallel configuration. However, the difference between the current through both spin channels is less compared to the parallel configuration.

Spin injection efficiency (SIE) is the parameter which can provide quantitative information about the spin-polarized transport through the magnetic junction. SIE is calculated from the output current using the formula, 6.3 and is plotted in Fig. 6.3(c). SIE is very high for the magnetic junction in the parallel configuration. At a lower bias, SIE is more than 0.95. That means, more than 95 % of the total

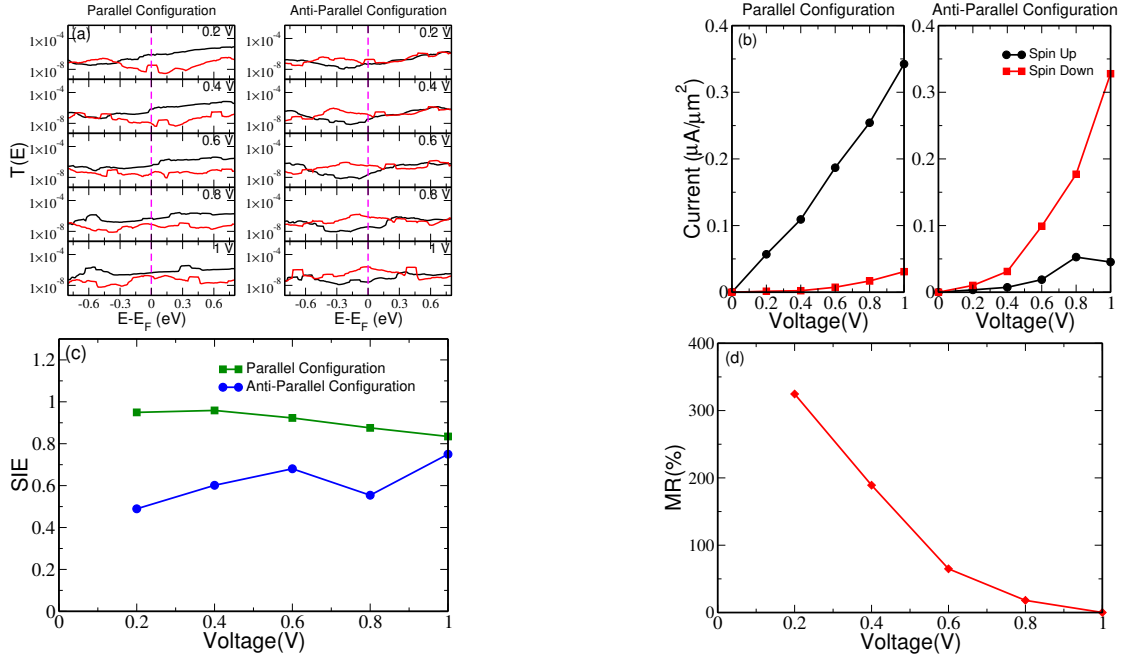


Fig. 6.3: (a) Spin-polarised transmission spectrum, (b) spin-polarized current-voltage characteristics, (c) spin injection efficiency (SIE) and (d) magnetoresistance (MR) of Co/trilayer CrI<sub>3</sub>/Co magnetic junction

current passes through a spin channel, and here it is a spin-up channel. SIE is also very high in the anti-parallel configuration when the applied bias voltage is 1 V.

The SIE values indicate that Co/trilayer CrI<sub>3</sub>/Co would be very suitable for obtaining highly spin-polarized current if the magnetic junction is kept in the parallel magnetic configuration at lower bias voltage. High SIE obtained here is mainly due to the presence of ferromagnetic material, CrI<sub>3</sub>. The potential of ferromagnetic semiconductor, CrI<sub>3</sub> to develop a highly spin-polarized current has already been discussed in the previous chapter. The calculated transport results validate the assumptions put forward based on the detailed electronic structure study on CrI<sub>3</sub>.

Another important device parameter, the magnetoresistance is also calculated for Co/trilayer CrI<sub>3</sub>/Co magnetic junction and shown in Fig. 6.3 (d). The magnetic junction exhibits a very high MR at lower bias voltage which eventually goes down with an increase in the applied bias. At 0.2 V, MR is 325 %, which is a good value for the spintronic device application.

On the basis of detailed electronic structure study, and transport calculation one can conclude that Co/trilayer CrI<sub>3</sub>/Co magnetic junction would be a very suitable spin-transport device capable of working at lower bias voltages.



### 6.3.2 Spin Transport through Co/CrI<sub>3</sub>/TMDC/CrI<sub>3</sub>/Co Magnetic Junctions

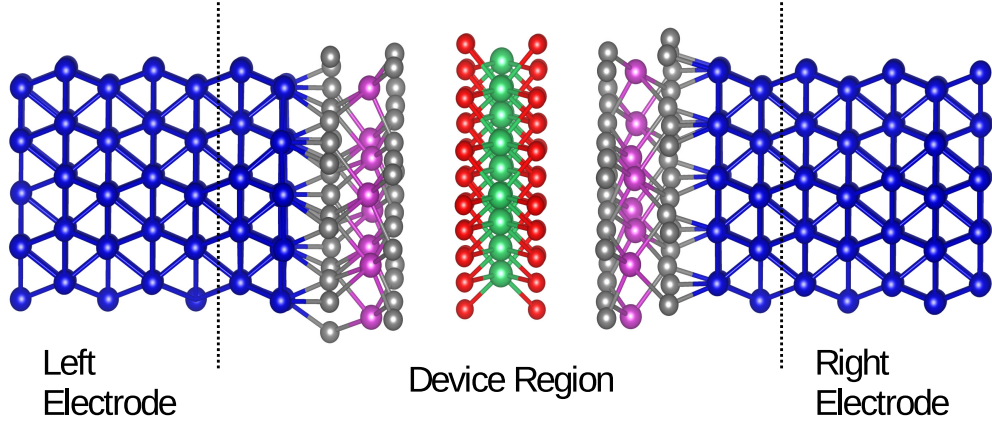


Fig. 6.4: Schematic representation of Co/CrI<sub>3</sub>/TMDC/CrI<sub>3</sub>/Co magnetic junction. Blue, pink and grey solid spheres represent Co, Cr and I atoms respectively. Green and red solid spheres represent atoms in the TMDC monolayer. Green spheres can be Mo or W and red spheres can be S or Se atoms.

At the final stage of my research, I have modelled another set of magnetic junctions combining CrI<sub>3</sub> and TMDC monolayers as transport layers along with semi-infinite Co-lead and studied the spin-transport behaviour through these junctions. Fig. 6.4 shows the schematic representation of Co/CrI<sub>3</sub>/TMDC/CrI<sub>3</sub>/Co magnetic junction in which monolayer of a TMDC material was sandwich between two CrI<sub>3</sub> mono-layers which is further connected to the semi-infinite Co-leads. Here, blue, pink, and grey solid spheres represent Co, Cr, and I atoms respectively. Green and red solid spheres represent atoms in the TMDC monolayer. Spin-resolved transmission spectrum, spin-current-voltage characteristics, spin injection efficiency (SIE) and magnetoresistance (MR) are calculated for Co/CrI<sub>3</sub>/TMDC/CrI<sub>3</sub>/Co magnetic junctions by considering MoS<sub>2</sub>, MoSe<sub>2</sub>, WS<sub>2</sub>, and WSe<sub>2</sub> as TMDC materials. These investigations are also carried out in the presence of an applied bias, ranging from 0.2 V to 1 V in both parallel and anti-parallel configurations. In this series of studies, the Co/CrI<sub>3</sub>/MoS<sub>2</sub>/CrI<sub>3</sub>/Co magnetic junction has been considered first. A spin-sensitive transmission spectrum is obtained in both parallel and anti-parallel magnetic configurations and shown in Fig. 6.5 (a). Calculation shows that the nature of the transmission spectrum differs significantly with the change in the relative magnetic configuration of electrodes. In the parallel configuration, transmission through the spin-up channel is more, whereas transmission through the spin-down channel is more at the anti-parallel configuration. The obtained spin-resolved current-voltage characteristics shown in Fig. 6.5(b) are also consistent with the calculated transmission spectrum. The Co/CrI<sub>3</sub>/MoS<sub>2</sub>/CrI<sub>3</sub>/Co

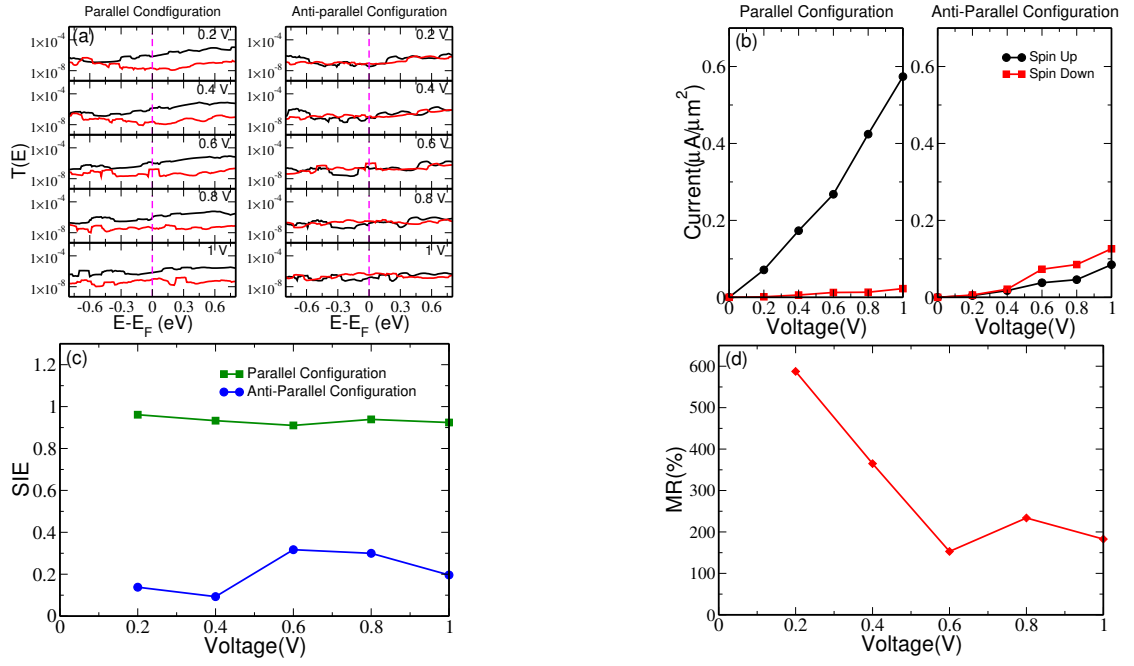


Fig. 6.5: (a) Spin-polarised transmission spectrum, (b) spin-polarized current-voltage characteristics, (c) spin injection efficiency (SIE) and (d) magnetoresistance (MR) of Co/CrI<sub>3</sub>/MoS<sub>2</sub>/CrI<sub>3</sub>/Co magnetic junction.)

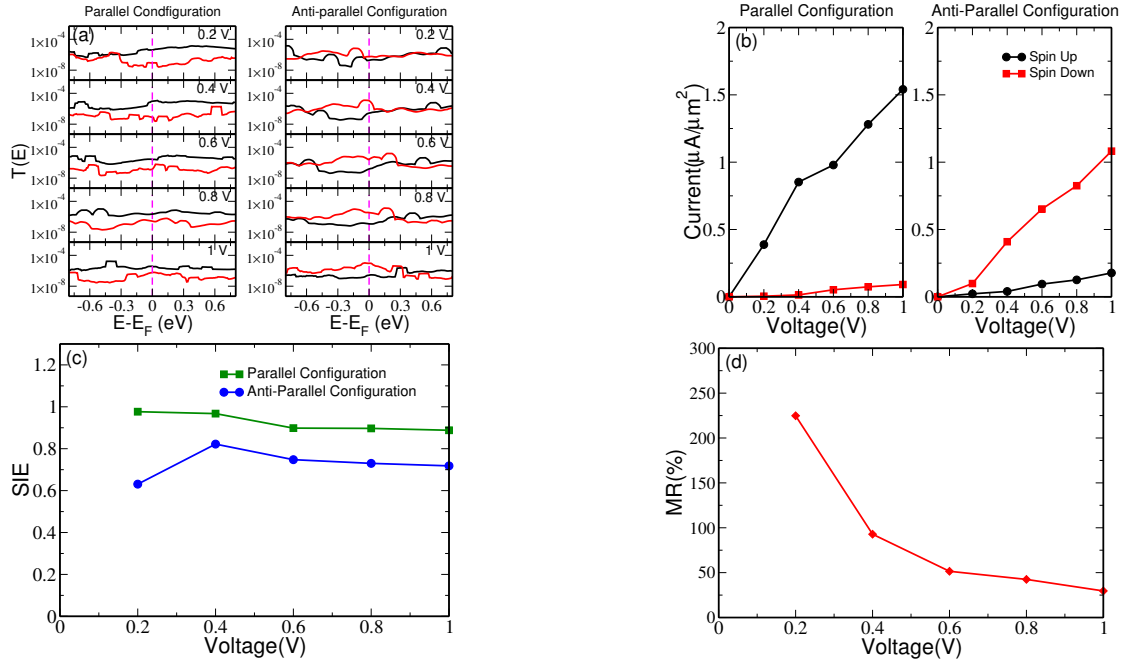


Fig. 6.6: (a) Spin-polarised transmission spectrum, (b) spin-polarized current-voltage characteristics, (c) spin injection efficiency (SIE) and (d) magnetoresistance (MR) of Co/CrI<sub>3</sub>/MoSe<sub>2</sub>/CrI<sub>3</sub>/Co magnetic junction.

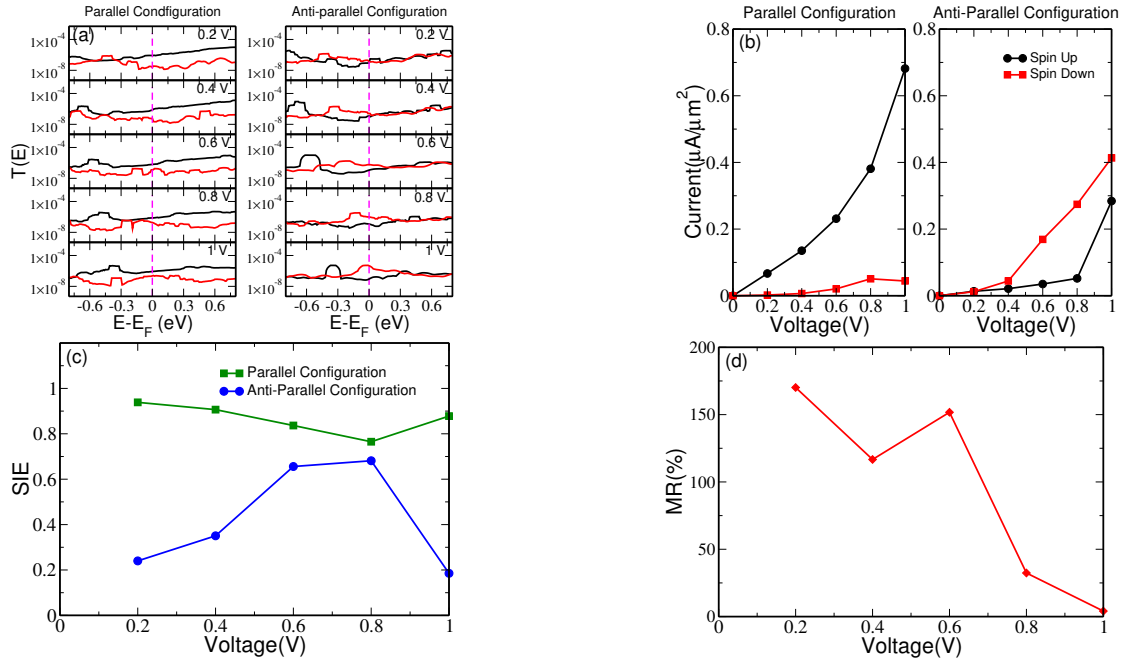


Fig. 6.7: (a) Spin-polarised transmission spectrum, (b) spin-polarized current-voltage characteristics, (c) spin injection efficiency (SIE) and (d) magnetoresistance (MR) of Co/CrI<sub>3</sub>/WS<sub>2</sub>/CrI<sub>3</sub>/Co magnetic junction.

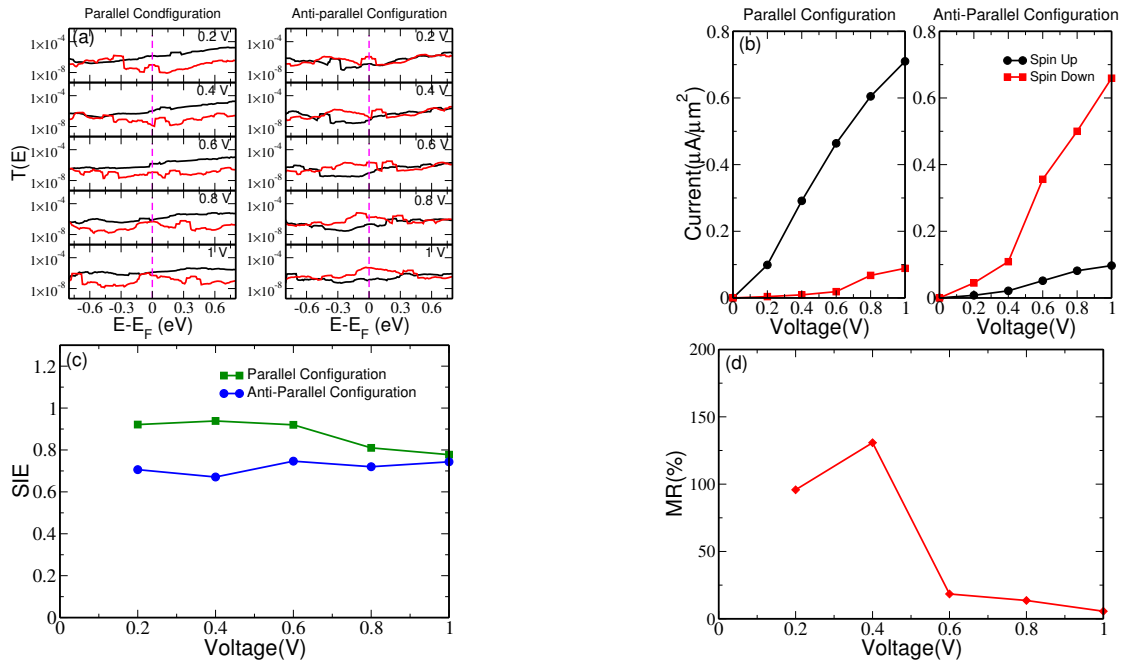


Fig. 6.8: (a) Spin-polarised transmission spectrum, (b) spin-polarized current-voltage characteristics, (c) spin injection efficiency (SIE) and (d) magnetoresistance (MR) of Co/CrI<sub>3</sub>/WSe<sub>2</sub>/CrI<sub>3</sub>/Co magnetic junction.

magnetic junction transmits a large amount of current through the spin-up channel when it is in the parallel configuration. Nevertheless, the spin-up current is found to be drastically reduced when the relative magnetic configuration of electrodes becomes anti-parallel. The spin-down current was also found to be more than the spin-up current in this configuration. Even though parallel and anti-parallel configurations give spin-polarized current-voltage characteristics, the difference between spin-up current and spin-down current varies in both magnetic configurations. The difference between the current through two spin channels is much greater in the parallel configuration than in the anti-parallel configuration.

The SIE calculated for Co/CrI<sub>3</sub>/MoS<sub>2</sub>/CrI<sub>3</sub>/Co magnetic junction is shown in Fig. 6.5 (c). Parallel configuration shows reasonably high SIE (> 90%) in all the applied bias range. Spin filtering at the CrI<sub>3</sub>/MoS<sub>2</sub> interface is mainly responsible for the very high SIE in the Co/CrI<sub>3</sub>/MoS<sub>2</sub>/CrI<sub>3</sub>/Co magnetic junction. The magnetoresistance of the junction at various applied bias voltages are also estimated. A high MR of 590 % is obtained at 0.2 V. MR goes down at higher bias voltages.

Similar calculations are carried out for Co/CrI<sub>3</sub>/MoSe<sub>2</sub>/CrI<sub>3</sub>/Co, Co/CrI<sub>3</sub>/WS<sub>2</sub>/CrI<sub>3</sub>/Co, and Co/CrI<sub>3</sub>/WSe<sub>2</sub>/CrI<sub>3</sub>/Co magnetic junctions (Fig. 6.6-6.8). Spin-polarized transmission spectrum and current-voltage characteristics are obtained in all these cases. Similar to Co/CrI<sub>3</sub>/MoS<sub>2</sub>/CrI<sub>3</sub>/Co magnetic junction, these magnetic junctions also transmit a large amount of spin-up current in the parallel configuration. The large difference between spin-up and spin-down current in the parallel configuration is mainly due to the high spin injection efficiency at the interface. Interestingly, in all these structure SIE is found to be more at lower bias voltage. The SIE obtained here is much greater than the SIE for Co/MoS<sub>2</sub>/graphene/MoS<sub>2</sub>/Co magnetic junction discussed in the chapter 4. Excellent spin filtering occurs due to the presence of monolayer CrI<sub>3</sub> at the interface is responsible for high SIE obtained in the magnetic junctions. The MR is also estimated for the other magnetic junctions. Among four hetero-junctions Co/CrI<sub>3</sub>/TMDC/CrI<sub>3</sub>/Co magnetic junctions, Co/CrI<sub>3</sub>/MoS<sub>2</sub>/CrI<sub>3</sub>/Co magnetic junction provides maximum MR. It is observed that MR values go down at higher bias voltages in all these magnetic junctions. Compared to other magnetic junctions, MR at higher bias is more in Co/CrI<sub>3</sub>/MoS<sub>2</sub>/CrI<sub>3</sub>/Co magnetic junction, even though it is much less than the MR at lower bias voltage.

Transport study carried out on Co/CrI<sub>3</sub>/TMDC/CrI<sub>3</sub>/Co magnetic junctions validates the assumptions of monolayer CrX<sub>3</sub> and CrX<sub>3</sub>/TMDC heterostructure studies discussed in chapter 5. Monolayer CrX<sub>3</sub> provides spin filter effects, and due to the presence of spin-dependent Schottky barrier height for electrons in the

CrX<sub>3</sub>/TMDC interface, a high spin-polarized current is developed in the magnetic junctions. Our study reveals that the spin transport properties and MR can be significantly enhanced by using Van-der Waal magnetic hetero-junctions based on a combination of CrX<sub>3</sub> and TMDC materials.

## 6.4 Conclusion

To conclude, in this study I have carried out a detailed investigation of spin transport through magnetic junctions composed of van-der Waal heterostructures made of 2D ferromagnetic material, CrI<sub>3</sub> and TMDC compounds, using the combination of DFT and NEGF methods. Co serves as the electrode material in all the magnetic junctions. The presence of ferromagnetic semiconductor material (CrI<sub>3</sub>) with large band edge energy difference, helped to obtain high spin-polarized current in all these junctions. These magnetic junctions show a very high SIE at low applied bias voltages. Apart from high SIE, high MR is also obtained at lower bias voltages. This study proposes that the magnetic junctions composed of the CrI<sub>3</sub> compound have the potential to act as an efficient spintronic device. Varying the TMDC material in the device region offers the possibility of tuning device parameters.

# Chapter 7

## Summary and Future Work

### 7.1 Summary

To summarize this thesis work, the electronic structures of different 2D materials are investigated using first-principle calculations based on the density functional theory. The aim was to study the suitability of using 2D materials in transport devices. To start with, detailed electronic band structures of different TMDC materials are carefully investigated in their low dimensional form. Calculation shows that, in each TMDC, few layers (up to three layers) of the compound remain under the strong quantum confinement regime. Therefore, the compound's electronic behaviour and the nature of transport through it can be tuned efficiently employing proper methods. Aiming to study the spin-transport through these compounds, Co-TMDC interfaces are modelled and the interface electronic structure and magnetic properties are carefully investigated. The calculation reveals a noticeable change in that the electronic structures and magnetic behaviour of layered TMDC materials while it is in contact with Co surface. Their Schottky barrier height also decreases in this heterostructure. The Co/monolayer TMDC interface introduces a spin-polarized state near the Fermi energy, which effectively acts as a spin filter. The study also shows the potential use of Co as an efficient spin injector to the 2D TMDC materials.

Next, the spin transport through various magnetic junctions composed of monolayers, trilayers, and heterostructures of TMDC materials are studied. A combination of the density functional theory and non-equilibrium Green's function methods is used for this purpose. The results obtained from the detailed investigation of the electronic structure of the Co/TMDC interface and magnetic tri-junctions helped explain the transport behaviour of magnetic junctions com-

posed of Co and TMDC materials. Co/TMDC interface has a vital role in determining the transport properties of the magnetic junctions. It is observed that the spin-polarized state near the Fermi energy in the Co/MoS<sub>2</sub> interface effectively acts as a spin filter and enhances the spin injection efficiency of the system.

Spin-transmission spectrum and spin-polarized current are calculated for the magnetic junctions at various applied bias voltages in the parallel and anti-parallel electrodes magnetic configurations. The effect on the transport properties due to the change in the applied bias as well as the change in the relative magnetic configuration of electrodes has been investigated. At a different applied bias situation, the magnetoresistance of all magnetic junctions is estimated. The study showed that MR could be tuned by varying the number of layers and type of layers in the device region and also by varying applied bias. A giant MR value of 1270% is estimated in the Co/MoS<sub>2</sub>/graphene/MoS<sub>2</sub>/Co magnetic junction at an external bias of 1 V. A high MR value along with the device parameters indicates that this heterojunction would be ideal for practical applications in the future. This study prescribes how the magneto-electric properties can be further tuned by changing the number of layers as well as the layer type. Also, the results obtained in this study promote the use of layers of metal dichalcogenides for spin-valve devices.

Newly synthesized 2D ferromagnetic materials are also considered, to study their possible use in spin-transport devices. High band edge energy difference in monolayer CrX<sub>3</sub> materials show that these materials are capable of producing robust spin filtering, which is very suitable for spintronic applications. Detailed electronic structure calculations are carried out in CrX<sub>3</sub>/TMDC van der Waals heterostructures. The study reveals that a stable interface between CrX<sub>3</sub> and TMDC layers can be achieved. Although the interface properties can be effectively tuned by varying the materials, the interlayer interaction present at the interface does not significantly alter the electronic and magnetic properties of CrX<sub>3</sub>. A substantial spin-dependent Schottky barrier was estimated in CrX<sub>3</sub>/TMDC heterostructure. Also, the complex magnetic interface in this heterostructure may act as an efficient spin filter for the tunnel barrier.

Spin transport studies are conducted on magnetic junctions of trilayer CrX<sub>3</sub>s and CrI<sub>3</sub>/TMDC/CrI<sub>3</sub> multilayers. Highly spin-polarized current and large magnetoresistance obtained from the magnetic junctions composed of CrI<sub>3</sub> validates the assumptions put forward based on electronic structure study carried out in CrI<sub>3</sub> and CrX<sub>3</sub>/TMDC heterostructures. The device parameters calculated for magnetic junctions composed of CrX<sub>3</sub> show a high potential of using these magnetic junctions in future efficient spintronic devices.

The highlights of the entire research can be summarized as follows

- This study provided a basic understanding of the spin transport phenomenon in low-dimensional materials.
- The electronic structure of 2D materials and their interface with metal are studied in detail and investigated the potential of spin injection.
- Different spin transport devices are modelled using various 2D materials and their heterostructures and studied spin transport through them in detail.
- Suggested different ways to tune the spintronic device parameters.
- This thesis proposes various magnetic junctions composed of materials with very high magnetoresistance and have high spin selectivity. These could be suitable for highly efficient device applications in the future.

## 7.2 Scope of Future Work

Finding suitable materials for spin transport and tuning transport properties lead to advanced spintronics devices. This research investigated the potential of spin transport in various 2D materials, calculated spin transport through various magnetic junctions, and proposed ways to tune spin transport properties. However, more research in this direction can provide more suitable materials for spin transport with improved properties. The effect of spin-orbit coupling is not included in the spin transport calculations in this research, which is one of the drawbacks. So more in-depth investigation of spin transport is possible by incorporating other spin interaction effects like spin-orbit coupling in the calculations. Realizing the potential and possibilities and understanding the drawbacks of this research, there are many scopes for further research on this topic as listed here.

- This study indicates that 2D chromium tri-halides could be well suited for spintronic applications. Since these materials are designed very recently, only a few reports are available for this class of materials. Therefore, a more detailed investigation of these materials and their heterostructures may provide the pathway for designing excellent spin transport devices.
- It is very essential to develop a computationally viable method to calculate spin transport by incorporating spin-orbit coupling, which can provide more detail and quantitative information for advanced MTJs.



- Finally, a detailed investigation of spin-transfer torque in magnetic junctions composed of 2D materials could provide many interesting phenomena associated with spin-transport. An in-depth investigation is also required in this area to understand how this can be utilized to improve spin transport properties.

# References

- Aadhityan, A., Kala, C. P., and Thiruvadigal, D. J. (2018). First principle study on tnr effect in a-mgo-a (a= fe, co and ni) magnetic tunnel junction. *Applied Surface Science*, 449:799–804.
- Acun, A., Zhang, L., Bampoulis, P., Farmanbar, M. v., van Houselt, A., Rudenko, A., Lingenfelder, M., Brocks, G., Poelsema, B., Katsnelson, M., et al. (2015). Germanene: the germanium analogue of graphene. *Journal of physics: Condensed matter*, 27(44):443002.
- Allain, A., Kang, J., Banerjee, K., and Kis, A. (2015). Electrical contacts to two-dimensional semiconductors. *Nature materials*, 14(12):1195–1205.
- Andrei, E. Y., Li, G., and Du, X. (2012). Electronic properties of graphene: a perspective from scanning tunneling microscopy and magnetotransport. *Reports on Progress in Physics*, 75(5):056501.
- Bai, J., Cheng, R., Xiu, F., Liao, L., Wang, M., Shailos, A., Wang, K. L., Huang, Y., and Duan, X. (2010). Very large magnetoresistance in graphene nanoribbons. *Nature nanotechnology*, 5(9):655–659.
- Becke, A. D. (1993). A new mixing of hartree-fock and local density-functional theories. *The Journal of chemical physics*, 98(2):1372–1377.
- Blum, V., Gehrke, R., Hanke, F., Havu, P., Havu, V., Ren, X., Reuter, K., and Scheffler, M. (2009). Ab initio molecular simulations with numeric atom-centered orbitals. *Computer Physics Communications*, 180(11):2175–2196.
- Bowen, M., Cros, V., Petroff, F., Fert, A., Martinez Boubeta, C., Costa-Krämer, J. L., Anguita, J. V., Cebollada, A., Briones, F., De Teresa, J., et al. (2001). Large magnetoresistance in fe/mgo/feco (001) epitaxial tunnel junctions on gaas (001). *Applied Physics Letters*, 79(11):1655–1657.
- Brandbyge, M., Mozos, J.-L., Ordejón, P., Taylor, J., and Stokbro, K. (2002). Density-functional method for nonequilibrium electron transport. *Physical Review B*, 65(16):165401.

- Büttiker, M. (1986). Role of quantum coherence in series resistors. *Physical Review B*, 33(5):3020.
- Chakraverty, M. and Harisankar, P. (2018). Demonstration of bias dependence of tunnel magnetoresistance in co-mgo-co magnetic tunnel junctions using first principles calculations. In *2018 4th International Conference on Devices, Circuits and Systems (ICDCS)*, pages 130–136. IEEE.
- Chakraverty, M., Kittur, H. M., and Kumar, P. A. (2013). First principle simulations of various magnetic tunnel junctions for applications in magnetoresistive random access memories. *IEEE Transactions on nanotechnology*, 12(6):971–977.
- Chen, M., Yu, Z., Wang, Y., Xie, Y., Wang, J., and Guo, H. (2016). Nonequilibrium spin injection in monolayer black phosphorus. *Physical Chemistry Chemical Physics*, 18(3):1601–1606.
- Chopra, K. N. (2019). *Spintronics Theoretical Analysis and Designing of Devices Based on Giant Magneto resistance*. DESIDOC.
- Clark, S. J., Segall, M. D., Pickard, C. J., Hasnip, P. J., Probert, M. I., Refson, K., and Payne, M. C. (2005). First principles methods using castep. *Zeitschrift für Kristallographie-Crystalline Materials*, 220(5-6):567–570.
- Clemmer, A. and Davies, S. (2011). Smeagol: a “specific-to-general” semantic web query interface paradigm for novices. In *International Conference on Database and Expert Systems Applications*, pages 288–302. Springer.
- Cobas, E., Friedman, A. L., van’t Erve, O. M., Robinson, J. T., and Jonker, B. T. (2012). Graphene as a tunnel barrier: graphene-based magnetic tunnel junctions. *Nano letters*, 12(6):3000–3004.
- Dankert, A., Kamalakar, M. V., Wajid, A., Patel, R. S., and Dash, S. P. (2015). Tunnel magnetoresistance with atomically thin two-dimensional hexagonal boron nitride barriers. *Nano Research*, 8(4):1357–1364.
- Dieny, B., Prejbeanu, I. L., Garello, K., Gambardella, P., Freitas, P., Lehndorff, R., Raberg, W., Ebels, U., Demokritov, S. O., Akerman, J., et al. (2020). Opportunities and challenges for spintronics in the microelectronics industry. *Nature Electronics*, 3(8):446–459.
- Dolui, K., Narayan, A., Rungger, I., and Sanvito, S. (2014). Efficient spin injection and giant magnetoresistance in fe/mos 2/fe junctions. *Physical Review B*, 90(4):041401.

- Frey, N. C., Bandyopadhyay, A., Kumar, H., Anasori, B., Gogotsi, Y., and Shenoy, V. B. (2019). Surface-engineered mxenes: electric field control of magnetism and enhanced magnetic anisotropy. *ACS nano*, 13(3):2831–2839.
- Friedman, A. L., Tedesco, J. L., Campbell, P. M., Culbertson, J. C., Aifer, E., Perkins, F. K., Myers-Ward, R. L., Hite, J. K., Eddy Jr, C. R., Jernigan, G. G., et al. (2010). Quantum linear magnetoresistance in multilayer epitaxial graphene. *Nano letters*, 10(10):3962–3965.
- Giannozzi, P., Andreussi, O., Brumme, T., Bunau, O., Nardelli, M. B., Calandra, M., Car, R., Cavazzoni, C., Ceresoli, D., Cococcioni, M., et al. (2017). Advanced capabilities for materials modelling with quantum espresso. *Journal of physics: Condensed matter*, 29(46):465901.
- Gómez-Navarro, C., Burghard, M., and Kern, K. (2008). Elastic properties of chemically derived single graphene sheets. *Nano letters*, 8(7):2045–2049.
- Gong, C., Li, L., Li, Z., Ji, H., Stern, A., Xia, Y., Cao, T., Bao, W., Wang, C., Wang, Y., et al. (2017). Discovery of intrinsic ferromagnetism in two-dimensional van der waals crystals. *Nature*, 546(7657):265–269.
- Gonze, X., Jollet, F., Araujo, F. A., Adams, D., Amadon, B., Applencourt, T., Audouze, C., Beuken, J.-M., Bieder, J., Bokhanchuk, A., et al. (2016). Recent developments in the abinit software package. *Computer Physics Communications*, 205:106–131.
- Grimme, S., Antony, J., Ehrlich, S., and Krieg, H. (2010). A consistent and accurate ab initio parametrization of density functional dispersion correction (dft-d) for the 94 elements h-pu. *The Journal of chemical physics*, 132(15):154104.
- Grimme, S., Ehrlich, S., and Goerigk, L. (2011). Effect of the damping function in dispersion corrected density functional theory. *Journal of computational chemistry*, 32(7):1456–1465.
- Gygi, F. (2008). Architecture of qbox: A scalable first-principles molecular dynamics code. *IBM Journal of Research and Development*, 52(1.2):137–144.
- Heyd, J., Scuseria, G. E., and Ernzerhof, M. (2003). Hybrid functionals based on a screened coulomb potential. *The Journal of chemical physics*, 118(18):8207–8215.
- Hirohata, A., Yamada, K., Nakatani, Y., Prejbeanu, I.-L., Diény, B., Pirro, P., and Hillebrands, B. (2020). Review on spintronics: Principles and device applications. *Journal of Magnetism and Magnetic Materials*, 509:166711.

- Hohenberg, P. and Kohn, W. (1964). Inhomogeneous electron gas. *Physical review*, 136(3B):B864.
- Hu, J.-Q., Shi, X.-H., Wu, S.-Q., Ho, K.-M., and Zhu, Z.-Z. (2019). Dependence of electronic and optical properties of mos 2 multilayers on the interlayer coupling and van hove singularity. *Nanoscale research letters*, 14(1):1–13.
- Huang, B., Clark, G., Klein, D. R., MacNeill, D., Navarro-Moratalla, E., Seyler, K. L., Wilson, N., McGuire, M. A., Cobden, D. H., Xiao, D., et al. (2018). Electrical control of 2d magnetism in bilayer cri 3. *Nature nanotechnology*, 13(7):544–548.
- Huang, B., Clark, G., Navarro-Moratalla, E., Klein, D. R., Cheng, R., Seyler, K. L., Zhong, D., Schmidgall, E., McGuire, M. A., Cobden, D. H., et al. (2017). Layer-dependent ferromagnetism in a van der waals crystal down to the monolayer limit. *Nature*, 546(7657):270–273.
- Huertas-Hernando, D., Guinea, F., and Brataas, A. (2007). Spin relaxation times in disordered graphene. *The European Physical Journal Special Topics*, 148(1):177–181.
- Iqbal, M. Z., Qureshi, N. A., and Hussain, G. (2018). Recent advancements in 2d-materials interface based magnetic junctions for spintronics. *Journal of Magnetism and Magnetic Materials*, 457:110–125.
- Jiang, S., Li, L., Wang, Z., Mak, K. F., and Shan, J. (2018a). Controlling magnetism in 2d cri 3 by electrostatic doping. *Nature nanotechnology*, 13(7):549–553.
- Jiang, S., Shan, J., and Mak, K. F. (2018b). Electric-field switching of two-dimensional van der waals magnets. *Nature materials*, 17(5):406–410.
- Jin, H., Li, J., Wan, L., Dai, Y., Wei, Y., and Guo, H. (2017). Ohmic contact in monolayer inse-metal interface. *2D Materials*, 4(2):025116.
- Julliere, M. (1975). Tunneling between ferromagnetic films. *Physics letters A*, 54(3):225–226.
- Kamaruddin, K. (2016). Graphene and nanotechnology applications for space technology. In *Space Environment and Kibo Utilization Workshop (SEKUW)*, April.
- Kang, J., Liu, W., Sarkar, D., Jena, D., and Banerjee, K. (2014). Computational study of metal contacts to monolayer transition-metal dichalcogenide semiconductors. *Physical Review X*, 4(3):031005.

- Kim, H. H., Yang, B., Patel, T., Sfigakis, F., Li, C., Tian, S., Lei, H., and Tsen, A. W. (2018). One million percent tunnel magnetoresistance in a magnetic van der waals heterostructure. *Nano letters*, 18(8):4885–4890.
- Kim, H. H., Yang, B., Tian, S., Li, C., Miao, G.-X., Lei, H., and Tsen, A. W. (2019). Tailored tunnel magnetoresistance response in three ultrathin chromium trihalides. *Nano letters*, 19(8):5739–5745.
- Kim, W. Y. and Kim, K. S. (2008). Prediction of very large values of magnetoresistance in a graphene nanoribbon device. *Nature nanotechnology*, 3(7):408–412.
- Klein, D. R., MacNeill, D., Lado, J. L., Soriano, D., Navarro-Moratalla, E., Watanabe, K., Taniguchi, T., Manni, S., Canfield, P., Fernández-Rossier, J., et al. (2018). Probing magnetism in 2d van der waals crystalline insulators via electron tunneling. *Science*, 360(6394):1218–1222.
- Kohn, W. and Sham, L. J. (1965). Self-consistent equations including exchange and correlation effects. *Physical review*, 140(4A):A1133.
- Kresse, G. and Furthmüller, J. (1996). Efficient iterative schemes for ab initio total-energy calculations using a plane-wave basis set. *Physical Review B - Condensed Matter and Materials Physics*, 54(16):11169–11186.
- Kresse, G. and Furthmüller, J. (1996). Efficient iterative schemes for ab initio total-energy calculations using a plane-wave basis set. *Physical review B*, 54(16):11169.
- Kuklin, A. V., Kuzubov, A. A., Kovaleva, E. A., Mikhaleva, N. S., Tomilin, F. N., Lee, H., and Avramov, P. V. (2017). Two-dimensional hexagonal crn with promising magnetic and optical properties: A theoretical prediction. *Nanoscale*, 9(2):621–630.
- Kuklin, A. V., Shostak, S. A., and Kuzubov, A. A. (2018). Two-dimensional lattices of vn: Emergence of ferromagnetism and half-metallicity on nanoscale. *The journal of physical chemistry letters*, 9(6):1422–1428.
- Kumar, H., Frey, N. C., Dong, L., Anasori, B., Gogotsi, Y., and Shenoy, V. B. (2017). Tunable magnetism and transport properties in nitride mxenes. *ACS nano*, 11(8):7648–7655.
- Lee, C., Wei, X., Kysar, J. W., and Hone, J. (2008). Measurement of the elastic properties and intrinsic strength of monolayer graphene. *science*, 321(5887):385–388.

- Lee, C., Yang, W., and Parr, R. G. (1988). Development of the colle-salvetti correlation-energy formula into a functional of the electron density. *Physical review B*, 37(2):785.
- Lee, Y.-H., Zhang, X.-Q., Zhang, W., Chang, M.-T., Lin, C.-T., Chang, K.-D., Yu, Y.-C., Wang, J. T.-W., Chang, C.-S., Li, L.-J., et al. (2012). Synthesis of large-area mos2 atomic layers with chemical vapor deposition. *Advanced materials*, 24(17):2320–2325.
- Li, H., Xu, Y.-K., Cheng, Z.-P., He, B.-G., and Zhang, W.-B. (2020). Spin-dependent schottky barriers and vacancy-induced spin-selective ohmic contacts in magnetic vdw heterostructures. *Physical Chemistry Chemical Physics*, 22(17):9460–9466.
- Li, X., Wu, X., and Yang, J. (2014). Half-metallicity in mnpse3 exfoliated nanosheet with carrier doping. *Journal of the American Chemical Society*, 136(31):11065–11069.
- Liao, Z.-M., Wu, H.-C., Kumar, S., Duesberg, G. S., Zhou, Y.-B., Cross, G. L., Shvets, I. V., and Yu, D.-P. (2012). Large magnetoresistance in few layer graphene stacks with current perpendicular to plane geometry. *Advanced Materials*, 24(14):1862–1866.
- Lin, L., Lu, J., and Ying, L. (2019). Numerical methods for kohn–sham density functional theory. *Acta Numerica*, 28:405–539.
- Liu, J., Sun, Q., Kawazoe, Y., and Jena, P. (2016). Exfoliating biocompatible ferromagnetic cr-trihalide monolayers. *Physical Chemistry Chemical Physics*, 18(13):8777–8784.
- Mak, K. F., Lee, C., Hone, J., Shan, J., and Heinz, T. F. (2010). Atomically Thin MoS: A New Direct-Gap Semiconductor. *Physical Review Letters*, 105(13):136805.
- Mannix, A. J., Zhou, X.-F., Kiraly, B., Wood, J. D., Alducin, D., Myers, B. D., Liu, X., Fisher, B. L., Santiago, U., Guest, J. R., et al. (2015). Synthesis of borophenes: Anisotropic, two-dimensional boron polymorphs. *Science*, 350(6267):1513–1516.
- Manzeli, S., Ovchinnikov, D., Pasquier, D., Yazyev, O. V., and Kis, A. (2017). 2d transition metal dichalcogenides. *Nature Reviews Materials*, 2(8):17033.
- Miao, N., Xu, B., Bristowe, N. C., Zhou, J., and Sun, Z. (2017). Tunable magnetism and extraordinary sunlight absorbance in indium triphosphide monolayer. *Journal of the American Chemical Society*, 139(32):11125–11131.

- Min, H., Hill, J., Sinitsyn, N. A., Sahu, B., Kleinman, L., and MacDonald, A. H. (2006). Intrinsic and rashba spin-orbit interactions in graphene sheets. *Physical Review B*, 74(16):165310.
- Mishra, H., Panda, J., Maddu, R., Sarkar, T., Dayen, J.-F., Belotcerkovtceva, D., and Kamalakar, M. V. (2021). Experimental advances in charge and spin transport in chemical vapor deposited graphene. *Journal of Physics: Materials*.
- Miyazaki, T., Yaoi, T., and Ishio, S. (1991). Large magnetoresistance effect in 82ni-fe/al-al2o3/co magnetic tunneling junction. *Journal of magnetism and magnetic materials*, 98(1-2):L7–L9.
- Monkhorst, H. J. and Pack, J. D. (1976). Special points for brillouin-zone integrations. *Physical review B*, 13(12):5188.
- Moodera, J. S., Kinder, L. R., Wong, T. M., and Meservey, R. (1995). Large magnetoresistance at room temperature in ferromagnetic thin film tunnel junctions. *Physical review letters*, 74(16):3273.
- Ning, Z. and Guo, H. (2008). Matdcal: A first principles package for nanoelectronics modeling. In *2008 22nd International Symposium on High Performance Computing Systems and Applications*, pages 16–16. IEEE.
- Novoselov, K. S., Geim, A. K., Morozov, S. V., Jiang, D., Katsnelson, M. I., Grigorieva, I., Dubonos, S., and Firsov, A. (2005a). Two-dimensional gas of massless dirac fermions in graphene. *nature*, 438(7065):197–200.
- Novoselov, K. S., Jiang, D., Schedin, F., Booth, T., Khotkevich, V., Morozov, S., and Geim, A. K. (2005b). Two-dimensional atomic crystals. *Proceedings of the National Academy of Sciences*, 102(30):10451–10453.
- Nowack, E., Schwarzenbach, D., and Hahn, T. (1991). Charge densities in cos2 and nis2 (pyrite structure). *Acta Crystallographica Section B: Structural Science*, 47(5):650–659.
- O’Hara, D. J., Zhu, T., Trout, A. H., Ahmed, A. S., Luo, Y. K., Lee, C. H., Brenner, M. R., Rajan, S., Gupta, J. A., McComb, D. W., et al. (2018). Room temperature intrinsic ferromagnetism in epitaxial manganese selenide films in the monolayer limit. *Nano letters*, 18(5):3125–3131.
- Papior, N., Lorente, N., Frederiksen, T., García, A., and Brandbyge, M. (2017). Improvements on non-equilibrium and transport green function techniques: The next-generation transiesta. *Computer Physics Communications*, 212:8–24.
- Perdew, J. P., Burke, K., and Ernzerhof, M. (1996). Generalized gradient approximation made simple. *Physical review letters*, 77(18):3865.



- Pi, K., Han, W., McCreary, K., Swartz, A., Li, Y., and Kawakami, R. (2010). Manipulation of spin transport in graphene by surface chemical doping. *Physical review letters*, 104(18):187201.
- Pillai, S. (2006). *Solid State Physics*. New Age International (P) Limited.
- Popov, I., Seifert, G., and Tománek, D. (2012). Designing electrical contacts to mos<sub>2</sub> monolayers: A computational study. *Phys. Rev. Lett.*, 108:156802.
- Pulizzi, F. (2012). Spintronics. *Nature materials*, 11(5):367–367.
- Radisavljevic, B., Radenovic, A., Brivio, J., Giacometti, V., and Kis, A. (2011). Single-layer mos 2 transistors. *Nature nanotechnology*, 6(3):147–150.
- Rao, C., Sood, A., Voggu, R., and Subrahmanyam, K. (2010). Some novel attributes of graphene. *The Journal of Physical Chemistry Letters*, 1(2):572–580.
- Schmidt, G., Ferrand, D., Molenkamp, L., Filip, A., and Van Wees, B. (2000). Fundamental obstacle for electrical spin injection from a ferromagnetic metal into a diffusive semiconductor. *Physical Review B*, 62(8):R4790.
- Semenov, Y., Zavada, J., and Kim, K. (2008). Magnetoresistance in bilayer graphene via ferromagnet proximity effects. *Physical Review B*, 77(23):235415.
- Sethulakshmi, N., Mishra, A., Ajayan, P. M., Kawazoe, Y., Roy, A. K., Singh, A. K., and Tiwary, C. S. (2019). Magnetism in two-dimensional materials beyond graphene. *Materials Today*, 27:107–122.
- Shen, T., Ren, J.-C., Liu, X., Li, S., and Liu, W. (2019). van der waals stacking induced transition from schottky to ohmic contacts: 2d metals on multilayer inse. *Journal of the American Chemical Society*, 141(7):3110–3115.
- Slonczewski, J. C. (1989). Conductance and exchange coupling of two ferromagnets separated by a tunneling barrier. *Physical Review B*, 39(10):6995.
- Smidstrup, S., Markussen, T., Vancraeyveld, P., Wellendorff, J., Schneider, J., Gunst, T., Verstichel, B., Stradi, D., Khomyakov, P. A., Vej-Hansen, U. G., et al. (2019). Quantumatk: an integrated platform of electronic and atomic-scale modelling tools. *Journal of Physics: Condensed Matter*, 32(1):015901.
- Soler, J. M., Artacho, E., Gale, J. D., García, A., Junquera, J., Ordejón, P., and Sánchez-Portal, D. (2002). The siesta method for ab initio order-n materials simulation. *Journal of Physics: Condensed Matter*, 14(11):2745.
- Sommerfeld, A. and Bethe, H. (1933). Elektronentheorie der metalle. In *Aufbau Der zusammenhängenden materie*, pages 333–622. Springer.

- Stokbro, K. (2008). First-principles modeling of electron transport. *Journal of Physics: Condensed Matter*, 20(6):064216.
- Stoller, M. D., Park, S., Zhu, Y., An, J., and Ruoff, R. S. (2008). Graphene-based ultracapacitors. *Nano letters*, 8(10):3498–3502.
- Sun, Y., Zhuo, Z., Wu, X., and Yang, J. (2017). Room-temperature ferromagnetism in two-dimensional fe<sub>2</sub>si nanosheet with enhanced spin-polarization ratio. *Nano letters*, 17(5):2771–2777.
- Tarawneh, K., Al-Aqtash, N., and Sabirianov, R. (2016). Large magnetoresistance in planar Fe/MoS<sub>2</sub>/Fe tunnel junction. *Computational Materials Science*, 124:15–22.
- Taylor, J., Guo, H., and Wang, J. (2001). Ab initio modeling of quantum transport properties of molecular electronic devices. *Physical Review B*, 63(24):245407.
- Thomas, L. H. (1927). The calculation of atomic fields. In *Mathematical proceedings of the Cambridge philosophical society*, volume 23, pages 542–548. Cambridge University Press.
- Tombros, N., Jozsa, C., Popinciuc, M., Jonkman, H. T., and Van Wees, B. J. (2007). Electronic spin transport and spin precession in single graphene layers at room temperature. *nature*, 448(7153):571–574.
- Tsymbal, E. Y., Mryasov, O. N., and LeClair, P. R. (2003). Spin-dependent tunnelling in magnetic tunnel junctions. *Journal of Physics: Condensed Matter*, 15(4):R109.
- Tung, R. T. (2014). The physics and chemistry of the schottky barrier height. *Applied Physics Reviews*, 1(1):011304.
- Valiev, M., Bylaska, E. J., Govind, N., Kowalski, K., Straatsma, T. P., Van Dam, H. J., Wang, D., Nieplocha, J., Apra, E., Windus, T. L., et al. (2010). Nwchem: A comprehensive and scalable open-source solution for large scale molecular simulations. *Computer Physics Communications*, 181(9):1477–1489.
- Vogt, P., De Padova, P., Quaresima, C., Avila, J., Frantzeskakis, E., Asensio, M. C., Resta, A., Ealet, B., and Le Lay, G. (2012). Silicene: compelling experimental evidence for graphenelike two-dimensional silicon. *Physical review letters*, 108(15):155501.
- Wang, W., Narayan, A., Tang, L., Dolui, K., Liu, Y., Yuan, X., Jin, Y., Wu, Y., Rungger, I., Sanvito, S., et al. (2015). Spin-valve effect in nife/mos<sub>2</sub>/nife junctions. *Nano letters*, 15(8):5261–5267.

- Wang, Z., Gutiérrez-Lezama, I., Ubrig, N., Kroner, M., Gibertini, M., Taniguchi, T., Watanabe, K., Imamoglu, A., Giannini, E., and Morpurgo, A. F. (2018). Very large tunneling magnetoresistance in layered magnetic semiconductor  $\text{CrI}_3$ . *Nature communications*, 9(1):1–8.
- Werner, H.-J., Knowles, P. J., Knizia, G., Manby, F. R., and Schütz, M. (2012). Molpro: a general-purpose quantum chemistry program package. *Wiley Interdisciplinary Reviews: Computational Molecular Science*, 2(2):242–253.
- Wolf, S. A., Chtchelkanova, A. Y., and Treger, D. M. (2006). Spintronics—a retrospective and perspective. *IBM journal of research and development*, 50(1):101–110.
- Xiao, D., Yao, W., and Niu, Q. (2007). Valley-contrasting physics in graphene: magnetic moment and topological transport. *Physical Review Letters*, 99(23):236809.
- Xu, C., Luo, G., Liu, Q., Zheng, J., Zhang, Z., Nagase, S., Gao, Z., and Lu, J. (2012). Giant magnetoresistance in silicene nanoribbons. *Nanoscale*, 4(10):3111–3117.
- Yang, J., Wang, J., Liu, Q., Xu, R., Sun, Y., Li, Z., Gao, F., and Xia, M. (2020). Band engineering in intrinsically magnetic  $\text{CrBr}_3$  monolayer. *Journal of Magnetism and Magnetic Materials*, 502:166608.
- Yang, Y. T., Ding, R. X., and Song, J. X. (2011). Transport properties of boron-doped single-walled silicon carbide nanotubes. *Physica B: Condensed Matter*, 406(2):216–219.
- Yao, W., Xiao, D., and Niu, Q. (2008). Valley-dependent optoelectronics from inversion symmetry breaking. *Physical Review B*, 77(23):235406.
- Yeo, B. C., Kim, D., Kim, C., and Han, S. S. (2019). Pattern learning electronic density of states. *Scientific reports*, 9(1):1–10.
- Zhang, K., Feng, Y., Wang, F., Yang, Z., and Wang, J. (2017). Two dimensional hexagonal boron nitride (2d-hbn): synthesis, properties and applications. *Journal of Materials Chemistry C*, 5(46):11992–12022.
- Zhang, Q., Chan, K. S., and Lin, Z. (2011). Spin current generation by adiabatic pumping in monolayer graphene. *Applied Physics Letters*, 98(3):032106.
- Zhang, W.-B., Qu, Q., Zhu, P., and Lam, C.-H. (2015). Robust intrinsic ferromagnetism and half semiconductivity in stable two-dimensional single-layer chromium trihalides. *Journal of Materials Chemistry C*, 3(48):12457–12468.

Zhen, Z. and Zhu, H. (2018). Structure and properties of graphene. In *Graphene*, pages 1–12. Elsevier.

# List of publications

## Research publications

- **Nayana Devaraj** and Kartick Tarafder. "Spin-transport through Van der Waals heterojunctions based on 2D-ferromagnet and transition metal dichalcogenides: A study from first-principles calculations" *Advanced Theory and Simulations*, 2022.
- **Nayana Devaraj** and Kartick Tarafder. "Large magnetoresistance in a Co/MoS<sub>2</sub>/graphene/MoS<sub>2</sub>/Co magnetic tunnel junction". *Physical Review B*, 103(16): 165407, 2021.
- **Nayana Devaraj** and Kartick Tarafder. "Spin transport through metal-dichalcogenides layers: a study from first-principles calculations". *Journal of Physics: Condensed Matter*, 33(6):065505, 2020.
- T Sruthi, **Nayana Devaraj**, and Kartick Tarafder. "Theoretical investigation of quantum capacitance in the functionalized MoS<sub>2</sub>-monolayer. *Electronic Structure*, 3(2):025003, 2021.

## Other publications

- Soumitra Payra, **Nayana Devaraj**, Kartick Tarafder, and Sounak Roy. "Unprecedented electroreduction of CO<sub>2</sub> over metal organic framework-derived intermetallic nano-alloy Cu<sub>0.85</sub>Ni<sub>0.15</sub>/C". *ACS Applied Energy Materials*, 2022.
- Saraswati Roy, **Nayana Devaraj**, Kartick Tarafder, Chanchal Chakraborty, and Sounak Roy. "The role of synthesis vis-à-vis oxygen vacancies of Co<sub>3</sub>O<sub>4</sub> in oxygen evolution reaction". *New Journal of Chemistry*, 2022.

## Conference Presentations

- **Nayana Devaraj**, and Kartick Tarafder. "Spin Polarized Transport and Magnetoresistance in Co/MoSe<sub>2</sub>/Co Junction" International Conference on Current Trends in Functional Materials (CTFM - 2020) at National Institute of Technology Karnataka, Surathkal, January, 2020.  
Poster presentation
- **Nayana Devaraj**, and Kartick Tarafder. "Comparative Study of Spin Transport in Metal/Mono-layer TMDC Junctions" International Conference

on Applied Materials and Technology (AMT - 2020), S. Nijalingappa College, Bengaluru, October, 2020.

Oral presentation

- **Nayana Devaraj**, and Kartick Tarafder "High Magnetoresistance in Co/TMDC/Co Magnetic Junctions" National Conference in the Physics of Materials, December, 2021, CSIR-NIIST, Thiruvananthapuram.

Poster presentation

## Workshops

- Two Weeks International Workshop on Research Methodology, Academic Writing and Publishing (IWRAP-22), February 2022, Sir Syed College, Taliparamba.
- Indo-US symposium on "Recent Advances in Magnetism and Spintronics", February 2018, Indian Institute of Technology Bombay, Mumbai.
- International Workshop on Advanced Materials (IWAM-2017) December, 2017, National Institute of Science & Technology, Berhampur, Orissa.
- Science Academies' lecture workshop on Topology in Condensed Matter Physics, March 2017, Sri Dharmasthala Manjunatheshwara College, Ujire.
- GIAN course "Quantum Transport: Atom to Transistor" December, 2016, Jawaharlal Nehru University, Delhi.
- GIAN course on Novel Functional Materials for Energy Conversion, October 2016, National Institute of Technology Karnataka, Surathkal.
- National Workshop on Computational Dynamics, September 2016, National Institute of Technology Karnataka, Surathkal.

## CURRICULUM VITAE

NAYANA DEVARAJ

### **Permenant Address:**

Neelambari,  
Pallikkunnu P.O.,  
Kannur,  
Kerala,  
India.  
Pin: 670004  
Mobile: 9497854826  
e-mail: nayanadevaraj@gmail.com

### **Academic Qualifications:**

#### **Master of Science**

C.G.P.A 7.68/10  
Central University of Kerala,  
Kerala,  
India.

#### **Bachelor of Science**

C.G.P.A : 3.34 /4  
Kannur University,  
Kerala,  
India.

**Research Publications :** 7

**Conferences attended :** 3

**Workshops attended :** 7